Réseaux multi-octave d'antennes spirales connectées

Pedro Mendes Ruiz

université PARIS-SACLAY

NNT : 2018SACLC075

CentraleSupélec

Multi-Octave Connected Spiral Arrays

Thèse de doctorat de l'Université Paris-Saclay
préparée à CentraleSupélec

École doctorale n°575
Electrical, optical, bio: physics and engineering (EOBE)
Spécialité de doctorat:
Electronique et Optoélectronique, Nano- et Microtechnologies

Thèse présentée et soutenue à Gif-sur-Yvette, le 09 octobre 2018, par

Pedro Mendes Ruiz

Composition du Jury :

Xavier Begaud Professeur, Télécom Paristech	Président du jury
Raphaël Gillard Professeur des Universités, INSA - Rennes	Rapporteur
Warren L. Stutzman Professeur Emérite, Virginia Tech	Rapporteur
Nicolas Ribière-Tharaud Ingénieur de Recherche, CEA	Examinateur
Régis Guinvarc'h Professeur, CentraleSupélec	Directeur de thèse
Randy L. Haupt Professeur, Colorado School of Mines	Encadrant
Israel Hinostroza Professeur assistant, CentraleSupélec	Encadrant

Thèse de doctorat

Introduction

Les réseaux d'antennes à large bande ont de nombreuses applications allant des télécommunications au radar et aux prévisions météorologiques. Parmi les caractéristiques qui ont un grand impact sur ces applications nous pouvons citer la qualité de la polarisation, le gain, la taille occupée par le réseau ainsi que la bande passante.

Plusieurs techniques ont été proposées pour élargir la bande passante des réseaux d'antennes. Une des problématiques qui est souvent associée aux réseaux large bande est l'apparition des lobes de réseaux, liées à la périodicité de l'espacement entre les éléments du réseau. Un des moyens employés pour résoudre ce problème est de supprimer la périodicité dans le réseau, par exemple avec l'utilisation des réseaux non-uniformément espacés.

Un autre problème dans les réseaux large bande est la fréquence de fonctionnement de l'élément du réseau. La plus basse fréquence d'opération est généralement liée à la taille de l'élément. Une possibilité pour traiter cette limitation est de profiter du couplage mutuel entre les éléments qui sont voisins dans le réseau.

De plus, plusieurs facteurs peuvent perturber la pureté de la polarisation rayonnée par les réseaux d'antennes. Pour adresser ce problème nous pouvons, par exemple, corriger les facteurs perturbateurs, comme pour éviter les résonances à mode-commun à travers le design soigneux du réseau d'alimentation (un problème connu dans les réseaux connectés), ou imposer la pureté de la polarisation à travers l'utilisation de la technique de rotation séquentielle pour le cas de la polarisation circulaire.

L'objectif de cette thèse est de développer un réseau d'antenne avec une bande passante de 10:1 capable de dépointer jusqu'à 30° avec les caractéristiques suivantes :

- Double polarisation circulaire (Axial Ratio inférieur à 3 dB)
- Coefficient de Réflexion inférieur à -10 dB
- Niveau des Lobes Secondaires Relative inférieur à -10 dB
- Design compact

Pour obtenir ces caractéristiques nous avons pris les Réseaux d'Anneaux Concentriques d'Antennes Spirales Archimédiennes développés par (*Hinostroza, 2013*) comme point de départ. Dans ces travaux, des connections entre les antennes spirales voisines dans un réseau circulaire ont été utilisées pour diminuer le coefficient de réflexion des spirales et les anneaux concentriques non uniformément espacés ont été utilisés pour diminuer les lobes secondaires qui étaient intrinsèquement hauts dans ce design.

Dans cette thèse nous allons d'abord implémenter les deux concepts dans un seul réseau et, après, nous allons retravailler la méthodologie d'optimisation puis incorporer la technique WAVES pour obtenir un réseau qui à la fois soit plus compact et possède une bande passante deux fois plus grande. Le réseau conçu répond aux exigences en dépointant jusqu'à 30° pour une bande passante qui va de 1 GHz à 13 GHz, avec les dimensions circonscrites par un cercle de rayon de 35 cm.

Le réseau conçu, bien qu'il remplisse les objectifs, a le désavantage d'être lacunaire, ce qui implique que le gain réalisé soit loin du gain surfacique maximal. Pour traiter cette faiblesse, une nouvelle conception de réseau large bande d'antennes spirales connectés a été proposée. Le nouveau concept consiste en un réseau 2-D de spirales à 4 bras avec les bras des spirales voisines dans le réseau connectés. Des simulations FEKO du réseau fini et infini ainsi qu'un prototype ont permis de valider le concept.

Réseau d'anneaux concentriques

Dans cette thèse un réseau d'anneaux concentriques a été développé. Les connections entre les spirales de polarisation opposée diminuent le coefficient de réflexion dans les fréquences basses, de façon à ce que la fréquence d'opération basse du réseau soit divisée par 3.3. En même temps, la topologie des anneaux concentriques, avec comme paramètres les rayons des anneaux et leurs rotations relatives, a été optimisée avec des Algorithmes Génétiques pour minimiser le niveau des lobes secondaires relatifs dans les hautes fréquences.

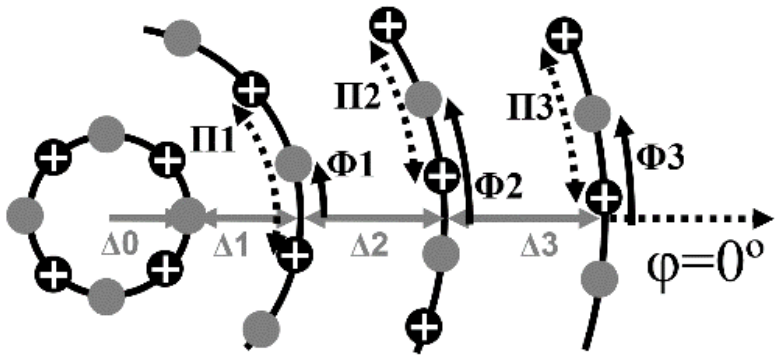

Figure 1 Réseau d'anneaux concentriques : les cercles remplies et avec des croix représentent, respectivement, les spirales polarisés main gauche et main droite. Les spirales sont intercalées, ce qui rend le réseau lacunaire, et alors des lobes secondaires hauts (« lobes de réseau ») apparaissent dans la zone visible de rayonnement. Les anneaux concentriques peuvent avoir les rayons et rotations relatives optimisés pour réduire ces lobes et alors réduire le niveau de lobes secondaires relative à hautes fréquences.

L'addition d'une contrainte de taille dans la procédure d'optimisation a eu comme résultat un réseau occupant 29% seulement de la surface occupée par le réseau au design antérieur, avec la même bande passante. Le réseau optimisé a été simulé avec FEKO et il opère entre 1 GHz et 6.9 GHz en dépointant jusqu'à 30°, en plus de répondre aux exigences suivantes :

- Double polarisation circulaire (Axial Ratio inférieur à 3 dB)
- Coefficient de Réflexion inférieur à -10 dB
- Niveau des Lobes Secondaires Relative inférieur à -10 dB
- Design compact

Tableau 1 Valeurs optimales des paramètres du réseau d'anneaux concentriques compacte. Valeur obtenus avec une zone de recherche des lobes secondaires réduite pour la fonction coût, en plus d'un poids rajouté au premier lobe secondaire.

Δ_0(cm)	Δ_1(cm)	Δ_2(cm)	Δ_3(cm)	Φ_1(rad)	Φ_2(rad)	Φ_3(rad)	$\sum_{i=0}^{N_r-1} \Delta_i$
7.24	8.01	8.42	9.18	0.64 Π_1 = 0.31	0.52 Π_2 = 0.16	0.52 Π_3 = 0.12	32.9 < 33 cm

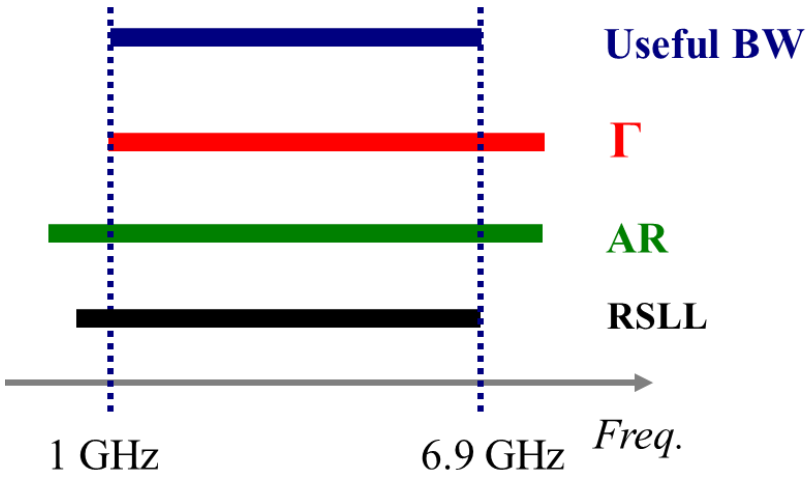

Figure 2 Les barres correspondent aux définitions de bande passante ci-après. En rouge nous avons la barre qui correspond au coefficient de réflexion, en vert le rapport axiale et en noir le niveau des lobes secondaires relative. La bande passante utile est l'intersection de ces trois bandes passantes.

Le design a été d'avantage développé avec la technique WAVES avec l'inclusion d'une copie réduite en son centre. Le réseau d'anneaux concentriques avec WAVES a été simulé avec FEKO dans ces trois modes d'opération : seules les antennes plus grandes allumées avec les antennes plus petites adaptées à des résistances de 220 Ω (1 GHz – 4 GHz), toutes les antennes allumées (4 GHz – 9.5 GHz) et seules les antennes plus petites allumées avec les antennes plus grandes adaptées à des résistances de 220 Ω (9.5 GHz – 13 GHz). Le chevauchement de la bande passante des 3 modes d'opération couvre une bande passante de 1 GHz à 13 GHz.

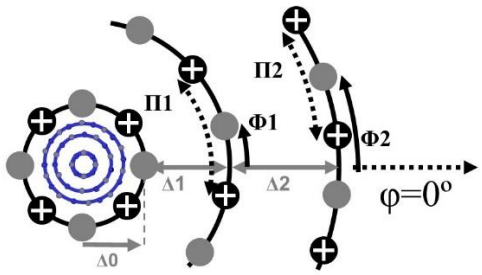

Figure 3 Schéma du réseau d'anneaux concentriques avec WAVES.

Tableau 2 Valeurs optimales des paramètres des éléments plus grands du réseau d'anneaux concentriques avec WAVES

Parameter	Δ_0(cm)	Δ_1(cm)	Δ_2(cm)	Φ_1(rad)	Φ_2(rad)	$\sum_{i=0}^{N_r-1} \Delta_i$
Range	12 – 17.7	$d_{r-to-r} - 2\,d_{r-to-r}$	$d_{r-to-r} - 2\,d_{r-to-r}$	0 – Π_1	0 – Π_2	< 33 cm
Optimized Value	15.26	9.20	8.39	0	0.27 rad = 0.11 Π_2	32.85 cm

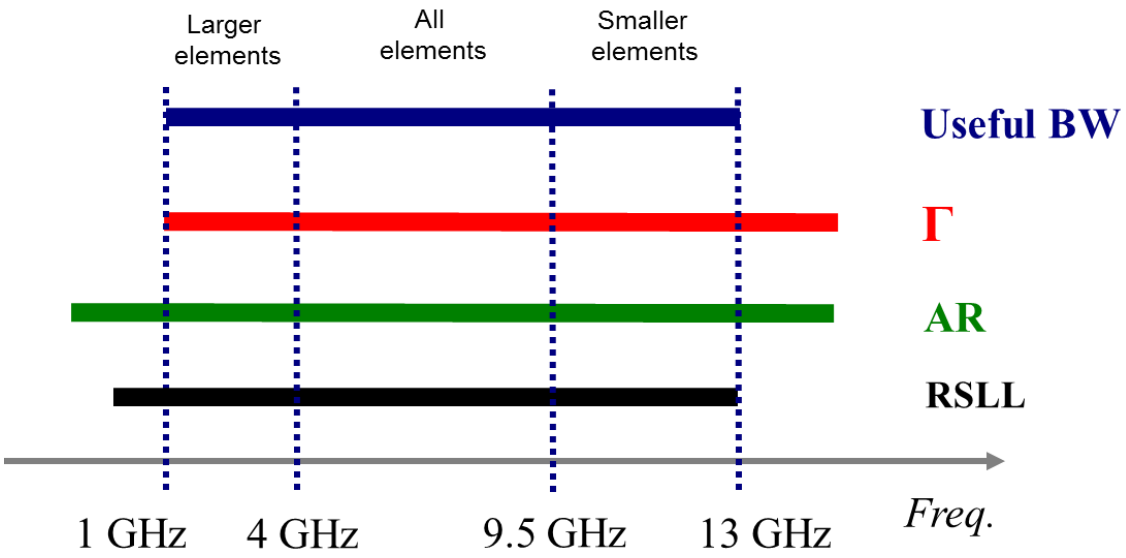

Figure 4 Les barres correspondent aux définitions de bande passante ci-après. En rouge nous avons la barre qui correspond au coefficient de réflexion, en vert le rapport axiale et en noir le niveau des lobes secondaires relative. La bande passante utile est l'intersection de ces trois bandes passantes.

La comparaison entre les deux designs a mis en évidence un compromis entre le gain et la bande passante. Le réseau d'anneaux concentriques sans WAVES a un gain environ 1.7 dB plus grand que l'autre design entre 4 GHz et 6 GHz. De plus il fonctionne en un seul mode d'opération ce qui permet un réseau d'alimentation plus simple. Cependant la bande passante est considérablement plus importante dans le réseau d'anneaux concentriques avec WAVES.

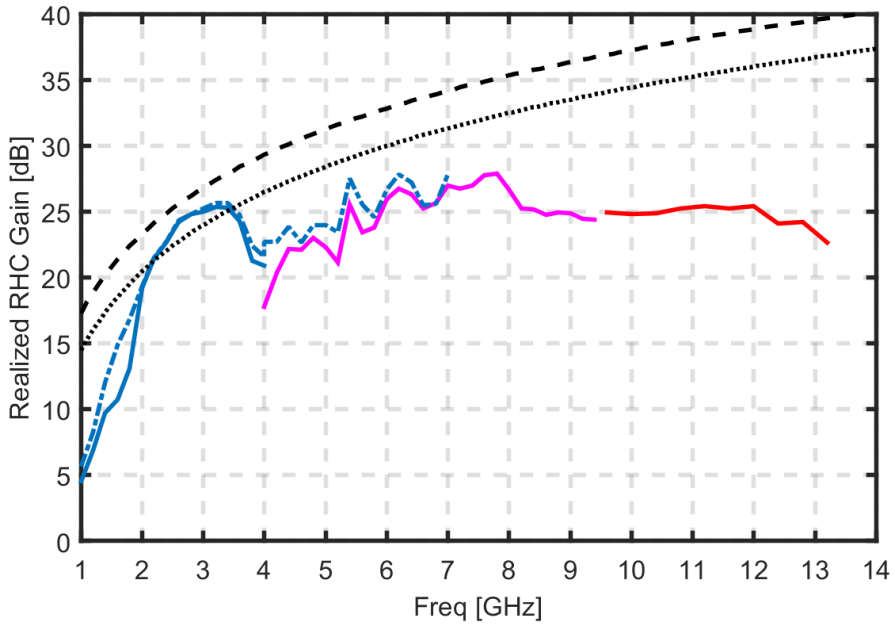

Figure 5 Courbes de gain réalisé à "broadside" pour le réseau d'anneaux concentriques de la section 2.3.3 (ligne bleu tireté) et pour le réseau d'anneaux concentriques avec WAVES de la section 2.4.1 avec que les éléments grands allumés (bleu), les éléments grands et petits allumés en même temps (magenta) et seulement les éléments petits allumés (rouge). Superposé nous avons le gain surfacique maximal correspondant au cercle de rayon de 35 cm (surface de 0.38 m^2) auquel les réseaux sont circonscrits (ligne noir tireté) aussi que celui correspondant à la surface occupé par les cavités des réseaux d'anneaux concentriques avec et sans WAVES, qui sont égales à 0.2 m^2 dans les deux cas (ligne noir pointillé).

Vu que le réseau d'anneaux concentriques de spirales connectés est lacunaire, son gain est petit comparé avec le gain surfacique. Ainsi nous allons proposer un nouveau design pour connecter des antennes spirales.

Réseau planaire d'antennes spirales connectés

Le nouveau design consiste en des antennes spirales disposées dans un réseau uniforme avec les bras connectés aux bras des antennes voisines. Nous avons concentré nos études sur les spirales à 4 bras car leurs simulations ont présenté une meilleure adaptation comparées aux spirales à 3 bras et moins de résonances par rapport aux spirales à 6 bras. De plus le réseau d'alimentation pour les spirales à 4 bras suppose des phases multiples de 90°, ce qui rend la construction et la mesure d'un prototype plus facile. Le nouveau design de réseau d'antennes spirales à 4 bras connectés a été analysé en simulations finies et infinies avec FEKO. Les simulations indiquent que le réseau peut avoir une bande passante arbitrairement large selon la finitude du réseau car les simulations infinies n'ont pas montré de limite.

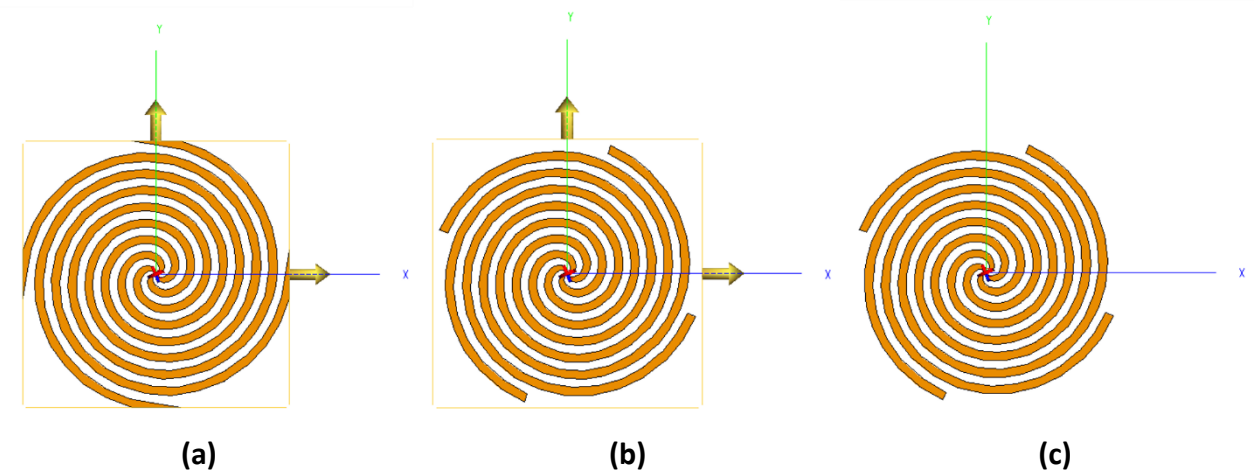

Figure 6 Modèles FEKO correspondant, de gauche à droite, au réseau infini de spirales à quatre bras connectés, au réseau infini de spirales à quatre bras non connectés et à une seule spirale à quatre bras. Les spirales ont un rayon égal à 2.4 cm.

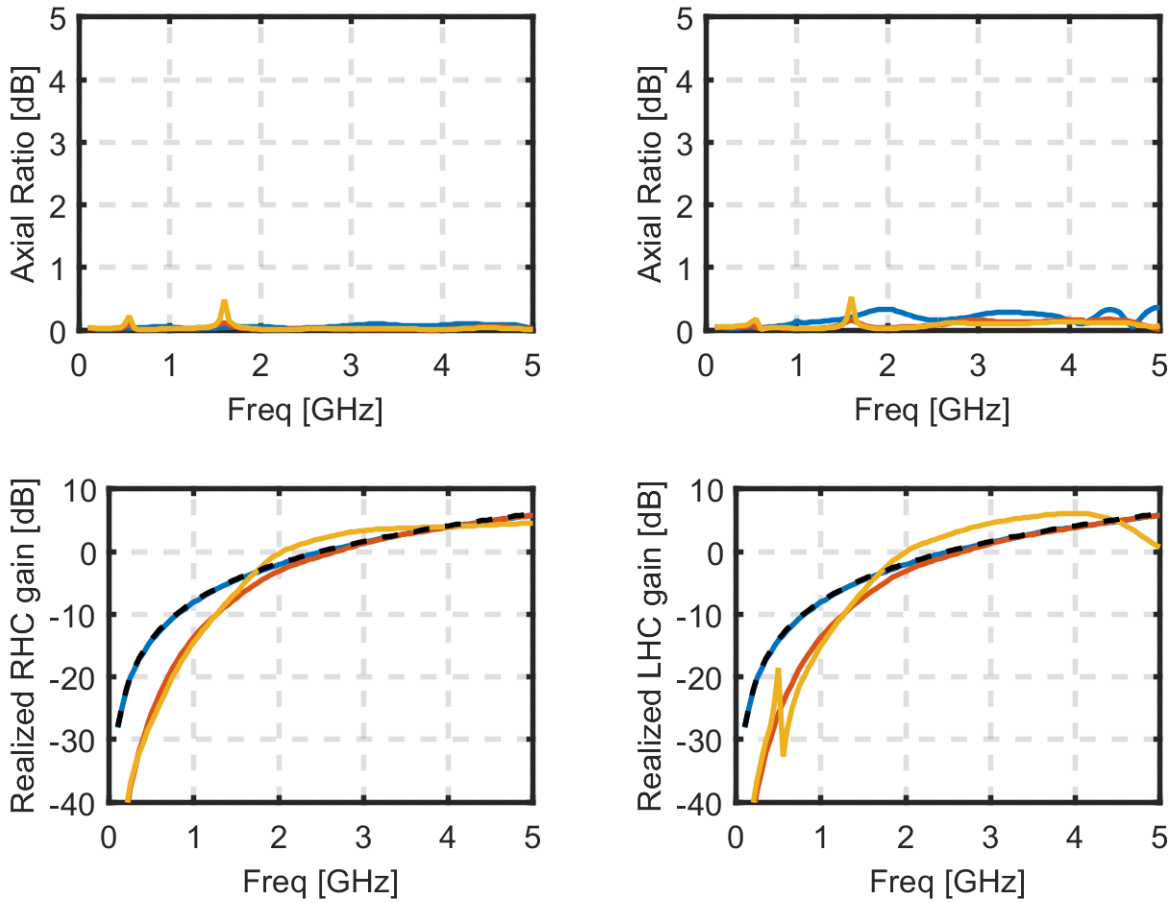

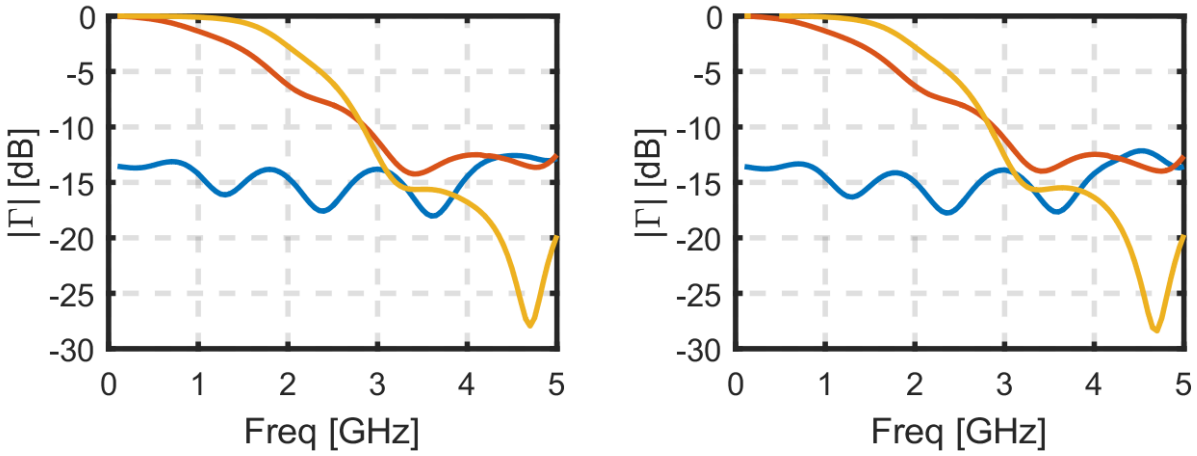

Figure 7 Simulation FEKO du réseau infini de spirales à quatre bras connectés (bleu), du réseau infini de spirales à quatre bras non connectés (rouge) et de la spirale à quatre bras seule (jaune). Les courbes à gauche montrent la polarisation principale (mode 1) et les courbes à droite montrent la polarisation secondaire (mode -1). Les courbes en tireté noir montrent le gain surfacique maximal correspondant à la région enfermée par les limites périodiques moins 3 dB pour compenser le fait que les antennes rayonnent des deux côtés.

Un prototype a été construit et le coefficient de réflexion aussi bien que le gain du réseau pour les polarisations circulaires main droite et circulaire main gauche ont été mesurées et sont en accord avec les simulations FEKO.

Figure 8 Mesure des paramètres S du prototype du réseau de spirales non complémentaires à quatre bras connectés.

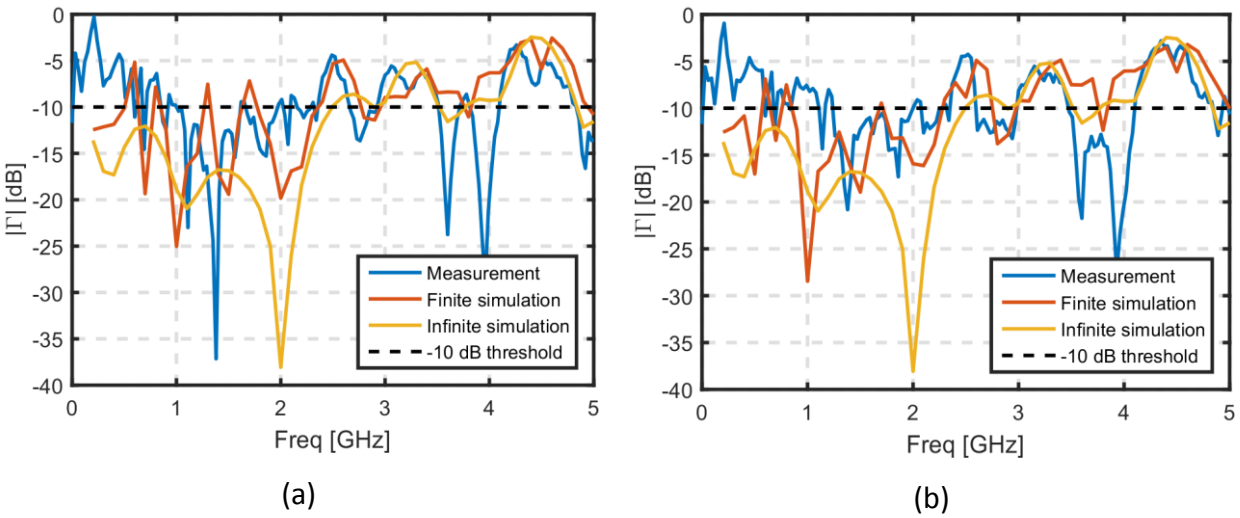

Figure 9 Coefficient de réflexion du réseau prototype, de la simulation FEKO du réseau de 3x3 spirales non complémentaires à quatre bras connectés avec une couche d'éléments adaptés par des résistances de 100 Ω et de la simulation FEKO du réseau infini de spirales non complémentaires à quatre bras connectés. En (a) nous avons le réseau avec polarisation circulaire main droite (mode 1) et en (b) nous avons le réseau avec polarisation circulaire main gauche (mode-1).

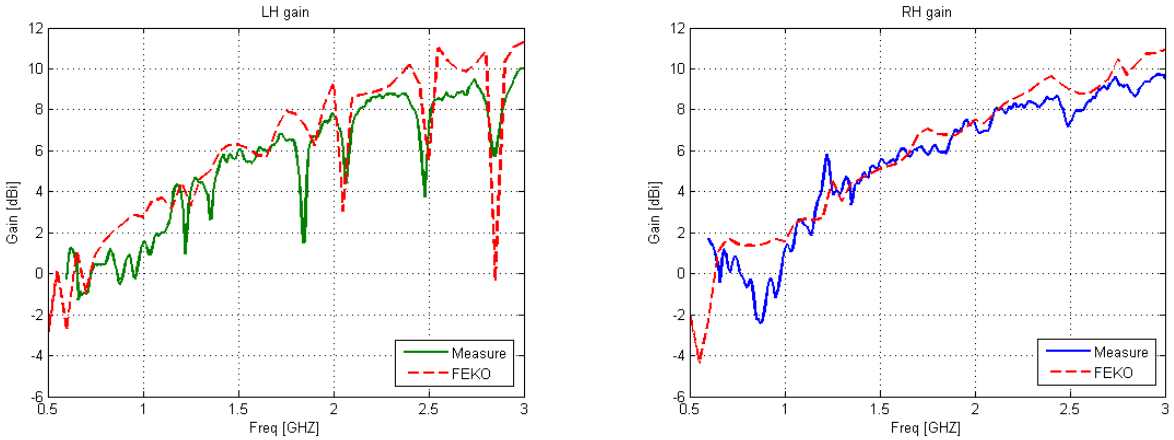

Figure 10 Gain de la composante à polarisation circulaire main droite et main gauche du réseau prototype et de la simulation FEKO du réseau de 3x3 spirales non complémentaires à quatre bras connectés avec une couche d'éléments adaptés par des résistances de 100 Ω.

Acknowledgments

I would like to begin this series of acknowledgments by thanking my team of supervisors. I have had valuable counsel from their mentoring and this work would not have been possible without them. I would like to thank Israel Hinostroza for the endless patience in the frequent and long discussions we had, sometimes on a daily basis. I would also like to thank Régis Guinvarc'h for the guidance on finding meaningful directions for my research - whenever it felt like I had hit a wall, in a minute or two a side door was already open. Last but not least, I would like to thank Randy Haupt for the spot on advices on about every topic I have come across for the last three years – I have learnt a lot from our discussions. Working with the three of you was a truly fulfilling experience.

I would also like to thank the members of the jury, Xavier Begaud and Nicolas Ribière-Tharaud, and the thesis reviewers, Raphaël Gillard and Warren Stutzman, for the interest they took in my work and for the valuable insight offered on the thesis corrections as well as in the questions posed during the defense. It was an honor to have you in my jury.

Moreover, I would like to thank all of the people with whom I have worked for the last years. Even in the cold winter I could always count on you for a good laugh at lunch or on the coffee break(s). I wish all of the best for the SONDRA team (for those still there, still to come, just arriving as well as those who already left a while ago). I will surely visit from time to time.

I also want to thank all of my family and friends for all of the love and continuous support during my PhD. A big thanks to my friends from the musical groups Rateria, Elephanfare and Mammouth Brassband - playing with you guys and having your friendship has always lifted my spirits.

A special thanks for the Brazilian community from CentraleSupélec. We have met when we first came to France and went through it all together – I will always be thankful for your friendship (and, obviously, of all of the friendships that came along the way since our arrival – I am profoundly grateful to have you all in my life).

I also want to thank both my brothers, Miguel and Vitor, for all of the love and care. Thanks to my mother Célia, my step father Eduardo, my father Miguel and my step mother Renata for always believing in me and always making sure that I am taking care of myself. You all are my foundation. Amo vocês do fundo do meu coração!

Table of Contents

Introduction

Wideband antenna arrays have many applications from telecommunications to radar and weather forecasting. Some characteristics that have a large impact on the utility of those arrays are the polarization characteristics, the gain, the size occupied as well as the bandwidth.

Several techniques have been proposed over the years to extend the bandwidth of antenna arrays. One of the usual problems associated with wideband arrays is having the highest frequency of operation limited by the onset of grating lobes, associated with the periodicity in the spacing between elements of the array. One of the means to tackle this issue is breaking the periodicity of the array, for instance by using non-uniformly spaced arrays.

Another issue in wideband arrays is the working frequency of the element of the array. The lowest frequency of operation is in general related to the size of the element. A recent trend used to address this limitation is to take advantage of the mutual coupling between neighboring elements in an array, in such a way that the size of the element is not necessarily the limiting factor rather than the array's size.

In addition, several factors can disturb the purity of the radiated polarization of antenna arrays. In order to address this issue one can, for instance, either tackle the disturbing factors, as in the case of avoiding common-mode resonances by the careful design of the feeding network (a known issue in connected arrays), or enforce the purity of the polarization by the use of the sequential rotation technique for the case of circular polarization.

The objective of this thesis is to develop an antenna array with a bandwidth of 10:1 and while steering up to 30° and having the following characteristics:

- Dual circular polarization (Axial Ratio below 3 dB)
- Reflection coefficient below -10 dB
- Relative Sidelobe Level below -10 dB
- Compact design

In order to obtain such characteristics we take the Concentric Ring Array of Archimedean Spirals developed in (*Hinostroza, 2013*) as the point of departure. In his work connections between

neighboring spirals in a circular array were used to lower the reflection coefficient of the spirals and non-uniformly spaced concentric rings of spirals were optimized to lower the high sidelobes intrinsic to the design.

In this thesis we first implement both design trends in a single array and then we further develop the Concentric Rings design by rethinking the optimization as well as using the WAVES technique to obtain an array that is at the same time more compact and has twice the original bandwidth. The designed array meets the requirements, up to a scan angle of 30°, for an operating band of 1 GHz to 13 GHz, while occupying an area circumscribed by a circle of radius of 35 cm.

The designed array, although it fulfills the objectives, has the downside of being sparse, which implies that the realized gain is below that achievable for the area. To address this weakness, a new topology for a wideband antenna array of connecting spirals is proposed. The new topology consists of a 2-D array of 4 arm spirals with the neighboring spirals arms connected. Infinite and finite array FEKO simulations as well as an experimental prototype validate the concept.

In Chapter 1 we present the state of the art as well as theoretical concepts important for the development of the thesis.

In Chapter 2 we present the development of the Concentric Ring Array of Connecting Spirals, including the presentation of the topology's geometry, the steps taken in the development of the optimization procedure and the optimized design, which has been analyzed by an embedded element model and by a FEKO simulation. Next, the addition of the WAVES technique is discussed and implemented using the concepts developed in the chapter, rendering a new design that is also analyzed with the approximated model and by FEKO.

In Chapter 3 we propose a new topology for a 2-D array of connected four-arm spirals. Infinite array simulations are used to present the topology's potential at providing an arbitrarily large bandwidth. Then we explore the finiteness effects on the array by running FEKO simulations, which are later validated by an experimental prototype.

References

Hinostroza, I., “Design of wideband arrays with Archimedean Spiral Antennas,” Ph. D. Dissertation, SUPELEC, Gif-sur-Yvette, France, 2013.

Chapter 1: State of Art and Theoretical Concepts

1.1. Introduction

In this chapter we present concepts that are key for the development of the thesis, including the array requirements, the operation of spiral antennas and several array concepts.

1.2. Definitions of Key Array Characteristics

1.2.1. Axial Ratio

The axial ratio of an antenna is defined as the ratio of the major axis to the minor axis of the polarization ellipse of the electric field radiated by the antenna. In Fig. 1. 1 we show the polarization ellipse of an electric field with Axial Ratio equal to 3 dB, meaning that the major axis of the ellipse is $\sqrt{2}$ larger than the smaller axis.

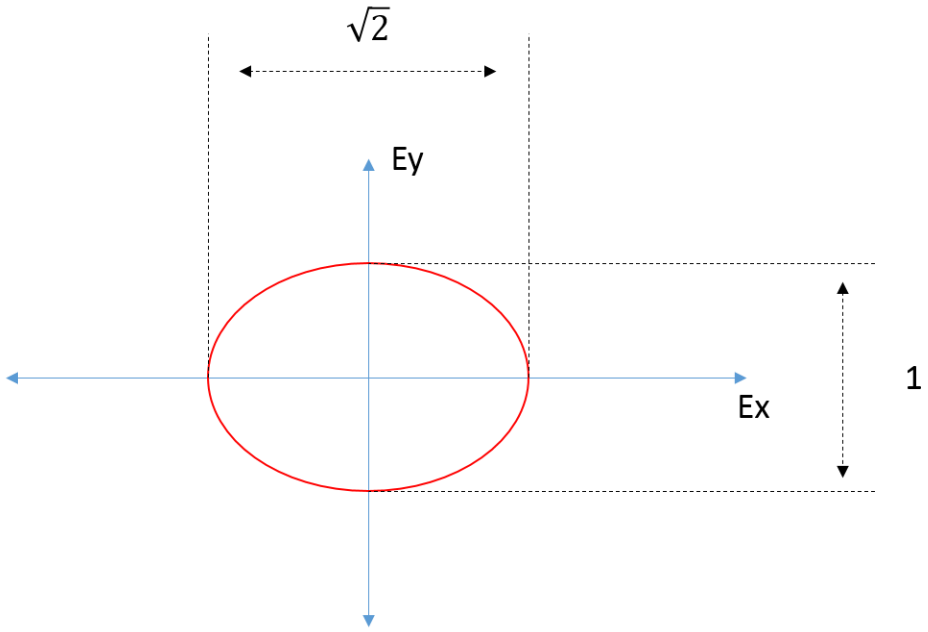

Fig. 1. 1 Polarization ellipse of an electric field with an Axial Ratio of 3 dB, which corresponds to a Cross Polarization Ratio of 15 dB

Another way of measuring the polarization purity of an electric field is the cross polarization ratio, which consists of the ratio of the principal polarization component to the cross polarization component of an electric field.

One can easily interchange between Axial Ratio and Cross Polarization Ratio using (1.1).

$$XpolR = 20\ log_{10} \frac{10^{\frac{AR}{20}} + 1}{10^{\frac{AR}{20}} - 1} \tag{1.1}$$

The quality of the polarization is important to several applications, for instance in radar analysis for the extraction of the features of targets and polarimetric radar (*Lee and Pottier, 2009*).

Given the importance of the polarization quality we decided to analyze the impact of array errors on the polarization produced by planar arrays, considering the elements to be ideal crossed dipoles as a first approach. We develop this approach in Appendix A.

1.2.2. Reflection Coefficient

The reflection coefficient, $|\Gamma|$, represents the energy that is reflected back to the power source. This happens due to an impedance mismatch between the antenna and the power source (1.2). For instance, a $|\Gamma|$ of -10 dB represents a loss in the power delivered to the antenna of 10% (1.3). The reflection coefficient is:

$$\Gamma = \frac{Z_{antenna} - Z_{source}}{Z_{antenna} + Z_{source}} \tag{1.2}$$

with $Z_{antenna}$ the impedance of the antenna and Z_{source} the impedance of the power source.

Using this to find the power accepted by the antenna:

$$P_{antenna} = (1 - |\Gamma|^2) \times P_{source} = \left(1 - \left|10^{\frac{-10}{20}}\right|^2\right) \times P_{source} = 0.9 \times P_{source} \tag{1.3}$$

with $P_{antenna}$ the power radiated by the antenna and P_{source} the power delivered by the power source.

In antenna arrays one can distinguish the reflection coefficient of the antenna system and the reflection coefficient of the array elements. The reflection coefficient from the antenna system can be treated as in equation (1.2).

For the antenna elements it is important to take into account the mutual coupling between elements. In general, multiple elements in the array are operating at the same time, so the power that is reflected depends not only on the impedance mismatch in the element feed but also on the coupling between the different elements. It is simple to obtain the reflection

coefficient on each of the antenna elements by representing the array as a multiport system using S parameters (Fig. 1. 2).

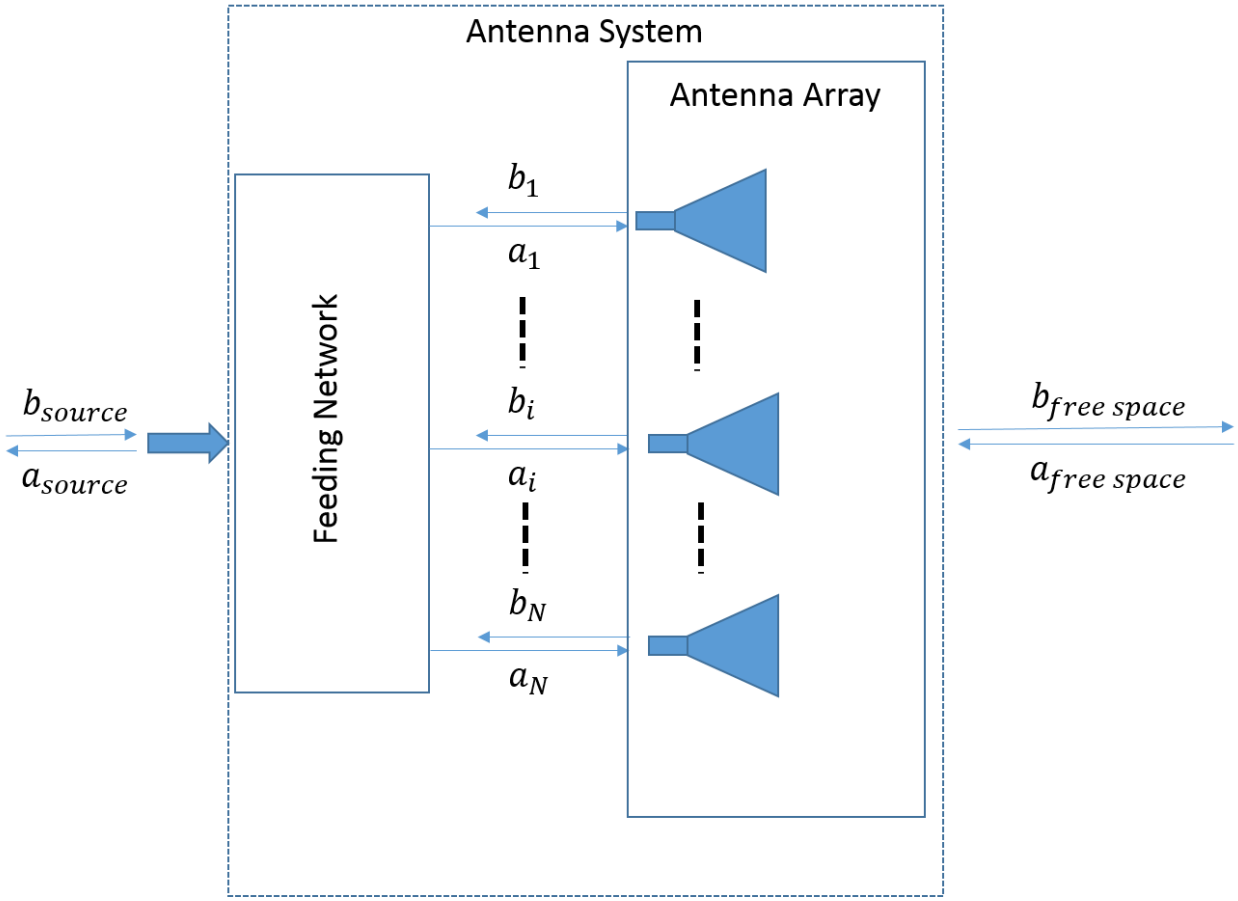

Fig. 1. 2 Scheme of an antenna system with a feeding network and an antenna array.

Using the S parameters one can compute the active reflection coefficient Γ_i of the i-th element on the array using equation (1.4).

$$\Gamma_i = \frac{b_i}{a_i} = \sum_{j=1}^{N} \frac{a_j\, S_{ij}}{a_i} \tag{1.4}$$

where S_{ij} is the scattering matrix entry for elements i and j.

The equation reduces to (1.5) once the array is pointing at broadside and all elements are fed with the same phase and amplitude.

$$\Gamma_i = \sum_{j=1}^{N} S_{ij} \quad , \quad a_k = constant\ for\ k = 1\ to\ N \tag{1.5}$$

Assuming complete symmetry between the elements geometries (e.g. for an infinite uniform array) we can state that the reflection coefficient of the antenna system is equal to the active reflection coefficient of each element (which is the same for all elements) (1.6).

$$\Gamma_{array\ source} = \Gamma_i \quad , \quad infinite\ uniform\ array\ and\ a_k = constant \tag{1.6}$$

1.2.3. Relative Sidelobe Level

The relative sidelobe level (RSLL) is defined in this thesis as the ratio between the largest sidelobe to the main lobe real level (Fig. 1. 3).

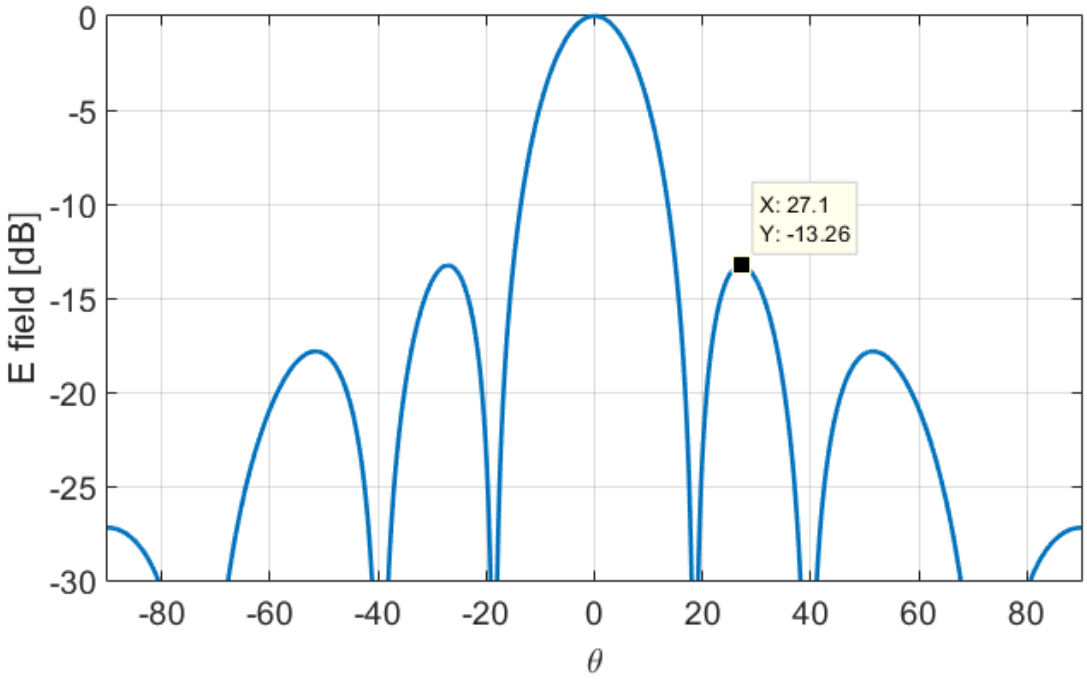

Fig. 1. 3 Arbitrary electric field elevation cut normalized by the main lobe. The relative sidelobe level (RSLL) is equal to -13.26 dB as highlighted.

1.3. Spiral Antennas

Archimedean spiral antennas are wideband antenna elements of the frequency independent type. The frequencies of operation of such antennas are limited by the truncation of their self-similar geometry.

The regions on the Archimedean spiral antenna responsible for radiating are within a circle centered on the spiral with a radius and frequency given by (1.7). Thus, the frequencies of operation of spiral antennas are limited by the inner radius (and thus the dimensions of the feed) and the outer radius (the size of the spiral) (Fig. 1. 4).

When you try using the spiral antenna at lower frequencies eventually the radiation region get to the end of the arms of the spiral. At this point the currents at the end of the arms of the spirals are reflected, which deteriorates the polarization and the reflection coefficient of the spiral antenna.

$$R_{ring} = \frac{c_0}{2\,\pi\,f_0} = \frac{\lambda_0}{2\,\pi} \tag{1.7}$$

where λ_0 is the wavelength at the operation frequency f_0.

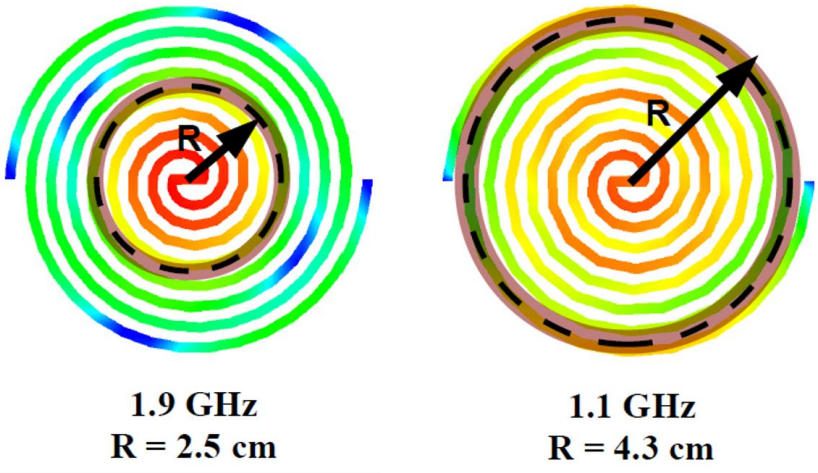

Fig. 1. 4 Normalized current density (30 dB dynamic range from red to blue) along the arms of an Archimedean spiral antenna for different frequencies of operation.

1.4. Antenna Arrays

Antennas can be combined to form an array. Doing so allows for larger gains, electronic steering and other features. In this section we will present a few concepts important for the development of the thesis.

1.4.1. Array Factor

The array factor is a very convenient way of analyzing the behavior of an array. It consists of the radiated field of an array having isotropic point sources. For a planar array in the x-y plane, the array factor is given by (1.8).

$$AF(\theta,\varphi,\theta_s,\varphi_s) = \sum_{n=1}^{N} w_n e^{jk[x_n(\sin\theta\ \cos\varphi - \sin\theta_s\ \cos\varphi_s) + y_n(\sin\theta\ \sin\varphi - \sin\theta_s\ \sin\varphi_s)]} \quad (1.8)$$

with θ,φ the radiation directions and θ_s,φ_s the steering direction of the array, in spherical coordinates.

It is interesting to make a change of variables (1.9) to equation (1.8), which gives (1.10).

$$\begin{aligned} u &= \sin\theta\cos\varphi \\ v &= \sin\theta\sin\varphi \end{aligned} \quad (1.9)$$

$$AF(u,v,u_s,v_s) = \sum_{n=1}^{N} w_n e^{jk[x_n(u-u_s) + y_n(v-v_s)]} \quad (1.10)$$

with u,v the radiation direction (direction cosines) and u_s,v_s the steering direction, in the u v space.

It should be noted that only the values in which $u^2+v^2 \leq 1$ correspond to real angles θ and φ. However, when $u^2+v^2 > 1$ you get information about regions of the array factor that will enter the real space once the array is steered, which is of interest in array factor analysis.

1.4.1.1. Grating Lobes

When the array aperture is under sampled compared to the wavelength (spacing larger than $\lambda/2$) there is the risk that grating lobes appear when the beam is steered of broadside. Grating lobes correspond to the replications of the main beam appearing on the real space. In Fig. 1. 5

we see the array factor of a 3x3 uniform array, using $u\ d_{elem}/\lambda$ and $v\ d_{elem}/\lambda$ as the axis (d_{elem} is the distance between elements in the array in both x and y axis). Because of this normalization of the axis the main beam replications appear at integer values in Fig. 1. 5, which corresponds to values of u and v that are multiples of λ/d_{elem}.

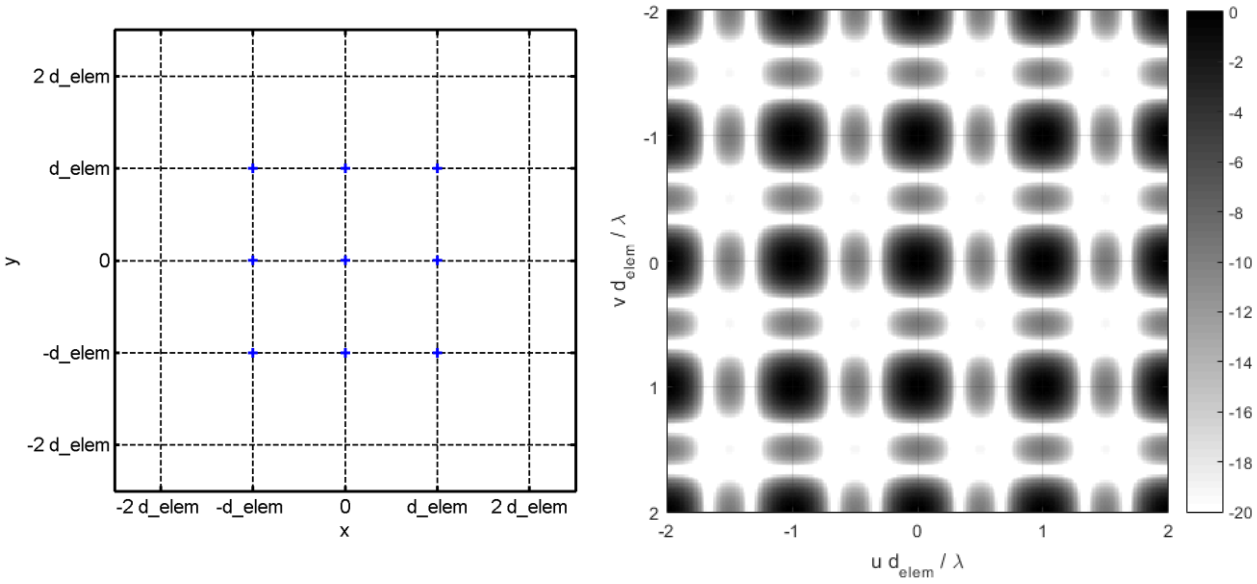

Fig. 1. 5 Elements positions of a 3x3 uniform array with a spacing of d_{elem} (left) and the corresponding AF with the axis normalized by d_{elem}/λ (right). The positions in the array factor where both $u\ d_{elem}/\lambda$ and $v\ d_{elem}/\lambda$ are integer are grating lobes.

1.4.1.2. Array factor region covered when steering up to 30°

At a given frequency, in order to observe all of the sidelobes that appear in the visible zone for an antenna array of isotropic sources steering to all θ_s, φ_s directions up to a maximal elevation angle of θ_0, you must look at the array factor in the region defined by equation (11) (*Lo and Lee, 1965*).

$$u^2 + v^2 \leq (1 + \sin\theta_0)^2 \tag{1.11}$$

In order to obtain this equation we start by defining u, v with relation to the spherical coordinate angles θ, φ (equation (1.9)) and the fundamental relation that defines the visible region (region where θ, φ are real) of the array factor is:

$$u^2 + v^2 = sin^2\theta\ (cos^2\varphi + sin^2\varphi) = sin^2\theta \leq 1 \tag{1.12}$$

So the visible region is defined by a circle of radius 1.

If we consider that the array is steered to θ_s, φ_s the center of the visible region circle is displaced to $[u_s, v_s]$ (*Lo and Lee, 1965*) and thus the visible region in that case is:

$$(u - u_s)^2 + (v - v_s)^2 \leq 1 \tag{1.13}$$

Another relation we can get is the region in the u, v space to which we can steer the array maximum given the maximal elevation angle θ_0:

$$u_s{}^2 + v_s{}^2 = sin^2\theta_s\,(cos^2\varphi_s + sin^2\varphi_s) = sin^2\theta_s \leq sin^2\theta_0 \tag{1.14}$$

which is true because $\theta_s \leq\ \theta_0 \leq\ \pi/2$ (you cannot steer an array backwards). We can rewrite equations (1.13) and (1.14) as follows:

$$\begin{gathered} r' = |(u - u_s\,, v - v_s)| \leq 1 \\ r_s = |(u_s, v_s)| \leq\ \sin\theta_0 \end{gathered} \tag{1.15}$$

with r' being the distance of the point $(u - u_s\,, v - v_s)$ to the origin of the u, v space and r_s the distance of the point (u_s, v_s) to the origin of the u, v space. It will be useful later in the demonstration to rewrite these points as follows:

$$\begin{gathered} (u, v) = (r\ \cos\omega\,, r\ \sin\omega) \\ (u_s, v_s) = (r_s\ \cos\omega_s\,, r_s\ \sin\omega_s) \\ (u - u_s\,, v - v_s) = \ (r'\ \cos\omega'\,, r'\ \sin\omega') \end{gathered} \tag{1.16}$$

with r, r', r_s being the distance of the points to the origin and $\omega, \omega', \omega_s$ the angle between the u axis and the vector going from the origin to the point.

Coming back to the original problem, in order to find the region that covers all of the visible sidelobes up to an elevation angle of θ_0 it is sufficient to find the largest region in the u, v space that obeys equation (1.15):

$$\begin{gathered} max(|(u, v)|^2), given \\ r' = |(u - u_s\,, v - v_s)| \leq 1 \\ r_s = |(u_s, v_s)| \leq\ \sin\theta_0 \end{gathered} \tag{1.17}$$

which can be solved as follows:

$$\begin{gathered} (u, v) = (u - u_s\,, v - v_s) + (u_s, v_s) \\ max(|(u, v)|^2) = max(|(u - u_s\,, v - v_s) + (u_s, v_s)|^2) \end{gathered} \tag{1.18}$$

$$= max(|(r'\ \cos\omega', r'\ \sin\omega') + (r_s\ \cos\omega_s, r_s\ \sin\omega_s)|^2)$$

$$= max(|(r'\cos\omega' + r_s\ \cos\omega_s, r'\sin\omega' + r_s\ \sin\omega_s)|^2)$$

$$= max\big(r'^2(cos^2\omega' + sin^2\omega') + {r_s}^2(cos^2\omega_s + sin^2\omega_s) + r_s r'(\cos\omega_s \sin\omega' + \sin\omega_s \cos\omega')\big)$$

$$= max(r'^2 + {r_s}^2 + r_s r' \sin(\omega_s + \omega'))$$

As $\sin(\omega_s + \omega')$ is maximal when it is equal to one we get:

$$max(|(u,v)|^2) = max((r' + r_s)^2) \tag{1.19}$$

which is maximal when both r' and r_s are maximal, so using equations (1.15) and (1.19) we get:

$$max(|(u,v)|^2) = (1 + \sin\theta_0)^2 \tag{1.20}$$

which validates equation (1.11).

1.4.1.3. One Ring Array

In Fig. 1. 6 we show the AF of a one ring array calculated at 2 GHz inside the region defined by $u^2 + v^2 \leq\ 1.5^2$, which contains all the sidelobes that can appear in the visible zone at 2 GHz for a maximal steering of $\theta_s = 30^o$ (see equation (1.11)). The array has 28 elements (N_{el}) uniformly spaced in a ring with 1.085 meters of radius (R). The length of the arc between elements is $d_{elem} = 2\pi R/N_{el}$.

By looking at the AF with the u-v axes normalized by d_{elem}/λ, we observe high sidelobes in the rings with an integer radius, corresponding to the grating lobe regions. In a concentric ring array we should expect to have the larger sidelobes appearing in those regions.

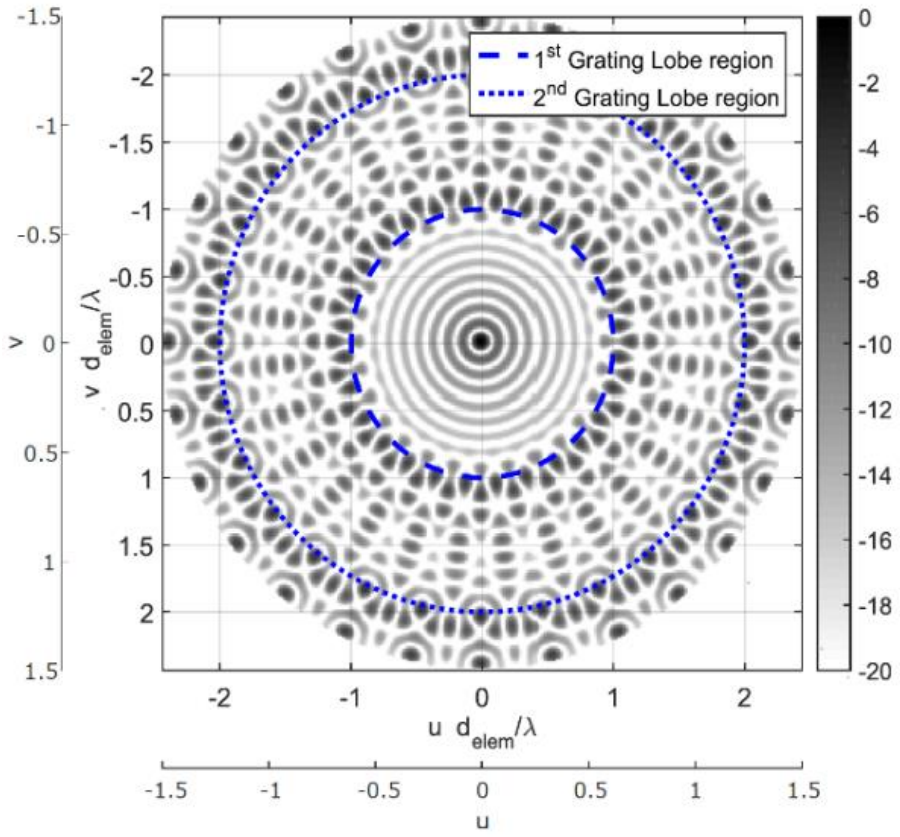

Fig. 1. 6 Array Factor of a one ring array with a radius of 1.085 m and 28 elements uniformly spaced, showing all sidelobes that appear in the visible zone at 2 GHz for a maximal steering of $\theta_s = 30^o$. The u-v axes are shown for the AF at 2 GHz, as well as the axis normalized by d_{elem}/λ. The 1st (dashed) and 2nd (dotted) Grating Lobe (GL) regions are highlighted in the Array Factor.

1.5. Wideband arrays

When designing wideband arrays there are several techniques used to enhance the bandwidth of the array. In this section we will discuss some of these techniques.

1.5.1. Connecting element approaches

One of the common techniques used in the design of wideband arrays takes advantage of the coupling between elements in order to extend their bandwidth to the lower frequencies.

(*Munk et al., 2003*) developed an array with intentional coupling between dipoles (Fig. 1. 7). (*Hansen, 2004*) presents the currents on a linear array of connected dipoles. These

contributions laid the groundwork for the trend of connecting elements in the design of wideband antenna arrays.

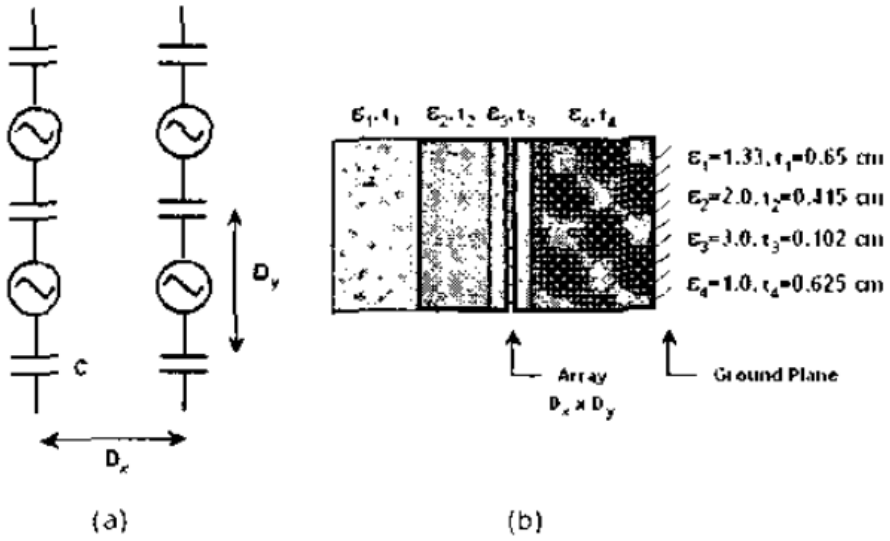

Fig. 1. 7 (a) Circuit model (b) Dielectric Profile (Munk et al., 2003)

(*Neto et al., 2009*), (*Cavallo et al., 2013*) and (*Bolt et al., 2016*) developed theoretical models for the design of connected dipole arrays (Fig. 1. 8) as well as special feeds using loop-shaped transformers to avoid common-mode resonances, allowing for the design of prototypes of single polarized (Fig. 1. 9) and dual polarized (Fig. 1. 10) arrays of connected dipoles. (*Konkol et al., 2017*) presented another way of feeding connected arrays by using high-power photo-diodes.

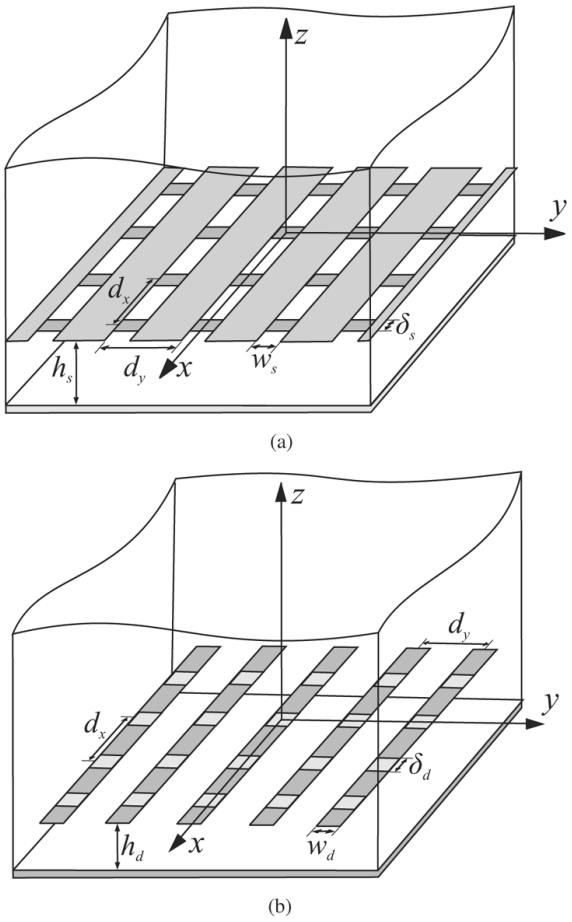

Fig. 1. 8 Geometries of 2-D connected arrays of (a) slots and (b) dipoles with backing reflector (Neto et al., 2009).

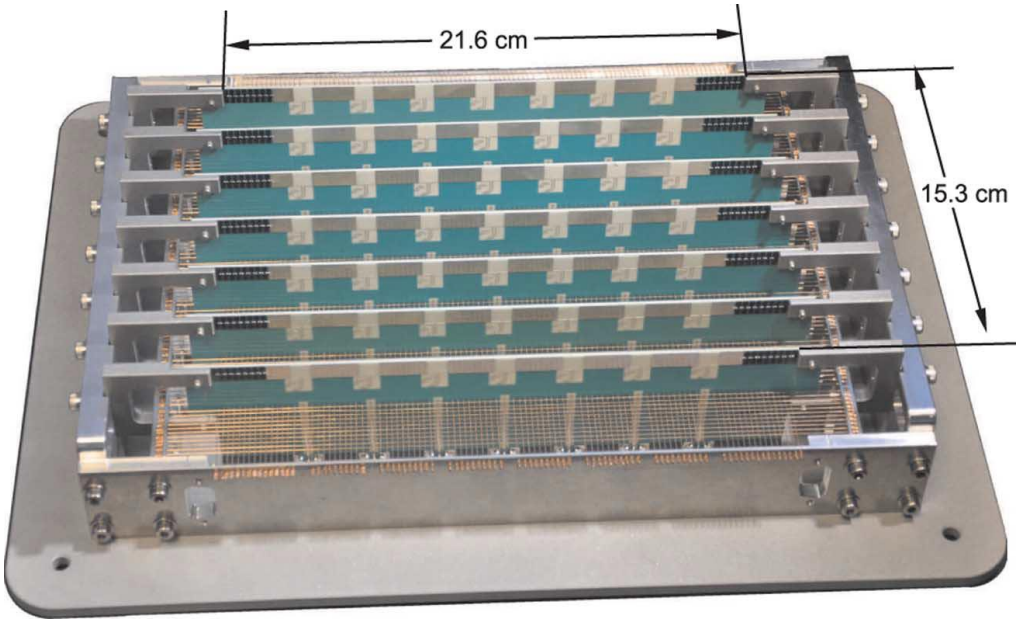

Fig. 1. 9 7x7 prototype array (of connecting dipoles) with dimensions (Cavallo et al., 2013)

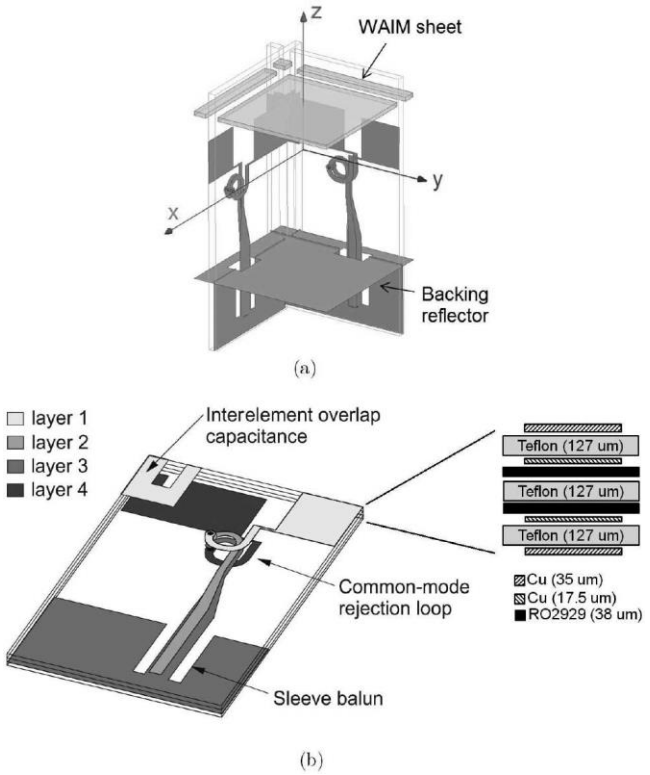

Fig. 1. 10 (a) Three-dimensional view of the array unit cell and (b) components of the dipole and the feed structure in the multilayer PCB. (Bolt et al., 2016)

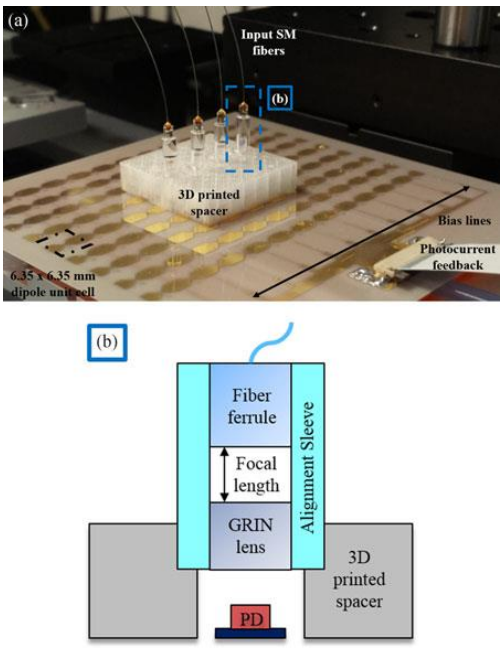

Fig. 1. 11 (a) The array after alignment of 4 single mode fibers and lens assemblies to the active elements. (b) Schematic of the optical alignment technique used to illuminate the photodiodes (Konkol et al., 2017).

(*Varault et al., 2017*) developed a wideband dual polarized self-complementary connected array antenna with low radar cross section under normal and oblique incidence.

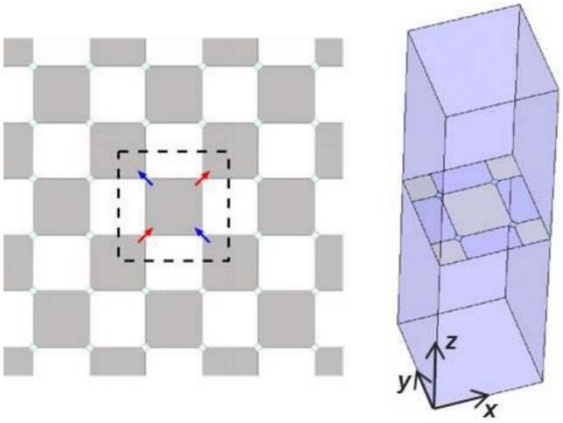

Fig. 1. 12 Self-complementary connected array aperture and unit cell (Varault et al., 2017).

(*Holland and Vouvakis, January 2012*), (*Holland et al., October 2012*) and (*Logan et al., 2018*) also used highly coupled elements to develop Planar Ultrawideband Modular Antenna (PUMA) arrays, which despite the complex design offers the advantage of being modular, thus facilitating the manufacture of such arrays (Fig. 1. 13 and Fig. 1. 14).

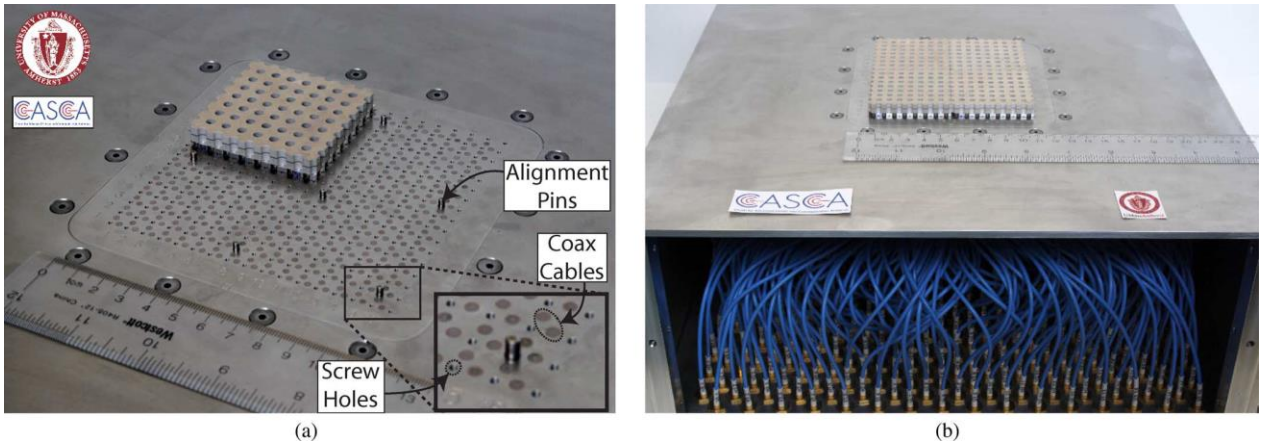

Fig. 1. 13 Modular and solderless assembly of a 16x16 dual-polarized PUMA array prototype on the measurement fixture. (a) Top plate of the fixture and the mounting of an 8x8 module. (b) Full array mounted on measurement fixture, with the side panel removed to show the coaxial cables exiting the top plate and terminating in SMA connectors on the backside of the fixture (Holland et al., October 2012).

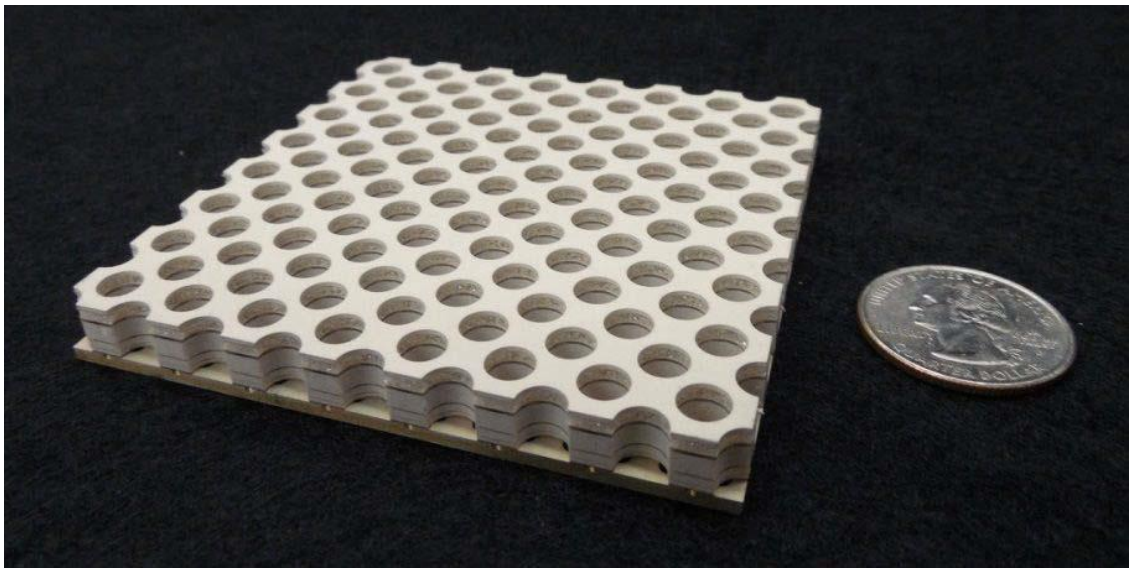

Fig. 1. 14 6:1 dual-polarized 256-port PUMA prototype array (128 elements per polarization) (Logan et al., 2018).

(*Alvan et al., 2012*) and (*Tzanidis et al., 2011*) have explored the use of interwoven spirals to obtain larger bandwidth due to the capacitive coupling between the arms of the neighboring spirals (Fig. 1. 15).

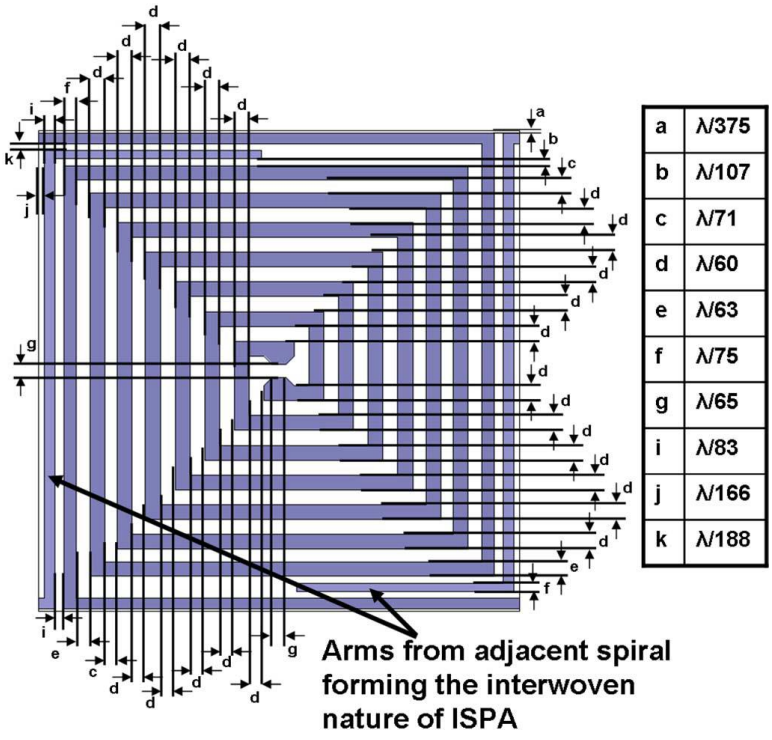

Fig. 1. 15 Interwoven Spiral Array (ISPA) unit cell and its dimensions in wavelengths. The element is fed at the center. (Tzanidis et al., 2011)

(*Guinvarc'h et al., 2012*) studied arrays with connected spirals of opposite polarization alternated in a linear array to improve the bandwidth by reducing the lowest frequency of operation by a factor of 1.32 (Fig. 1. 16). The connections allow for the currents of the spiral to flow to the neighboring spiral instead of being reflected, thus reducing the reflection coefficient in the lower frequencies. In addition, such an array would be able to produce dual circular polarization.

Fig. 1. 16 Linear array of connecting spirals with cavity (Guinvarc'h et al., 2012).

1.5.2. Sequential rotation of spiral elements

In order to obtain a good circular polarization one of the available methods is to use sequential rotation of adjacent elements (*Huang, 1986*) (*Louertani et al., 2011*). This technique consists of disposing the antenna elements in a ring, rotating the elements, and phasing them by an amount equal to their angular position.

The array in Fig. 1. 16 has a high axial ratio in the lower frequencies. (*Hinostroza et al., 2016*) has proposed to arrange the spirals in a circle (Fig. 1. 17) so that the sequential rotation could be applied, which resulted in a low axial ratio over the whole bandwidth of the array.

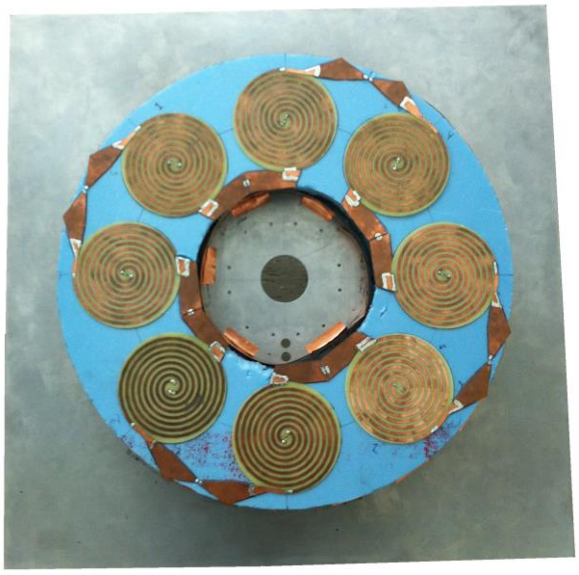

Fig. 1. 17 Ring array of connecting spirals with cavity (Hinostroza et al., 2016).

1.5.3. Grating lobe suppression

One of the limiting factors of wideband arrays is the presence of grating lobes. As the frequency rises the spacing between elements becomes wider in comparison to the wavelength and grating lobes appear in real space. To address this problem one can either bring the elements closer together, which usually implies the use of smaller elements that reduces bandwidth in the lower frequencies, or break the periodicity that causes the grating lobes, for instance by the use of non-uniform arrays.

Several techniques have been proposed to obtain the geometry of such arrays, including deterministic methods (*Haupt, 1995*), Genetic Algorithms (*Haupt, 2008*), (*Hinostroza et al., 2014*) (Fig. 1. 18), compressive-sensing (*Bencivenni et al., 2016*), etc…

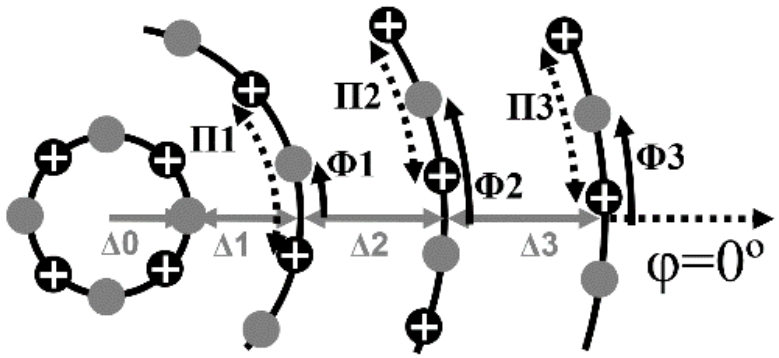

Fig. 1. 18 Concentric ring array: filled and cross circles represent RH and LH polarized spirals, respectively. Interleaved spirals make the array sparse, so high lobes ("grating lobes") appear in the radiating visible zone. Concentric rings with radius and relative rotations optimized to reduce those lobes can enhance the RSLL in higher frequencies.

Another way of avoiding grating lobes is by using wideband arrays with variable element size (*Shively and Stutzman, 1990*), (*Caswell, 2001*). In such arrays the elements of different sizes share the same aperture to cover different bandwidths. (*Lee et al., 2016*) designed a PUMA array with a scaled down subarray sharing the aperture to extend the overall bandwidth (Fig. 1. 19)

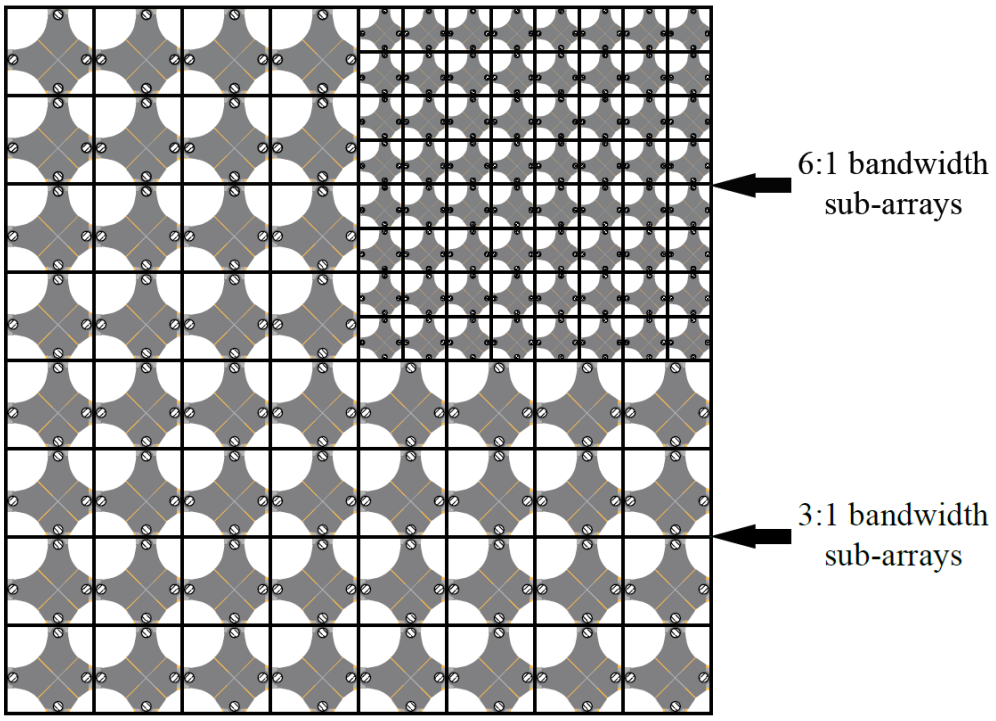

Fig. 1. 19 Sub-array view of a PUMA wavelength-scaled array (L-shape configuration) consisting of a 8 x 8 6:1 PUMA sub-array with three 4 x 4 3:1 PUMA sub-arrays (Lee et al., 2016).

1.6. Conclusion of chapter 1

In this chapter we introduced concepts key to the development of the thesis. We presented the parameters that define the requirement of the arrays developed in this thesis and the radiating mechanism of spiral antennas.

We discussed concepts on antenna arrays including the array factor as a tool for the analysis of arrays, the apparition of grating lobes due to the periodicity in an array's structure as well as several trends on the development of wideband antenna arrays, including the exploration of the mutual coupling between elements, the use of the sequential rotation technique to improve the polarization characteristics of circularly polarized arrays as well as the use of non-uniform spacing to break the periodicity of an array and thus avoid grating lobes.

References

Alvan, E. A., Sertel, K. and Volakis, J. L., “A Simple Equivalent Circuit Model for Ultrawideband Coupled Arrays,” *IEEE Antennas and Wireless Propagation Letters*, vol. 11, pp. 117-120, January 2012.

Bencivenni, C., Ivashina, M. V., Maaskant, R. and Wettergren, J., “Synthesis of Maximally Sparse Arrays Using Compressive Sensing and Full-Wave Analysis for Global Earth Coverage Applications,” *IEEE Transactions on Antennas and Propagation*, vol. 64, no. 11, pp. 4872-4877, November 2016.

Bolt, R. J., Cavallo D., Gerini G., Deurloo D., Grooters R., Neto, A. and Toso, G., “Characterization of a Dual-Polarized Connected-Dipole Array for Ku-Band Mobile Terminals,” *IEEE Transactions on Antennas and Propagation*, vol. 64, no. 2, pp. 591-598, February 2016.

Caswell, E. D., “Design and Analysis of Star Spiral with Application to Wideband Arrays with Variable Element Sizes,” Ph.D. dissertation, Virginia Polytechnic Institute and State University, Virginia, USA, 2001.

Cavallo, D., Neto, A., Gerini, G., Micco, A. and Galdi, V., “A 3- to 5- GHz Wideband Array of Connected Dipoles With Low Cross Polarization and Wide-Scan Capability,” *IEEE Transactions on Antennas and Propagation*, vol. 61, no. 3, pp. 1148-1154, March 2013.

Guinvarc'h, R., Serhir, M. and Ribière-Tharaud, N., “A cavity-backed dual polarized array of connected spiral antennas,” *Proceedings of the 2012 IEEE International Symposium on Antennas and Propagation (APSURSI)*, July 2012.

Hansen, R. C., “Linear Connected Arrays,” *IEEE Antennas and Wireless Propagation Letters*, vol. 3, pp. 154-156, 2004.

Haupt, R. L., “Unit circle representation of aperiodic arrays,” *IEEE Transactions on Antennas and Propagation*, vol. 43, no. 10, pp. 1152-1155, October 1995.

Haupt, R. L., “Optimized element spacing for low sidelobe concentric ring arrays,” *IEEE Transactions on Antennas and Propagation*, vol. 56, no. 1, pp. 266-268, January 2008.

Hinostroza, I., Guinvarc'h, R., Haupt, R. L. and Louertani, K., “A dual-polarized Wideband Planar Phased Array with Spiral Antennas,” *IEEE Transactions on Antennas and Propagation*, vol. 62, no. 9, pp. 4547-4553, June 2014.

Hinostroza, I., Guinvarc'h, R., Haupt, R. L. and Louertani, K., “A 6:1 Bandwidth, Low-Profile, Dual-Polarized Ring Array of Spiral Antennas with Connecting Arms,” *IEEE Transactions on Antennas and Propagation*, vol. 64, no. 2, pp. 752-756, February 2016.

Holland, S. S. and Vouvakis, M. N., “The Planar Ultrawideband Modular Antenna (PUMA) Array,” *IEEE Transactions on Antennas and Propagation*, vol. 55, no. 2, pp. 305-312, January 2012.

Holland, S. S., Schaubert, D. H. and Vouvakis, M. N., “A 7-21 GHz Dual-Polarized Planar Ultrawideband Modular Array Antenna (PUMA) Array,” *IEEE Transactions on Antennas and Propagation*, vol. 60, no. 10, pp. 4589-4600, October 2012.

Huang, J., “A technique for an array to generate circular polarization with linearly polarized elements,” *IEEE Transactions on Antennas and Propagation*, vol. 34, no. 9, pp. 1113-1124, September 1986.

Konkol, M. R., Ross, D. D., Shi, S., Harrity, C. E., Wright, A. A., Schuetz, C. A., Prather and D. W., “High-Power Photodiode-Integrated-Connected Array Antenna,” *Journal of Lightwave Technology*, vol. 35, no. 10, pp. 2010-2016, February 2017.

Lee, M. Y., Kindt, R. W. and Vouvakis, M. N., “Planar Ultrawideband Modular Antenna (PUMA) Wavelength-Scaled Array,” *Proceedings of the 2016 IEEE International Symposium on Antennas and Propagation (APSURSI)*, 26 June – 1 July 2016.

Lee, J., Pottier, E., *Polarimetric radar imaging: from basics to applications*, CRC Press, Boca Raton, FL, USA, 2009.

Lo, Y. T. and Lee, S. W., “Affine Transformation and Its Application to Antenna Arrays,” *IEEE Transactions on Antennas and Propagations*, vol. 13, no.6, pp. 890-896, November 1965.

Logan, J. T., Kindt, R. W., Lee, M. Y. and Vouvakis, M. N., “A New Class of Planar Ultrawideband Modular Antenna Arrays With Improved Bandwidth,” *IEEE Transactions on Antennas and Propagation*, vol. 66, no. 2, pp. 692-701, February 2018.

Louertani, K., Guinvarc'h, R., Ribière_Tharaud, N. and Hélier, M., "Study of the Radiated Polarization of an Antenna Array with Circular Geometry," *Progress In Electromagnetics Research C*, vol. 24, pp. 173-183, 2011.

Munk, B., Taylor, R., Durham, T., Croswell, W., Pigon, B., Boozer, R., Brown, S., Jones, M., Pryor, J., Ortiz, S., Rawnick, J., Krebs, K., Vanstrum, M., Gothard, G. and Wiebelt, D. (2003), A Low-Profile Broadband Phased Array Antenna, *Proceedings of the 2003 IEEE Antennas and Propagation Society International Symposium (APSURSI)*, vol. 2, pp. 448-451, June 2003.

Neto, A., Cavallo, D., Gerini, G. and Toso, G., "Scanning Performances of Wideband Connected Arrays in the Presence of a Backing Reflector," *IEEE Transactions on Antennas and Propagation*, vol. 57, no. 10, pp. 3092-3102, October 2009.

Shively, D. G. and Stutzman, W. L., "Wideband arrays with variable element sizes," *IEE Proceedings H – Microwaves, Antennas and Propagation*, vol. 137, no. 4, pp. 238-240, August 1990.

Tzanidis, I., Sertel, K. and Volakis, J. L., "Interwoven Spiral Array (ISPA) With a 10:1 Bandwidth on a Ground Plane," *IEEE Antennas and Wireless Propagation Letters*, vol. 10, pp. 115-118, 2011.

Varault, S., Soiron, M., Barka, André, Lepage, A. C. and Begaud, X., "RCS Reductions With a Dual Polarized Self-Complementary Connected Array Antenna," *IEEE Transactions on Antennas and Propagation*, vol. 65, no. 2, pp. 567-575, February 2017.

Chapter 2: Concentric Ring Array

2.1. Introduction

(*Guinvarc'h et al., 2012*) found that by connecting spirals of opposite polarization alternated in a linear array (Fig. 2. 1) one can improve the bandwidth by reducing the lowest frequency of operation by a factor of 1.32. In addition, such an array is able to produce dual circular polarization.

Fig. 2. 1 Linear array of connecting spirals with cavity (Guinvarc'h et al., 2012).

However, such an approach comes with a cost. The spirals of opposite polarization sharing a cavity radiate with a high Axial Ratio at low frequencies. Moreover, as there is an element in between spirals of the same polarization, the inter element spacing is necessarily large, which means that grating lobes are bound to appear at lower frequencies than in a usual uniform single polarized array.

In order to overcome the issue with the polarization purity it has been proposed to use a ring array topology (Fig. 2. 2, *Hinostroza et al., 2016*). By placing the spirals in a ring arrangement it is possible to use the sequential rotation technique to improve the polarization quality (*Huang,* 1986), (*Louertani et al.,* 2011), while the connections between the spirals reduce the lowest operating frequency.

With this design the array is still sparse and, thus, the bandwidth is limited by the appearance of grating lobes. In order to mitigate those lobes while keeping the array's advantages, it has been proposed to use non-uniform concentric ring arrays (*Hinostroza et al., 2014*). With the added non uniformity, the grating lobes can be mitigated, thus extending the array bandwidth in the higher frequencies.

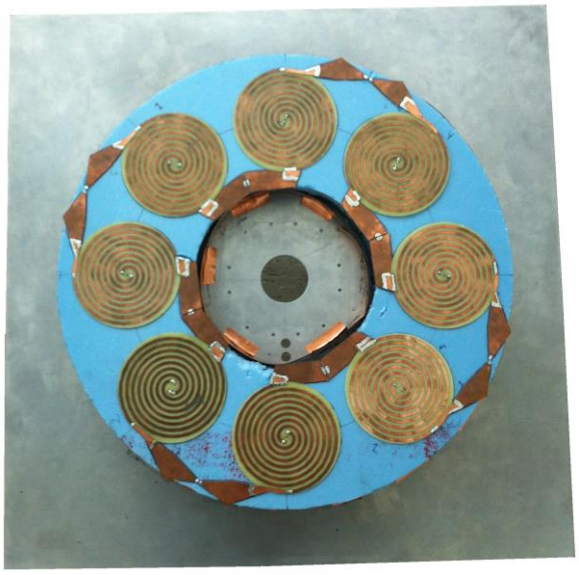

Fig. 2. 2 Ring array of connecting spirals with cavity (Hinostroza et al., 2016).

The parameters of a concentric ring array are the element spacing, which was selected to accommodate the spiral elements of both polarizations and their connections, and the number of rings, their radius and their relative rotation (Fig. 2. 3). Genetic Algorithms have been used to minimize the highest sidelobe level visible at the highest frequency of operation while steering up to 30 degrees, assuming array elements radiate as isotropic sources. The optimization process succeeded in mitigating the Grating Lobes, however the obtained array was too big to fit in a reasonable sized platform (4.22 meters diameter).

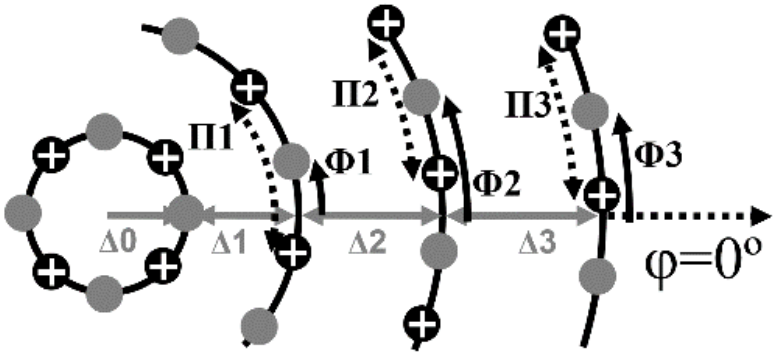

Fig. 2. 3 Concentric ring array: filled and cross circles represent RH and LH polarized spirals, respectively. Interleaved spirals make the array sparse, so high lobes ("grating lobes") appear in the radiating visible zone. Concentric rings with radius and relative rotations optimized to reduce those lobes can enhance the RSLL in higher frequencies.

The first issue that we will tackle in this chapter is the implementation of the connections in the concentric ring array. Next we look into how to optimize this array to obtain a more compact array with the same features: large bandwidth, dual circular polarization, steering up to 30 degrees and good axial ratio. Then, we will show how to use the WAVES technique (*Shively and Stutzman, 1990*) to further extend the bandwidth of the array while keeping the design compact.

It should be noted that, combining the concentric ring array design in (*Hinostroza et al., 2014*) and the connections between spirals in (*Hinostroza et al., 2016*), the array has been designed to work between 0.3 and 2.1 GHz (*Hinostroza, 2013*). In this work we decided to use a different bandwidth, so we applied a scaling on those designs in order to work on a comparable scenario. This way, the array is downscaled by a 3.3 factor, which means that the corresponding bandwidth of the Concentric Ring Array (CRA) of connecting spirals goes from 1-6.9 GHz and has a diameter of 1.28 meters.

2.2. Concentric Ring Array of Connecting Spirals

In (*Hinostroza, 2013*) the final design consists of combining non-uniform concentric rings to mitigate the grating lobes (Fig. 2. 3) with the connections between the arms of Archimedean spirals of opposing polarization to enhance the reflection coefficient in the lower frequencies (Fig. 2. 2).

In this chapter the first step we take is to implement the connections in the concentric ring array. Then, will work on reducing the size of the array.

2.2.1. Concentric Ring Array Geometry

A diagram of the concentric ring array, which has $N_r = 4$ rings, appears in Fig. 2. 3. Variables in the i-th ring design ($i = 0, \dots, N_r - 1$) include the ring spacing Δ_i and the ring rotation angle Φ_i. The array consists of connected Archimedean spirals with a diameter of $D_{spi} = 3.18$ cm and a lower operating-frequency of 1 GHz (due to the connections (*Hinostroza et al., 2016*)). The spacing between elements of the same polarization within a ring has an approximate value of

$d_{elem} = 7.37$ cm (*Hinostroza et al., 2014*). Every other element in a ring is RH (right hand) polarized, while the others are LH (left hand) polarized.

The number of spirals of the same polarization (N_i) in a ring of radius r_i is determined by:

$$N_i = \left\lfloor \frac{2\,\pi\,r_i}{d_{elem}} \right\rfloor, \tag{2.1}$$

where $\lfloor x \rfloor$ is the floor function, to round down the value of N to a integer value. The number of spirals in the i-th ring is thus equal to $2\,N_i$, with N_i right handed polarized spirals and N_i left handed polarized spirals.

We can then calculate the angular distance Π_i between two elements of the same polarization as follows:

$$\Pi_i = \frac{2\,\pi}{N_i} \tag{2.2}$$

The values of the ring rotations are restricted to $0 \leq \Phi_i \leq \Pi_i$. Indeed, the resulting concentric ring arrays with $\Phi_i = cte + k\,\Pi_i, k = 0,1,2 \ldots$ are all equivalent.

2.2.2. Connections Re-Optimization

In order to extrapolate the optimized results from the one-ring array in Fig. 2. 2 to the other rings in a CRA the simplest solution is to normalize the optimized parameters and transpose the results for the larger rings. As an example we present the optimized parameters in Fig. 2. 4 and Table 2. 1 with the optimized results from (*Hinostroza et al., 2016*), and then show how to transpose the results for another ring.

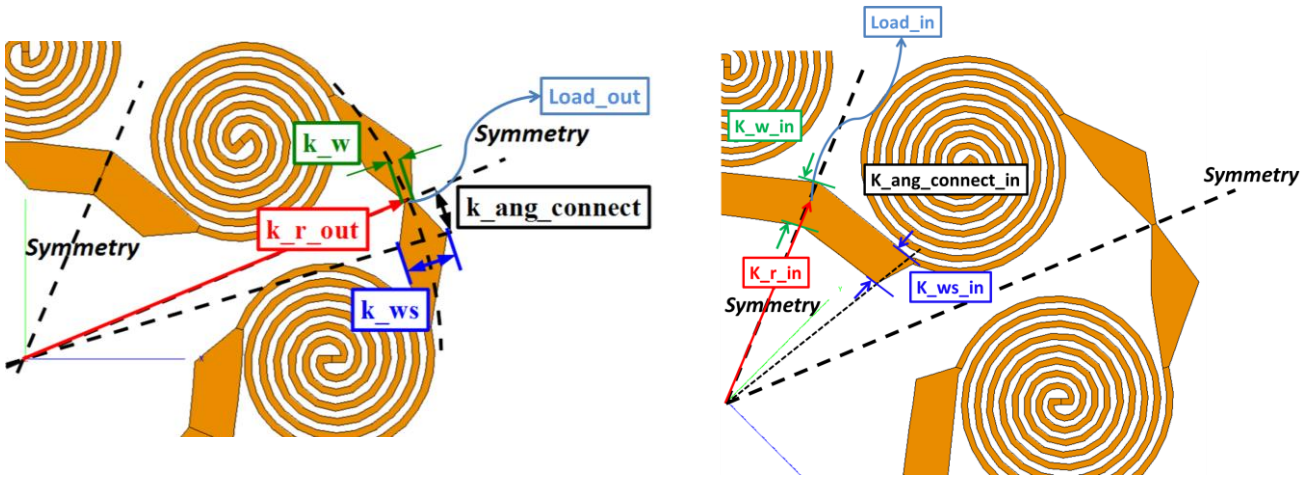

Fig. 2. 4 Connections optimization parameters (Hinostroza et al., 2016)

Table 2. 1 Connections parameters optimum values (Hinostroza et al., 2016)

Symbol	Optimum Value	Description
Load_in	101 ohm	Load in inner conn.
K_r_in	9.92 cm	Dist. center to middle of inner conn.
K_w_in	2.15 cm	Width at middle of inner conn.
K_ws_in	2 cm	Width out of middle of inner conn.
K_ang_connect_in	29.2°	Angular distance from symmetry line for inner conn.
Load_out	197 ohm	Load in outer conn.
k_r_out	21.45 cm	Dist. center to middle of outer conn.
k_w	0.2 cm	Width at middle of outer conn.
k_ws	2.3 cm	Width out of middle of outer conn.
k_ang_connect	8.3°	Angular distance from symmetry line for outer conn.

In order to bring those parameters to our framework we scale the distances by a factor of 3.3:

Table 2. 2 Connections parameters optimum values from Table 2. 1 scaled down by a factor 3.3. Ring radius R = 4.69 cm.

Symbol	Optimum Value
load_in	101 ohm
k_r_in	3.01 cm
k_w_in	0.65 cm
k_ws_in	0.61 cm
k_ang_connect_in	29.2°
load_out	197 ohm
k_r_out	6.5 cm
k_w	0.06 cm
k_ws	0.7 cm
k_ang_connect	8.3°

The load values (load_in and load_out) and the connection widths at the different points of the connection (k_w_in, k_ws_in, k_w and k_ws) can be kept the same between different rings.

The parameters k_r_in and k_r_out assume the center of the array is the reference. To extrapolate those parameters from one ring to the next we must compensate for the difference in the ring's radius.

As for the angular parameters k_ang_connect_in and k_ang_connect, it is easy to normalize those by the angular distance between elements of the same polarization in order to extrapolate the parameter from one ring to the next.

Applying those changes produces the new values in Table 2. 3:

Table 2. 3 Connections parameters optimum values scaled down by a factor 3.3, transposed for the jth ring (with radius R_j and angle between spirals of the same polarization Π_j)

Symbol	Optimum Value	$R_j = 4.69\ cm,\ \Pi_j = 90°$ Fig. 2. 2 and Fig. 2. 5 (a)	$R_j = 31.5\ cm,\ \Pi_j = 13.3°$ Fig. 2. 5 (b)
load_in	101 ohm	-	-
k_r_in	R_j – 1.68 cm	3.01 cm	29.8 cm
k_w_in	0.65 cm	-	-
k_ws_in	0.61 cm	-	-
k_ang_connect_in	0.32444 Π_j	29.2°	4.3°
load_out	197 ohm	-	-
k_r_out	R_j + 1.80 cm	6.5 cm	33.3 cm
k_w	0.06 cm	-	-
k_ws	0.7 cm	-	-
k_ang_connect	0.09222 Π_j	8.3°	1.2°

The one-ring array from Fig. 2. 2 has a radius (4.69 cm) that is significantly smaller than that of the larger rings in the concentric ring array (up to 64 cm). As explained, the parameters of the connections in the smaller ring can be extrapolated to the connections of the rings with different radius, but when the difference in radius is too large the connections on the ring arrays with larger radius are deformed (Fig. 2. 5). To address this problem the connections need to be re-optimized.

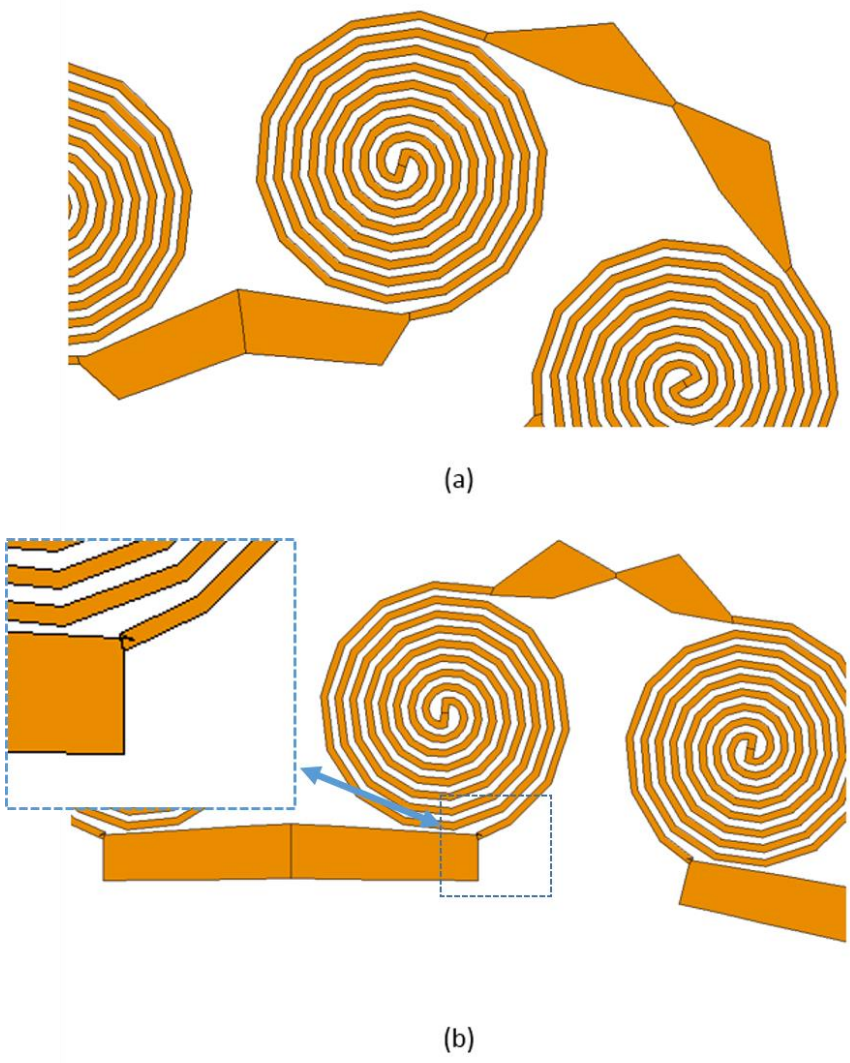

Fig. 2. 5 Connections between spirals in a ring array for an array with 4 spirals per polarization (a) and for an array with 27 elements per polarization (b). The parameters used for the connections are listed in Table 2. 3.

For the re-optimization of the connections we considered a ring with a larger radius and, thus, more elements, so that the connections optimized in such a ring array can be transposed to rings of different radius with similar performances. The optimization of the parameters was made using Opt FEKO (*Hinostroza et al., 2016*), but this time for a ring array with 16.95 cm radius and 14 spiral elements per polarization (with the spiral diameters being 3.18 cm). The results are shown in Table 2. 4.

Table 2. 4 Connections parameters optimum values – re-optimization with ring radius of 16.95 cm and 14 elements per polarization

Symbol	Optimum Value	$R_j = 4.69\ cm$, $\Pi_j = 90°$	$R_j = 16.95\ cm$, $\Pi_j = 25.7°$	$R_j = 31.5\ cm$, $\Pi_j = 13.3°$
load_in	0.16 ohm	-	-	-
k_r_in	R_j - 1.97 cm	2.72 cm	14.98 cm	29.53 cm
k_w_in	0.85 cm	-	-	-
k_ws_in	0.76 cm	-	-	-
k_ang_connect_in	0.5161 Π_j	46.5°	13.3°	6.9°
load_out	223 ohm	-	-	-
k_r_out	R_j + 1.80 cm	6.49 cm	18.75 cm	33.3 cm
k_w	0.09 cm	-	-	-
k_ws	0.85 cm	-	-	-
k_ang_connect	0.1321 Π_j	11.9°	3.4°	1.8°

2.2.3. FEKO Simulation

Using the new parameters for the connections we simulated the CRA from (*Hinostroza, 2014*) but now incorporated the connections from the new optimization. As mentioned before, we also scaled it down by a factor of 3.3. In Fig. 2. 6 we show the element positions and the top view of the array in the FEKO model.

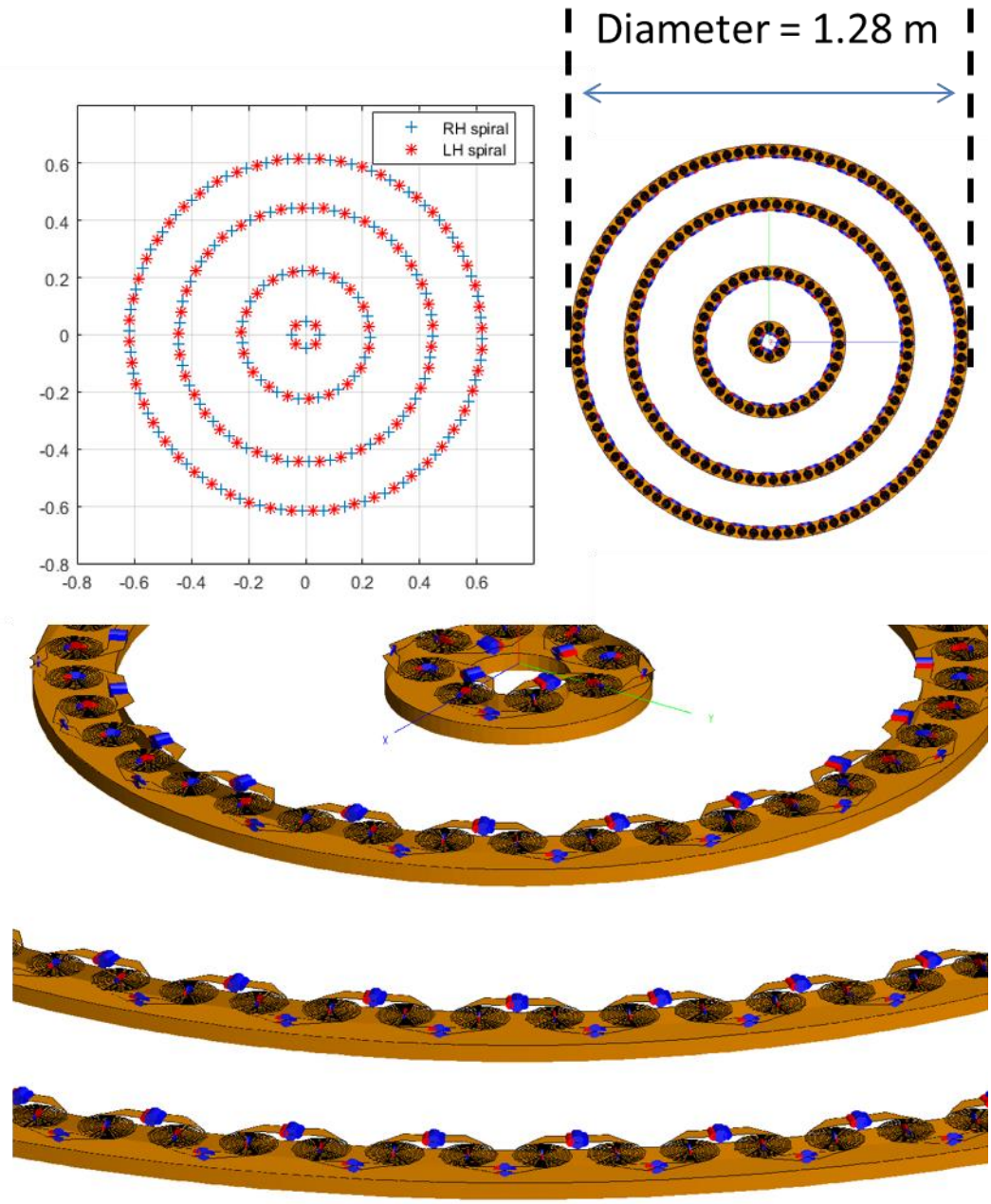

Fig. 2. 6 Element locations, Top view of the FEKO model and isometric view of the FEKO model for the concentric ring array from (Hinostroza et al., 2014) with added connections between spirals.

The simulation results are shown for two scenarios: pointing at broadside (Fig. 2. 7) and steered to 30° (Fig. 2. 9) for the RHC polarization.

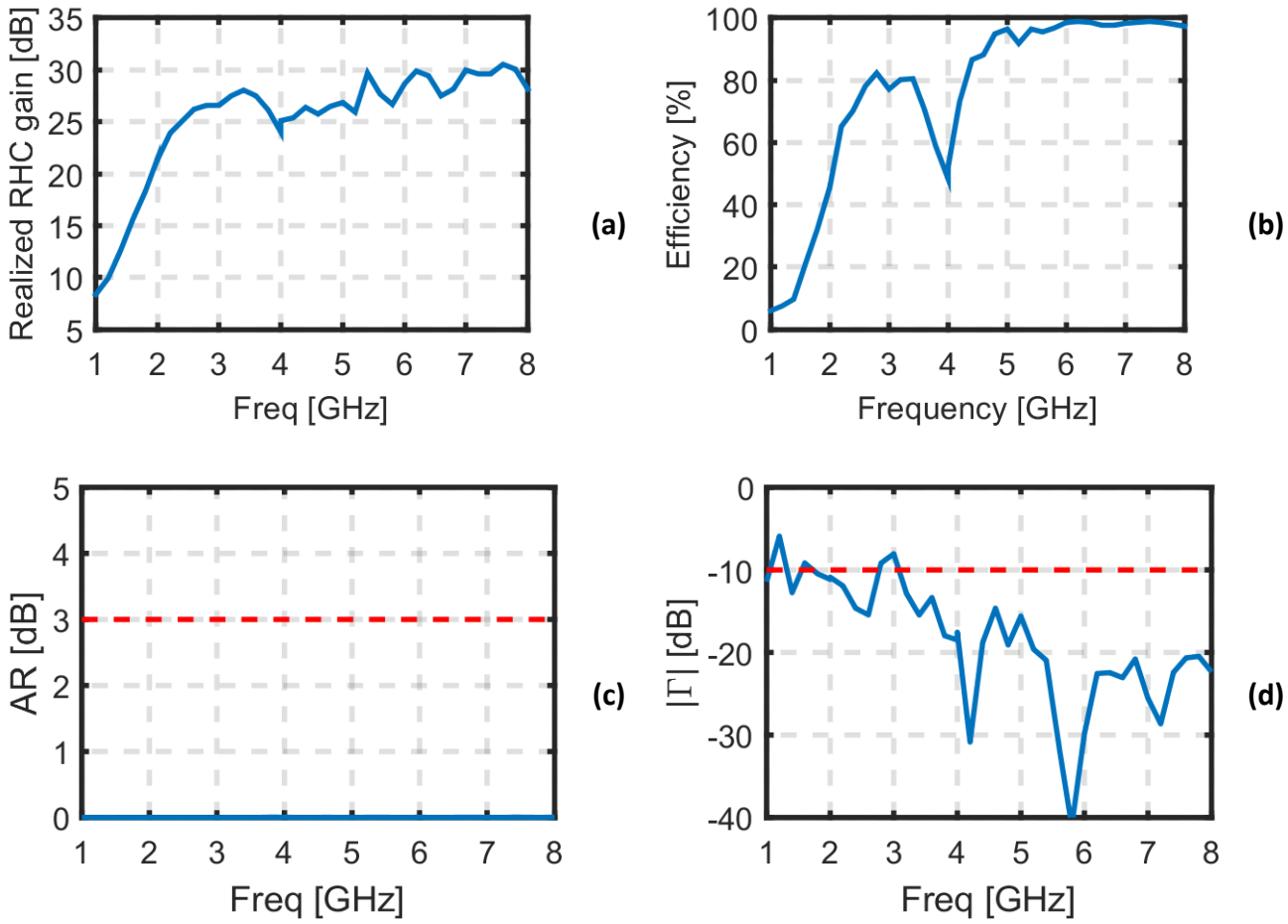

Fig. 2. 7 FEKO simulation of the concentric ring array of Fig. 2. 6 from (Hinostroza et al., 2014) with added connections between spirals at broadside ((a) Gain, (b) Efficiency, (c) AR and (d) $|\Gamma|$ typical case). The dashed red lines indicate the limit from the specifications.

We can see from Fig. 2. 7 that the gain of the antenna array is low at the lower frequencies due to the low efficiency and to the small size of the array in terms of wavelength (the array diameter is 70 cm, which is equal to 2.33 λ at 1 GHz - maximal gain is $4\pi S/\lambda^2$, which amounts to 23.3 dB at 1 GHz for the given diameter). This happens because the connections are absorbing a lot of power through their resistors. We can also observe a drop in the efficiency at 4 GHz. It is probably somehow linked to the distance between elements as $\lambda_{4\ GHz} = 7.5\ cm \sim d_{elem}$, where d_{elem} is the distance between elements of the same polarization in a ring.

In Fig. 2. 8 we see the radiating pattern of the array at 3.6 GHz, 4 GHz and 4.4 GHz. At 4 GHz we can see the mainbeam is slightly mixed with the first sidelobe, which does not happen at the neighboring frequencies (where there is no drop in the efficiency).

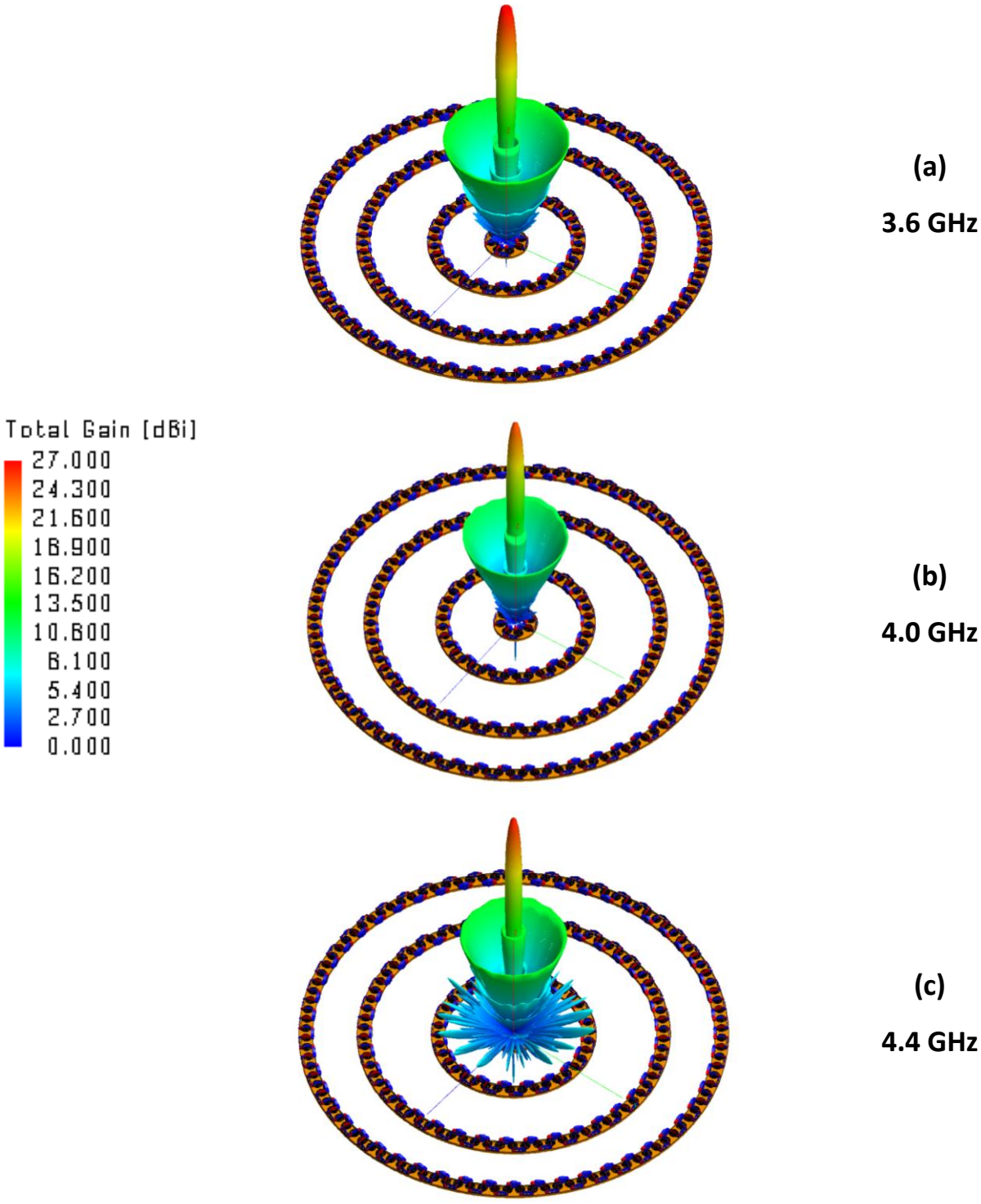

Fig. 2. 8 Radiating Pattern from the FEKO simulation of the concentric ring array of Fig. 2. 6 from (Hinostroza et al., 2014) with added connections between spirals at broadside. In (a) we have the Radiating Pattern at 3.6 GHz, in (b) at 4 GHz and in (c) at 4.4 GHz.

The AR is below the maximum specification through the whole bandwidth and, apart from one spike at 1.2 GHz, the reflection coefficient also meets the requirements over the bandwidth.

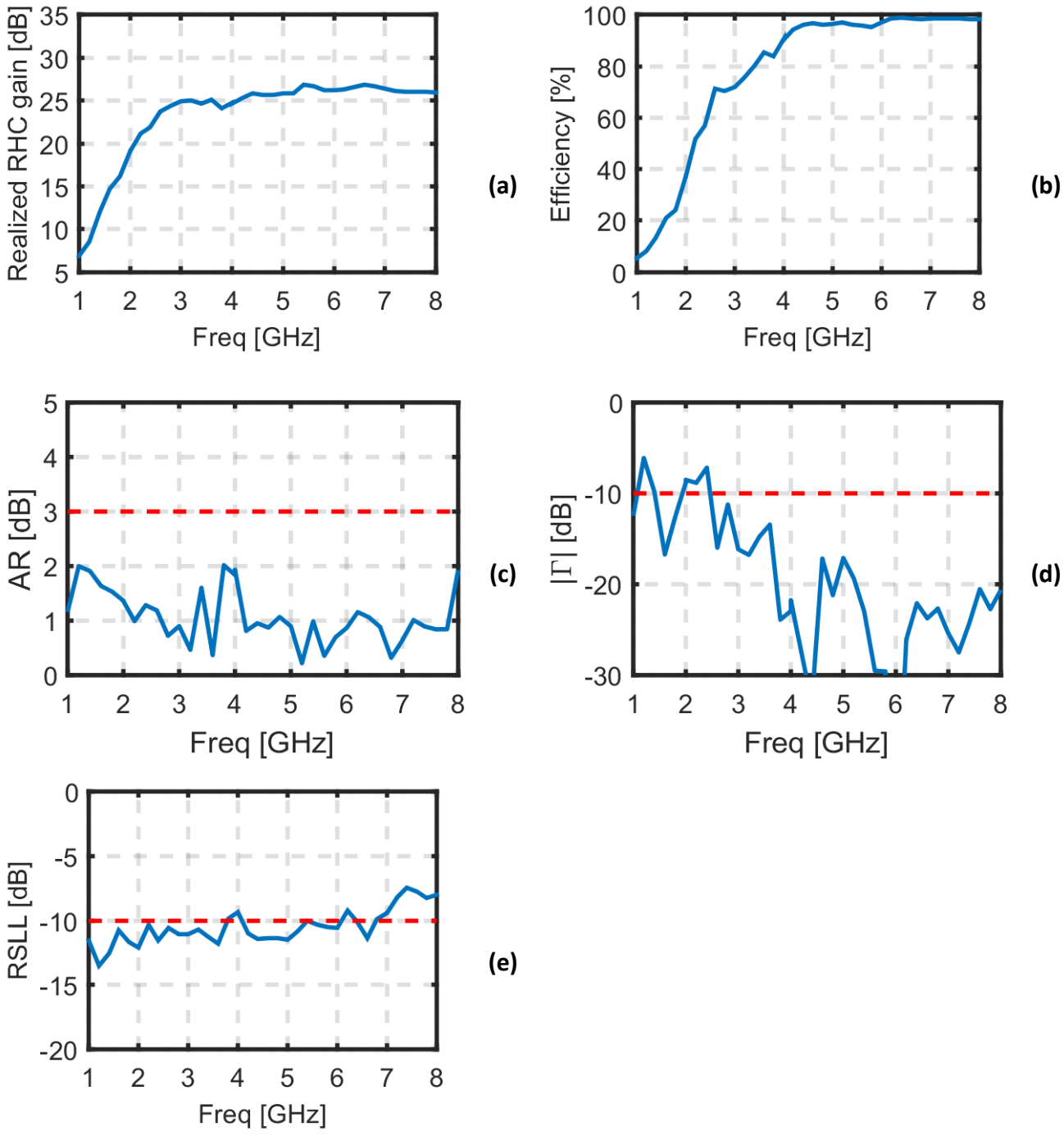

Fig. 2. 9 FEKO simulation of the concentric ring array of Fig. 2. 6 from (Hinostroza et al., 2014) with added connections between spirals steered to 30° ((a) Gain, (b) Efficiency, (c) AR, (d) $|\Gamma|$ typical case and (e) RSLL). The dashed red lines indicate the limit from the specifications.

Steering the beam to 30° eliminates the drop in efficiency that occurred at 4 GHz, as seem in Fig. 2. 9. The scanning loss oscillates between 1.4 dB and 4 dB over the bandwidth (except for the frequencies around 4 GHz).

In fig we show the radiating pattern of the array at 4 GHz and at 4.4 GHz. We can observe that the first sidelobes are deformed at 4 GHz.

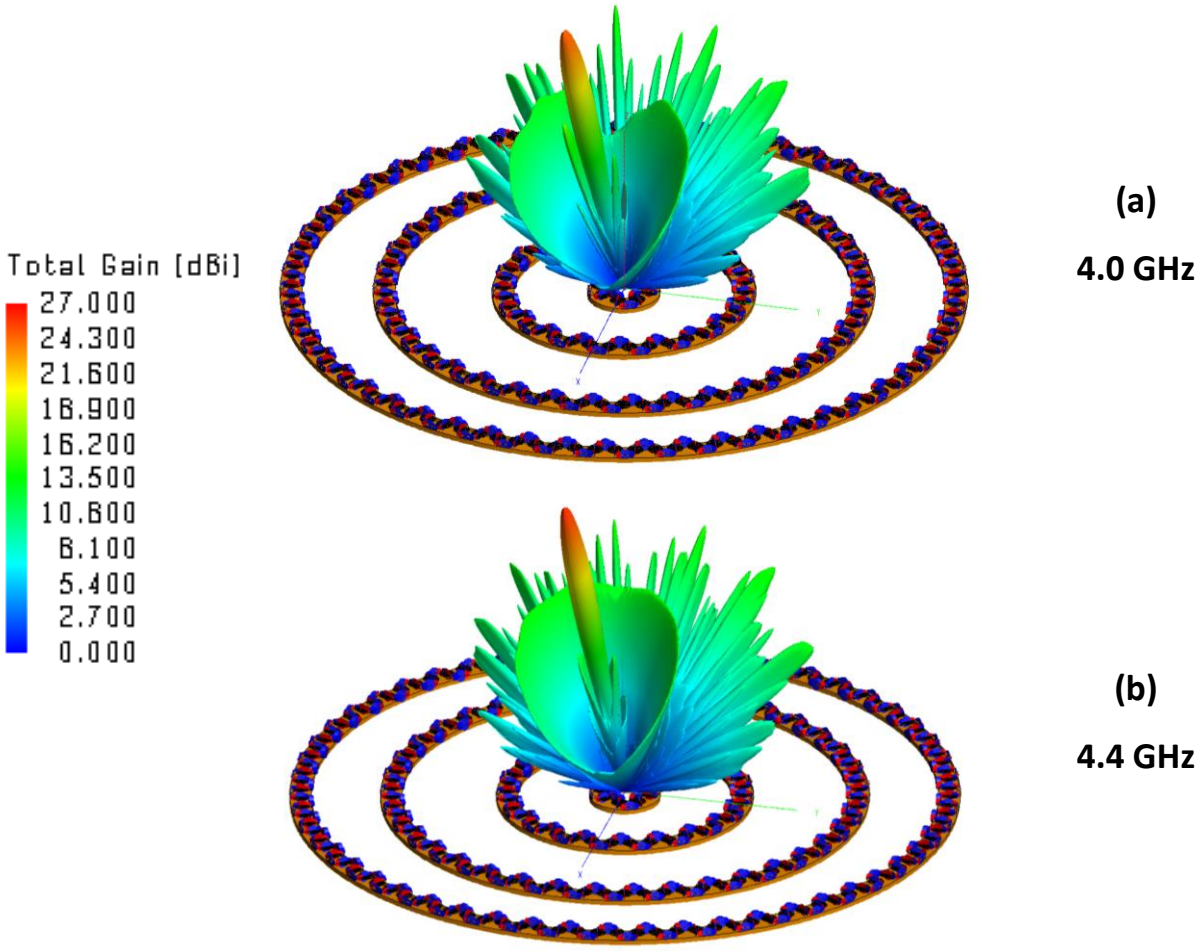

Fig. 2. 10 Radiating Pattern from the FEKO simulation of the concentric ring array of Fig. 2. 6 from (Hinostroza et al., 2014) with added connections between spirals steered to 30°. In (a) we have the Radiating Pattern at 4 GHz and in (b) at 4.4 GHz.

The AR still meets the requirements, as well as the reflection coefficient. The RSLL meets the requirements up to 6.9 GHz. Thus, the array band of operations goes from 1-6.9 GHz.

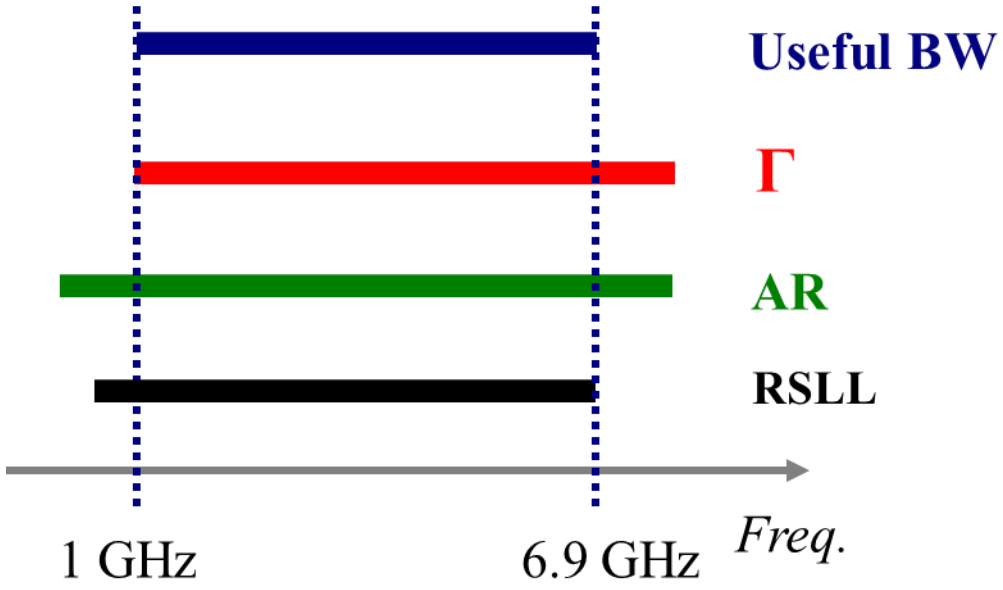

Fig. 2. 11 The bars correspond to the bandwidth definitions listed. In red we have the bar corresponding to the reflection coefficient, in green the axial ratio and in black the relative sidelobe level. The overall useful bandwidth is the intersection of these three bandwidths.

2.3. Compact Concentric Ring Array (CRA)

The array analyzed in the last section has a diameter of 1.28 meters as shown in Fig. 2. 6. Observing Fig. 2. 6 we can note that the array has a lot of space that is not occupied. In this section we will revisit the design of the array and devise an optimization that gives us an array with the same bandwidth while occupying a much smaller area.

2.3.1. First Approach - Size Constraint

In order to obtain a more compact array we started by re-optimizing the topology using Genetic Algorithms in a similar way as (*Hinostroza et al., 2014*), but adding a size constraint for the resulting array in the optimization. We will now give more detail on the array's geometry, the constraints used, the cost function and the optimization procedure. Then, we will analyze the results of the optimization.

2.3.1.1. Geometry

The maximal radius of the cavity is set by the requirements to be smaller than 35 cm. The maximal array radius for the rings is limited by $R_{max} = 33\ cm$, which accounts for the cavity size (Fig. 2. 12).

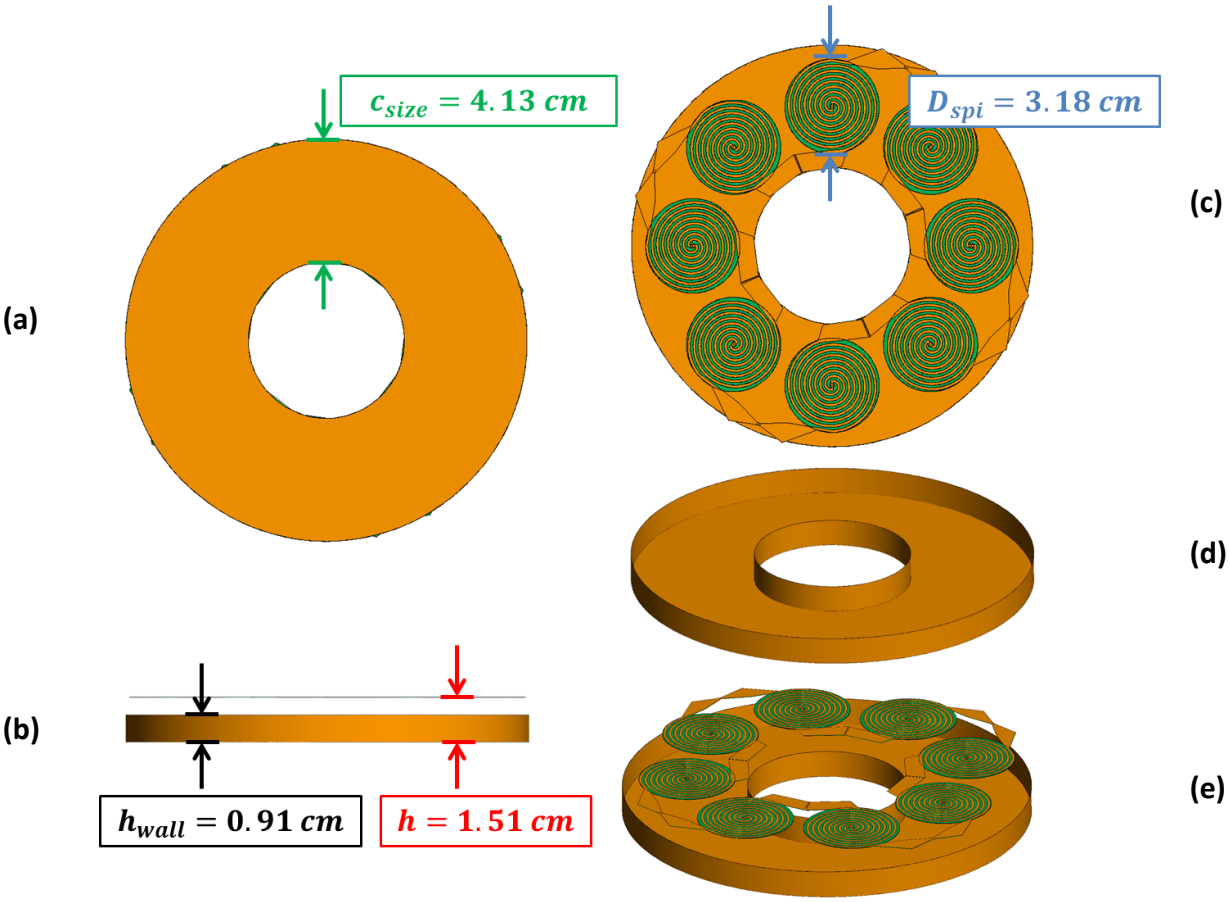

Fig. 2. 12 FEKO model of the cavity behind the ring array of connected spirals: top view (a) and isometric view (d). FEKO model of a ring array of connecting spirals: side view (b), top view (c) and isometric view (e). Spiral diameter (D_{spi}) highlighted in blue, cavity size (c_{size}) in green, height of the wall of the cavity (h_{wall}) in black and distance between the spirals and the bottom of the cavity (h) in red.

Equation 2.3 give the formulas to calculate the cavity size c_{size} (highlighted in green in Fig. 2. 12), the maximal radius of the array, and limits on the values of Δ_i for the optimization.

$$\begin{aligned} c_{size} &= 1.3\, D_{spi} = 4.13 \\ R_{max} &= 35 - c_{size}\,/2 = 33 \ \text{(values in cm)} \\ \textstyle\sum_{i=0}^{N_r-1} \Delta_i &\leq R_{max} \end{aligned} \tag{2.3}$$

In order to avoid having the rings touching each other we set a minimal distance between rings d_{r-to-r}, calculated as follows:

$$d_{r-to-r} = 1.6\, D_{spi} = 5.1\ (cm) \tag{2.4}$$

As an example Fig. 2. 13 shows the element locations and the FEKO model. Table 2. 5 shows the parameters of this array.

Table 2. 5 Parameters of the example array

Δ_0	Δ_1	Δ_2	Δ_3	Φ_1	Φ_2	Φ_3	$\sum_{i=0}^{N_r-1}\Delta_i$	Π_1	Π_2	Π_3
7 cm	8 cm	10 cm	8 cm	0.2 Π_1	0.9 Π_2	0.5 Π_3	33 cm	0.52 rad	0.30 rad	0.22 rad

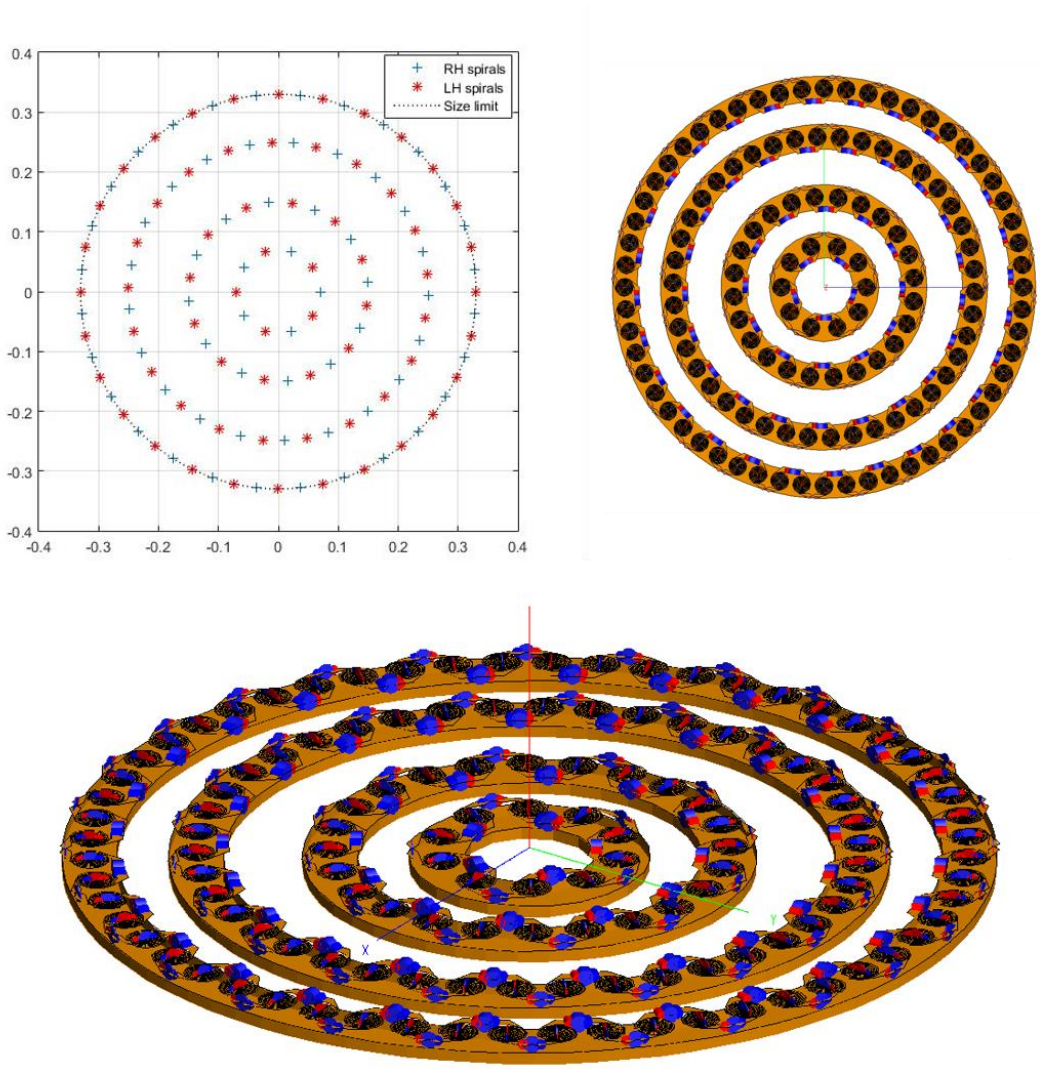

Fig. 2. 13 Elements locations of the example array (top left), Top view of the FEKO model (top right) and isometric view of the FEKO model for the example array (bottom).

2.3.1.2. Cost Function

In order to optimize the sidelobes we treat the array elements as isotropic sources (Array Factor). In order to reduce the sidelobes that are visible in the higher frequency of the desired bandwidth and the maximum steering direction, we look at the sidelobes that appear, in the Array Factor at the highest frequency, 6.9 GHz, inside of a region given by the following equation (see equation (1.11) in chapter 1):

$$u^2 + v^2 \leq (1 + \sin\theta_s)^2 \tag{2.5}$$

In order to illustrate this idea we will show in Fig. 2. 14 the Array Factor of the example array from Table 2. 5 at 6.9 GHz, normalized by its maximal value.

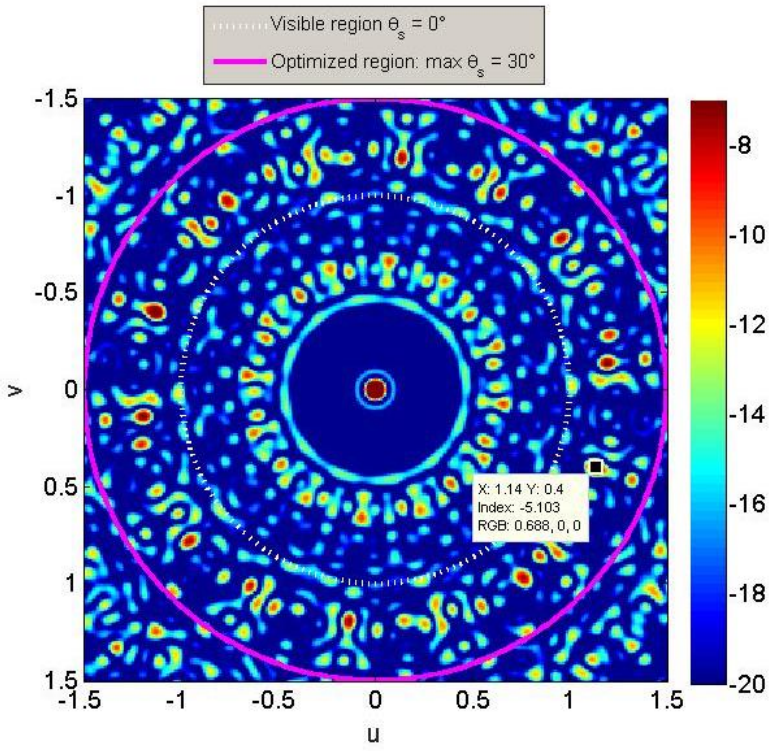

Fig. 2. 14 Array factor of the example array at 6.9 GHz. The visible region is highlighted in the white dotted line. The zone that corresponds to the union of the visible zones when steering up to $\theta_s = 30°$ and all φ_s is highlighted in purple.

Due to the symmetry of the geometry, the AF possesses central symmetry. Because of that, we can be sure that by calculating only half of the u v space, including the center of the main lobe, we will effectively obtain the AF for the whole u v space. Thus, to make the cost function faster, we search the sidelobes inside of:

$$u^2 + v^2 \leq (1 + \sin\theta_s)^2, u \geq 0 \tag{2.6}$$

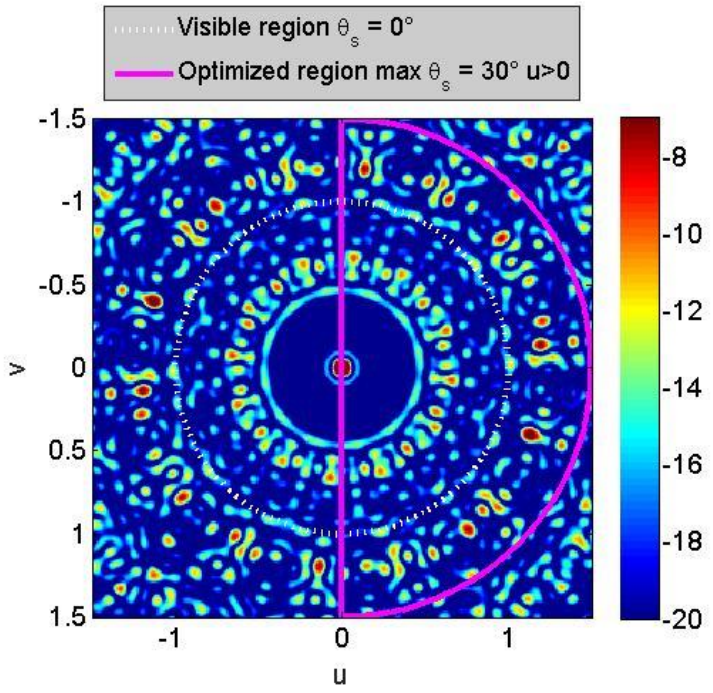

Fig. 2. 15 Array factor of the example array at 6.9 GHz. The visible region is inside the highlighted white dotted line. The zone in which we search the highest sidelobe to use in the cost function for our optimization of the concentric ring array is inside the highlighted purple line.

In order to find the maximum sidelobe level, we calculate the normalized array factor at 6.9 GHz in the region described by equation (2.6) and search for the maximal value outside of the main beam.

$$RSLL_{cost} = max_{(u,v \in u^2+v^2 \le (1+\sin\theta_0)^2, u \ge 0 \;\&\; u,v \notin mainbeam)}(20\, log_{10}|AF_{6.9GHz-norm}(u,v)|), \quad \theta_0 = 30° \tag{2.7}$$

In order to obtain a resulting array that has similar properties in the Right Handed and in the Left Handed polarization modes of operation, we calculated the AF factor for both the RH antennas and the LH antennas, find the highest sidelobe inside the region defined by equation (2.6) and calculated the cost function as follows:

$$cost = -(RSLL_{cost\,RH} \times RSLL_{cost\,LH}) \tag{2.8}$$

with $RSLL_{RH}$ and $RSLL_{LH}$ in dB.

This way, the cost function rewards solutions that have the smaller RSLL for both polarizations at the same time.

2.3.1.3. Optimization Procedure

A genetic algorithm was used to optimize Δ_i and Φ_i in order to arrive at the geometry that minimizes the cost function. We used Matlab genetic algorithm toolbox to implement the optimization.

To implement the constraint on the radius size limit during the optimization we used:

$$\sum_{i=0}^{N_r-1} \Delta_i \leq R_{max} \tag{2.9}$$

The minimal distance between rings is constrained by the parameters $\Delta_i, i = 0,1,2,3$ having a minimal value of d_{r-to-r}. As for Δ_0 we have chosen its minimal value to be the minimal radius which permits at least 3 spiral elements per polarization. This is done because we need at least 3 elements per polarization for the sequential rotation technique to work properly (*Louertani et al., 2011*).

We also choose a maximal value for those parameters to limit the search space, however the higher bound in those parameters has little influence on the optimization because of the constraint in the maximal radius already in place. In Table 2. 6 we present those limits.

Table 2. 6 Range of optimization parameters

Δ_0(cm)	Δ_1(cm)	Δ_2(cm)	Δ_3(cm)	Φ_1(rad)	Φ_2(rad)	Φ_3(rad)	$\sum_{i=0}^{N_r-1} \Delta_i$
3.5 – 13.5	$d_{r-to-r} - 3\,d_{r-to-r}$	$d_{r-to-r} - 3\,d_{r-to-r}$	$d_{r-to-r} - 3\,d_{r-to-r}$	$0 - \Pi_1$	$0 - \Pi_2$	$0 - \Pi_3$	< 33 cm

The parameters we used for the genetic algorithm were the standard values for Matlab R2015a OptimTool genetic algorithm except for the maximal number of generations, which we set to 200 as we observed the algorithm was usually stuck in a solution if it ran further than that.

In order to have a better coverage of the solution space and to avoid having the algorithm stuck to a local minimal point of the cost function, we ran the genetic algorithm 8 times in a row and only kept the best solution. We tried running it more times or with more generations but in general the results with 8 runs and a maximal number of generations of 200 are sufficient as the results do not get much better with more runs or generations.

2.3.1.4. Results

By applying the optimization procedure to the geometry described, we got the following set of optimal values:

Table 2. 7 Compact CRA optimal values

Δ_0(cm)	Δ_1(cm)	Δ_2(cm)	Δ_3(cm)	Φ_1(rad)	Φ_2(rad)	Φ_3(rad)	$\sum_{i=0}^{N_r-1} \Delta_i$
12.82	5.96	5.28	5.44	0.24 Π_1 = 0.10	0.33 Π_2 = 0.10	0.25 Π_3 = 0.06	29.5 < 33 cm

Fig. 2. 16 shows the array factor of the optimized array. The cost function value at this point is of -110.

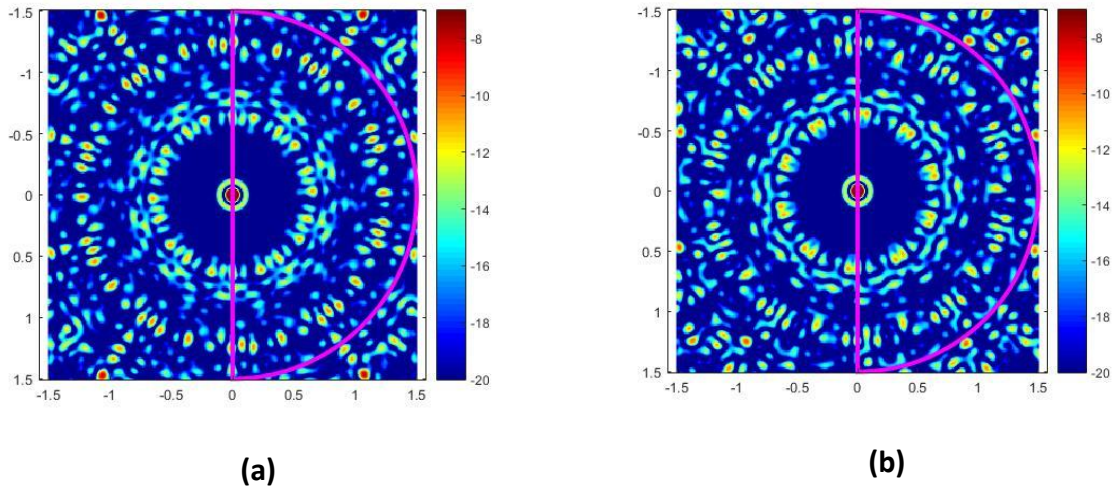

Fig. 2. 16 Array factor of the optimized compact concentric ring array at 6.9 GHz, in (a) from the RH polarized elements and in (b) from the LH polarized ones. In purple we highlight the zone in which we searched for the highest sidelobe for our optimization.

We can see that the peak sidelobes inside the optimized zone are around -10.5 dB. The example array, that had its parameters chosen arbitrarily without any prior knowledge, had its peak sidelobe around -5 dB (Fig. 2. 14), so the optimization reduced those sidelobes.

2.3.1.5. Array Analysis

Having optimized the array geometry with isotropic sources, the next step is to observe how the array behaves with the element pattern included.

Element Pattern

As a first approximation we will use the following function (*Caswell, 2001*) to approximate the radiating pattern of a spiral:

$$g(\theta,\varphi) = cos^{q}\theta, \qquad q = 1.1724 \tag{2.10}$$

Using FEKO, we simulated a one ring array with 14 elements per polarization and a radius of 16.95 cm, only feeding one of the spirals while loading the other ports with 220 ohm resistances, from 1 to 9 GHz with a step of 1 GHz. The parameter q from equation (2.10) was found by a best fit to the simulations of the element pattern of this simulation.

Then, the simulated data was transformed from the θ,φ space to the u,v space and interpolated to fit a uniform grid in the u,v space (Fig. 2. 17).

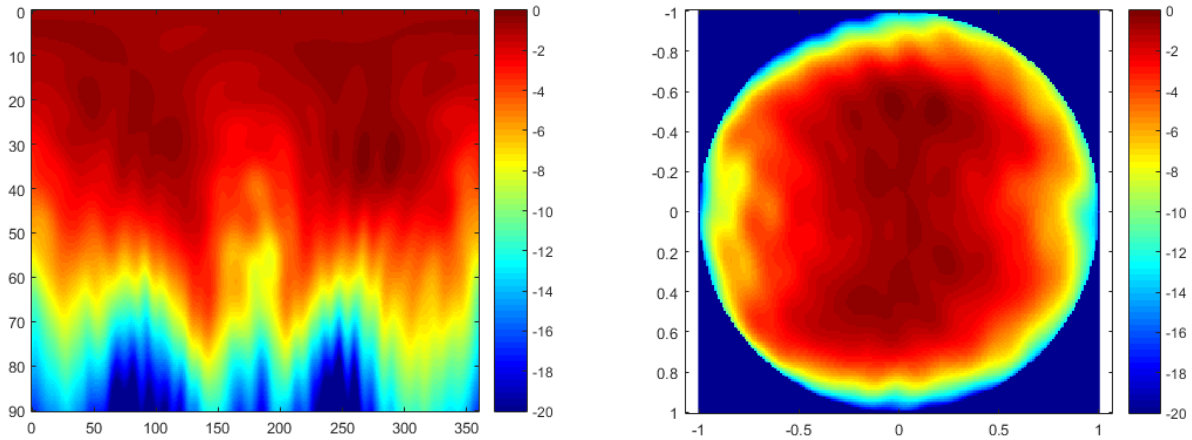

(a) **(b)**

Fig. 2. 17 Element pattern from FEKO simulation of a one ring array of connected spirals (see Fig. 2. 13 for an array with 4 rings) with 14 elements per polarization and a radius of 16.95 cm with one of the spirals on while matching the other spirals to 220 ohm resistances. The element pattern is shown at 5GHz ((a) theta phi space and (b) uv space).

The Matlab function fit tool box, with non-linear least squares, was used to find the parameter q that fits the equation (2.10) to the simulated data. As the cosine representation gives sharp

nulls when theta approaches 90° the algorithm only fitted the equation to the simulated data for theta smaller than 70°.

$$g(u,v) = cos^q\left(\sqrt{\sin^{-1}(u^2+v^2)}\right), u^2+v^2 < 0.94^2\ (\theta < 70°) \qquad (2.11)$$

By fitting the data to the equation for different frequencies we got the following results for q:

Table 2. 8 Fitted values of q

1 GHz	2 GHz	3 GHz	4 GHz	5 GHz	6 GHz	7 GHz	8 GHz	9 GHz
1.005	1.2182	1.3591	1.0636	0.9933	1.3271	1.4954	1.0861	1.0038

For our approximation we took the mean value, which results in $q = 1.1724$. In Fig. 2. 18 the element pattern from the equation (2.10) and in Fig. 2. 19 gives the element pattern from the simulation at different frequencies.

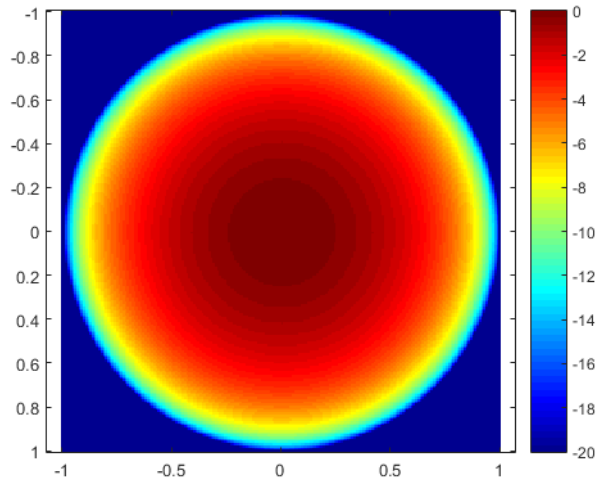

Fig. 2. 18 Element pattern from equation (2.10) in the u v space.

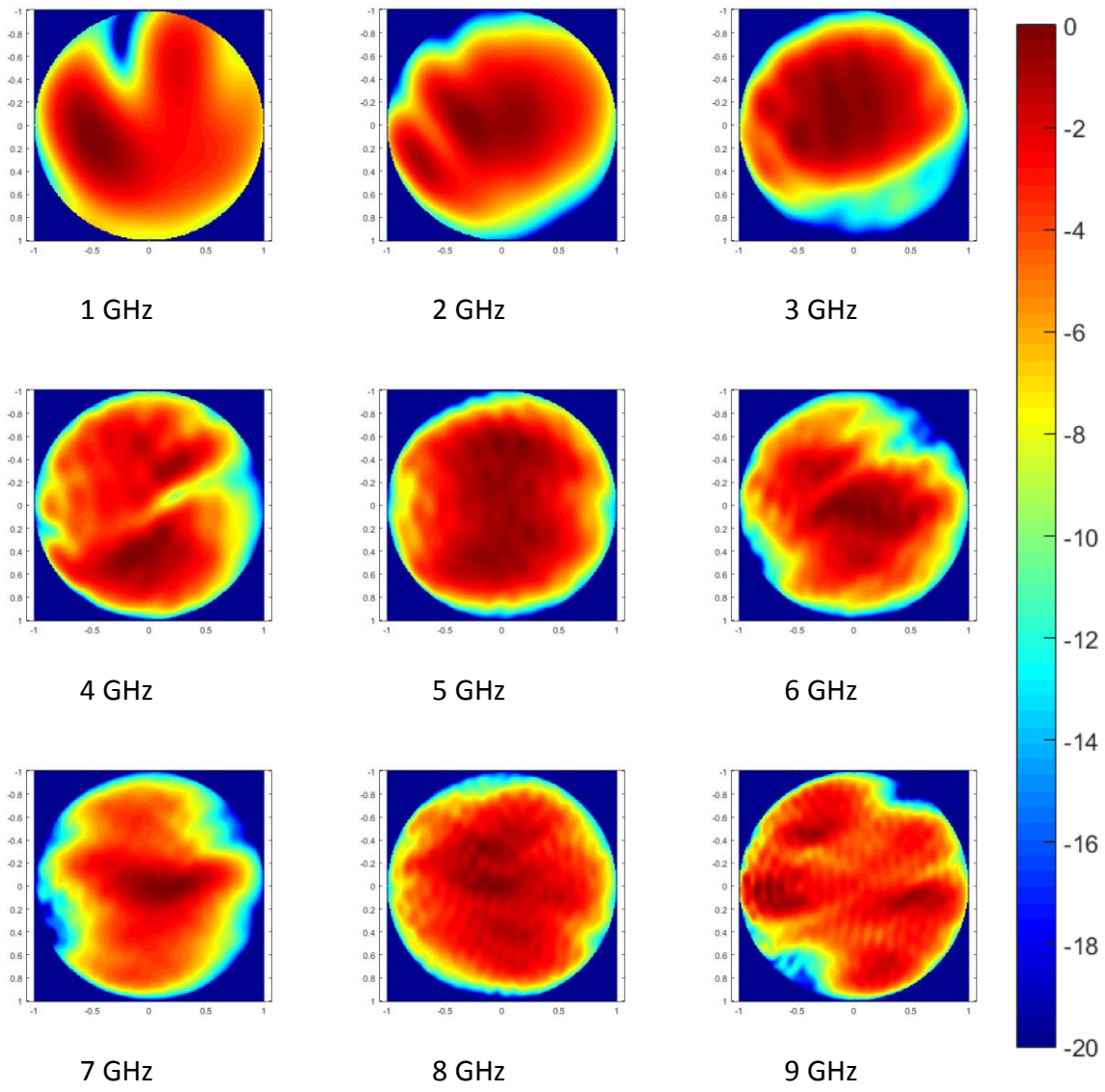

Fig. 2. 19 Element pattern from FEKO simulation of a one ring array of connecting spirals with a radius on 16.95 cm and 14 elements per polarization, with only one element connected to a feeding source and the other adapted by matching resistances, from 1 to 9 GHz in the u v space.

RSLL

By using this element pattern, we proceeded to evaluate the RSLL of the array of Table 2. 7 while steering. First we calculated the Array Pattern $F(f,\theta,\varphi,\theta_s,\varphi_s)$ by multiplying the element pattern $g(\theta,\varphi)$ and the steered array factor $f(\theta,\varphi,\theta_s,\varphi_s)$.

$$F(f,\theta,\varphi,\theta_s,\varphi_s) = g(\theta,\varphi)\, f(\theta,\varphi,\theta_s,\varphi_s) \tag{2.12}$$

Then, for each frequency, we searched for the largest sidelobe that appears in the Array Pattern for every steering where $\theta_s < 30°$.

$$RSLL(f) = max_{\theta_s,\varphi_s}\{max_{[\theta,\varphi]\notin MainLobe}[F(f,\theta,\varphi,\theta_s,\varphi_s)]\},$$
$$0° \leq \theta_s \leq \theta_0 = 30° \;\&\; 0° \leq \varphi_s \leq 360° \tag{2.13}$$

Using this method we can estimate the RSLL as a function of frequency for the optimized array (Fig. 2. 20).

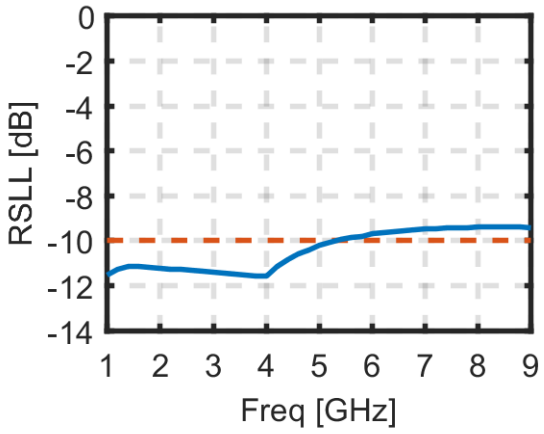

Fig. 2. 20 RSLL vs freq. for the compact concentric ring array 1st optimization using a $\cos^q$ approximation for the element pattern. The dotted red line is the limit from the specifications.

We can observe that the high end of the bandwidth is limited to 5.2 GHz with this approach. We managed to reduce the size of the new array compared to the previous array, from (*Hinostroza, 2013*), but the bandwidth of the new array is smaller (1-5.2 GHz), even if our optimization took the whole bandwidth of the previous array (1-6.9 GHz) into account.

2.3.2. A step further in optimization: using Array Pattern analysis

As we have seen, by optimizing the sidelobe level in a canonical way, the resulting array has a reduced bandwidth. In order to obtain a larger bandwidth we will examine the array patterns steered to $[\theta_s\,, \varphi_s] = [30°, 0°]$ (calculated using equation (2.10)) at several frequencies (Fig. 2. 21) to devise a better optimization.

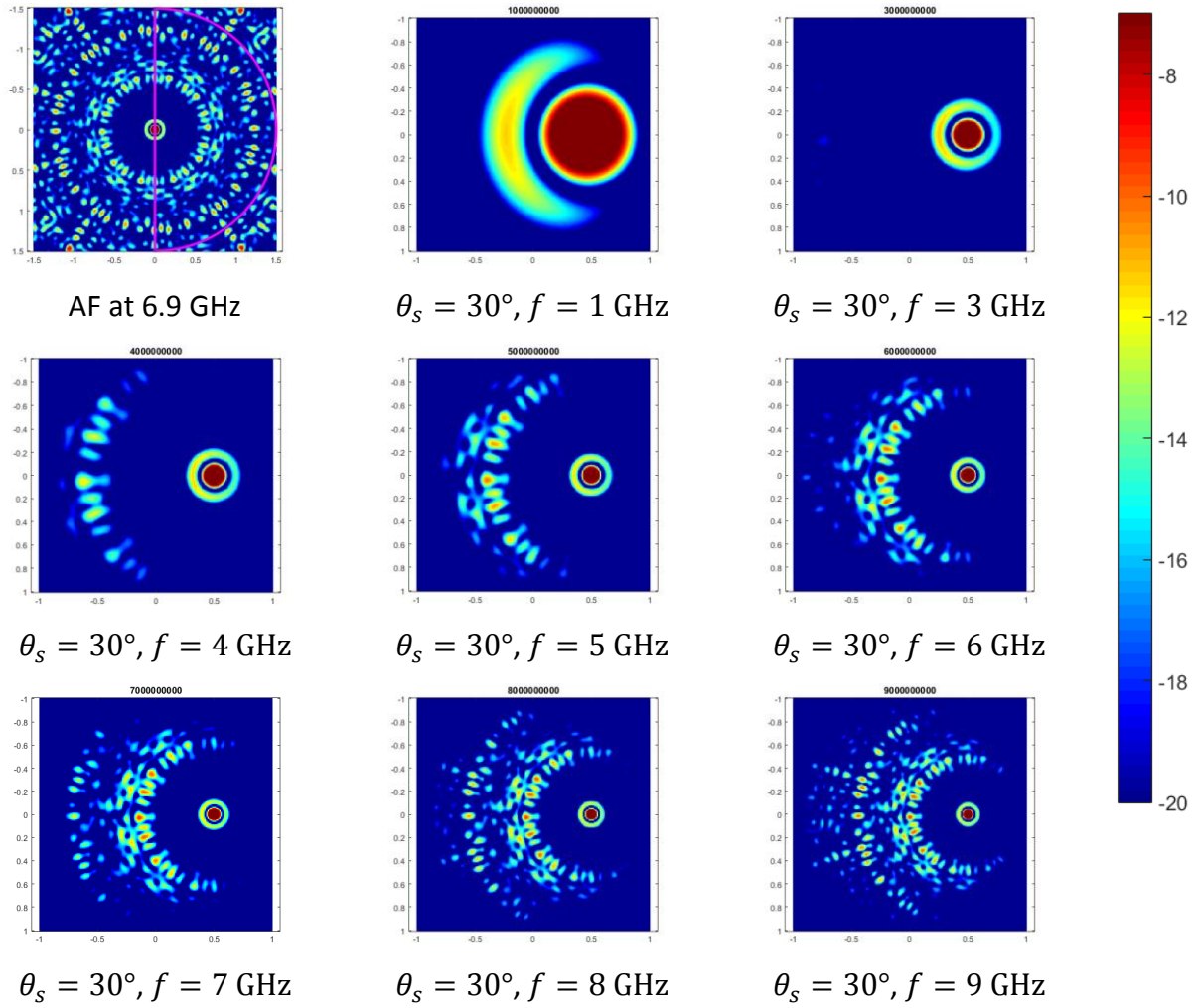

Fig. 2. 21 Array Factor of the optimized array from Table 2. 7 at 6.9 GHz (Top Left). On the other figure we have the radiating pattern of the same array steered to 30° at several frequencies (from 1 to 9 GHz) using the equations (2.10) and (2.12).

Fig. 2. 21 shows the different zones of the AF that are more important at the different frequency ranges. As the frequency increases, the circles of sidelobes shrinks and get closer to the main beam. At the lower frequencies (1-3 GHz) the sidelobe level is dictated by the ring around the main beam.

Up to the mid frequencies, the 1st circle of high sidelobes is prevalent. At higher frequencies the 2nd circle of high sidelobes starts to appear and have a larger influence in the sidelobe level.

Those high sidelobe circles correspond to the sum of the grating lobe regions of the rings in the CRA (see Fig. 1. 6), which all appear around the same region as the distance between elements is approximatively the same for all rings in the array. We will refer to those circles as grating lobe rings.

One thing that is interesting to note is that, at 7 GHz (Fig. 2. 22), although the 2nd ring of grating lobes is in the visible region, its level is a lot lower than what we see in the AF. On the other hand, the 1st ring of grating lobes is larger than what we see in the AF.

This happens because, at that 7 GHz and steering to $\theta_s = 30°$, the mainbeam of the array factor passes at the border of the element pattern (at $[u, v] = [0.5, 0]$) and gets attenuated while the 1st ring of grating lobes passes at the center of the element pattern (at $[u, v] = [0, 0]$) and is not affected. Relative to the mainbeam, the 1st ring of grating lobes is being boosted.

The 2nd ring of grating lobes passes outside of the main beam of the element pattern (at $[u, v] = [0.7, 0]$) and so it is more attenuated by the element pattern than the mainbeam of the array factor, so relative to the mainbeam it is being attenuated .

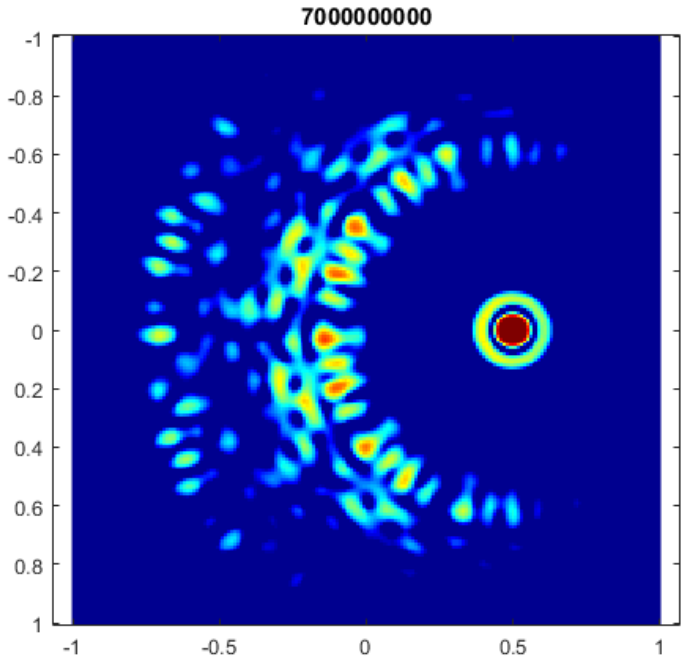

$\theta_s = 30°, f = 7$ GHz

Fig. 2. 22 Radiating pattern of the optimized array from Table 2. 7, steered to 30°, at 7GHz,calculated using the equations (2.10) and (2.12).

In order to compensate for that effect it should be sufficient to find an array with a lower level on the first ring of grating lobes. As the second ring of grating lobes is attenuated by the

element pattern relative to the main beam at the frequency range of interest we can limit the optimized region in the Array Factor to only include the 1st ring of grating lobes.

2.3.2.1. Cost Function

In order to implement the optimization of the array considering the grating lobe regions in the AF it is no longer reasonable to look at a specific frequency to decide the region to be optimized. It makes more sense to normalize the array factor by the frequency and the distance between elements (as one would in a uniform array to identify the grating lobes, as well as it has been done in Fig. 1. 5 and Fig. 1. 6).

As we want to optimize the sidelobes that appear up to the second grating lobe ring, without including it, the optimized zone becomes:

$$\left(\frac{u\ d_{elem}}{\lambda}\right)^2 + \left(\frac{v\ d_{elem}}{\lambda}\right)^2 \leq 1.85^2, u \geq 0 \tag{2.14}$$

To have a comparison with the previous optimization this zone corresponds, at 6.9 GHz, to:

$$u^2 + v^2 \leq 1.15^2, u \geq 0 \tag{2.15}$$

So to calculate the sidelobe level we calculate the normalized array factor in the region described by equation (2.14) and search for the maximal value outside of the main beam, as is done in equation (2.16):

$$RSLL_{cost2} = max_{\left(u,v \in \left(\frac{u\ d_{elem}}{\lambda}\right)^2 + \left(\frac{v\ d_{elem}}{\lambda}\right)^2 \leq 1.85^2, u \geq 0\ \&\ u,v \notin mainbeam\right)} \left(20\ log_{10}|AF_{norm}(u,v)|\right) \tag{2.16}$$

As before, the cost function includes the RSLL of both polarizations (RH and LH), as in equation (2.8) in order to reward solutions where the RSLL is equally low at both polarizations.

We proceeded to optimize the array with this cost function using the same procedure described in section 2.3.1.3.

2.3.2.2. Results

By optimizing the array using the new cost function, we obtained the parameters in Table 2. 9. The cost function of the optimized array has a value of -131.85. In Fig. 2. 23 we show the AF of the optimized array calculated at 6.9 GHz.

Table 2. 9 Compact CRA optimal values using the RSLL search zone of (2.14) for the cost function

Δ_0(cm)	Δ_1(cm)	Δ_2(cm)	Δ_3(cm)	Φ_1(rad)	Φ_2(rad)	Φ_3(rad)	$\sum_{i=0}^{N_r-1}\Delta_i$
12.9	5.85	5.37	5.24	077. Π_1 = 0.32	0.24 Π_2 = 0.07	0.62 Π_3 = 0.16	29.4 < 33 cm

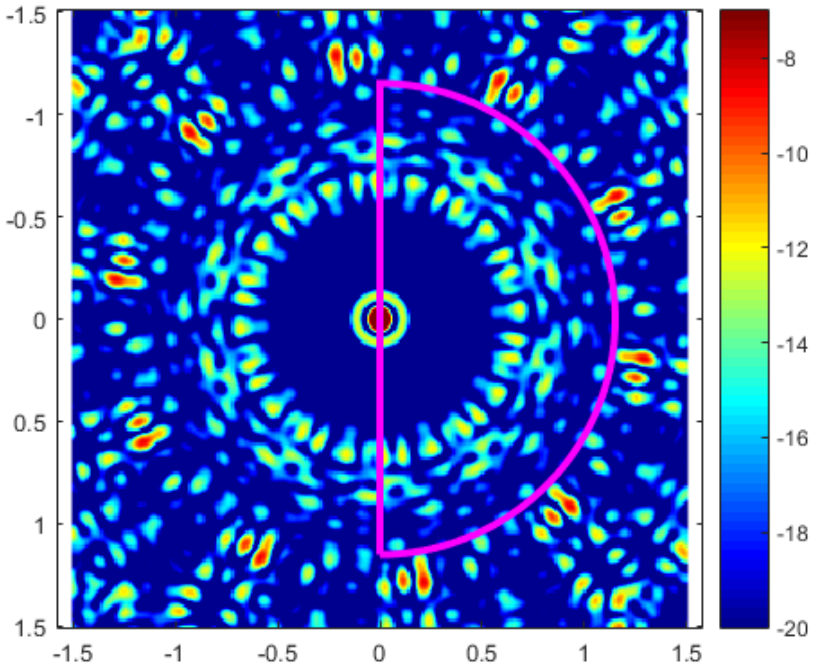

Fig. 2. 23 Array factor of the optimized compact concentric ring array using a smaller RSLL search zone for the cost function, at 6.9 GHz. In purple we highlight the zone in which we searched for the highest sidelobe for our optimization.

Fig. 2. 23 shows that the optimization succeeded in reducing the first ring of grating lobes, having their values leveled around -11.7 dB, 1.2 dB lower than in the first optimization (that had all sidelobes leveled around -10.5 dB).

As expected, by restricting the optimized zone the optimization converges to lower sidelobes in the first ring of grating lobes while allowing for larger sidelobes in the second ring of grating lobes.

The second ring of grating lobes is higher than in the previous optimization, but the values are still leveled, with values around -8.5 dB. This is a nice property to have if we want the array to have similar properties for all directions as, even though they are attenuated, the second ring of grating lobes still appears in the visible zone for the arrays frequency and steering range of operation.

2.3.2.3. Array Analysis

Fig. 2. 24 is a plot of the RSLL vs frequency for the optimized array, calculated using equations (2.10) and (2.13) (as with the previous array).

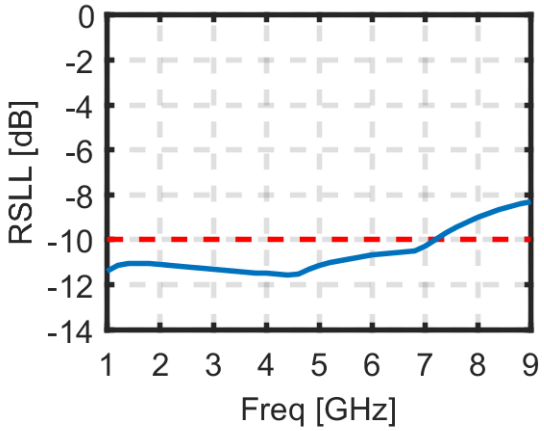

Fig. 2. 24 RSLL vs freq. for the compact concentric ring array 2nd optimization using a $\cos^q$ approximation for the element pattern. The dotted red line is the limit from the specifications.

We can see that the new optimization strategy was successful in widening the bandwidth of the array. With the new optimization, the array respects the RSLL requirements up to 7.2 GHz.

2.3.2.4. Array analysis using FEKO

The arrays have been analyzed using an approximate expression up to this point. As we have found a design that satisfied the imposed constraints we move on to validate its performance with a FEKO simulation (Fig. 2. 25).

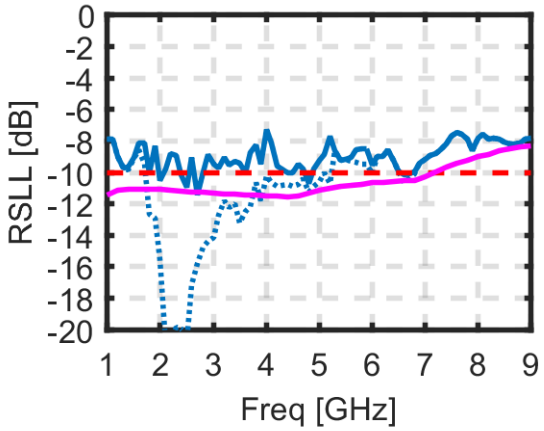

Fig. 2. 25 RSLL vs freq. for the compact concentric ring array 2nd optimization. The purple curve is the RSLL calculated using a $\cos^q$ approximation for the element pattern. The blue curve is the RSLL obtained from a FEKO simulation of the array. The dotted blue curve is the RSLL from the same FEKO simulation but disregarding the sidelobe closest to the main beam (Fig. 2. 26) The dashed red line is the limit from the specifications.

As we can see, the sidelobe level is higher than what was found in the approximate model (Fig. 2. 24). Looking at the electric fields (Fig. 2. 26) we noticed that the first lobes were higher than what we expected.

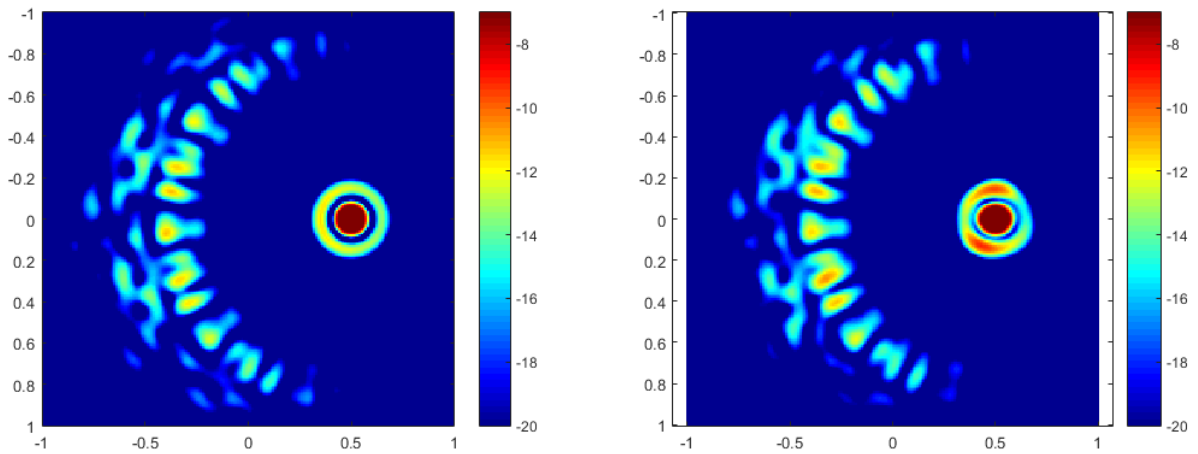

Fig. 2. 26 Electric field radiated from the concentric ring array from Table 2. 9 at 5 GHz, steered to 30°, in the u v space. In (a) we have the electric field obtained with equations (2.10) and (2.12) and in (b) the electric field obtained from a FEKO simulation.

Indeed, if we exclude the first lobe from our RSLL calculations, the resulting RSLL vs frequency curve gets a lot closer to the one predicted from the simplified model (Fig. 2. 25)

This first lobe relates, in the AF, to the ring lobe around the main beam. It would seem from Fig. 2. 26 that, if we are able to further reduce this ring lobe we would obtain an array with the desired bandwidth (1-6.9 GHz).

2.3.3. Optimization with weighting of 1st lobe

The approach we will use to effectively reduce the first ring lobe, while keeping the first ring of grating lobes small, will be based on adding a multiplicative weighting factor γ to the first ring lobe in the cost function, thus prioritizing its reduction during the optimization.

The value γ was chosen to be $\sqrt{2}$. The value of the first lobe in the solutions of the previous optimizations had a similar value compared to the larger lobes in the grating lobe regions, so by adding this weighting we can force the value of the first lobe to be at least 3 dB ($20\ log_{10}\sqrt{2}$) below the larger sidelobes. Hopefully we can find a solution with a similar level in the grating lobe region while respecting this new constraint.

In order to find the region occupied by the first ring in the u-v space we simply looked at one of the realizations of the array (given the geometric constraints) and went from the circle just after the main beam to a circle after the first lobe and before the grating lobes:

$$0.13^2 \leq \left(\frac{u\, d_{elem}}{\lambda}\right)^2 + \left(\frac{v\, d_{elem}}{\lambda}\right)^2 \leq 0.41^2 \tag{2.17}$$

The region occupied by the first lobe in a ring array is related to the distance between elements and the radius of the array, so there should not be that much variation in its position under the constraints imposed on the geometry. Moreover, the beamwidth of the main beam is also kept reasonably constant for the given geometry.

So, the new cost function is given by:

$$RSLL_{cost\ 3} = max_{\left(u,v \in \left(\frac{u\, d_{elem}}{\lambda}\right)^2 + \left(\frac{v\, d_{elem}}{\lambda}\right)^2 \leq 1.85^2, u \geq 0\ \&\ u,v \notin mainbeam\right)} \left(20\, log_{10}|AF_{Pond}(u,v)|\right) \tag{2.18}$$

$$AF_{Pond}(u,v) = \begin{matrix} AF_{norm}(u,v), 0.41^2 \leq \left(\frac{u\, d_{elem}}{\lambda}\right)^2 + \left(\frac{v\, d_{elem}}{\lambda}\right)^2 \leq 1.85^2 \\ \gamma\, AF_{norm}(u,v), 0.13^2 \leq \left(\frac{u\, d_{elem}}{\lambda}\right)^2 + \left(\frac{v\, d_{elem}}{\lambda}\right)^2 \leq 0.41^2, \gamma = \sqrt{2} \end{matrix} \tag{2.19}$$

$$cost = -(RSLL_{cost\ RH} \times RSLL_{cost\ LH}) \tag{2.20}$$

Using the same optimization procedure as before, the genetic algorithm produced the set of parameters on Table 2. 10. Fig. 2. 27 shows the AF of the optimized array with and without the weighting factor on the first ring lobe.

Table 2. 10 Compact CRA optimal values using a smaller RSLL search zone for the cost function, as well as weighting the first sidelobe

Δ_0(cm)	Δ_1(cm)	Δ_2(cm)	Δ_3(cm)	Φ_1(rad)	Φ_2(rad)	Φ_3(rad)	$\sum_{i=0}^{N_r-1} \Delta_i$
7.24	8.01	8.42	9.18	0.64 Π_1 = 0.31	0.52 Π_2 = 0.16	0.52 Π_3 = 0.12	32.9 < 33 cm

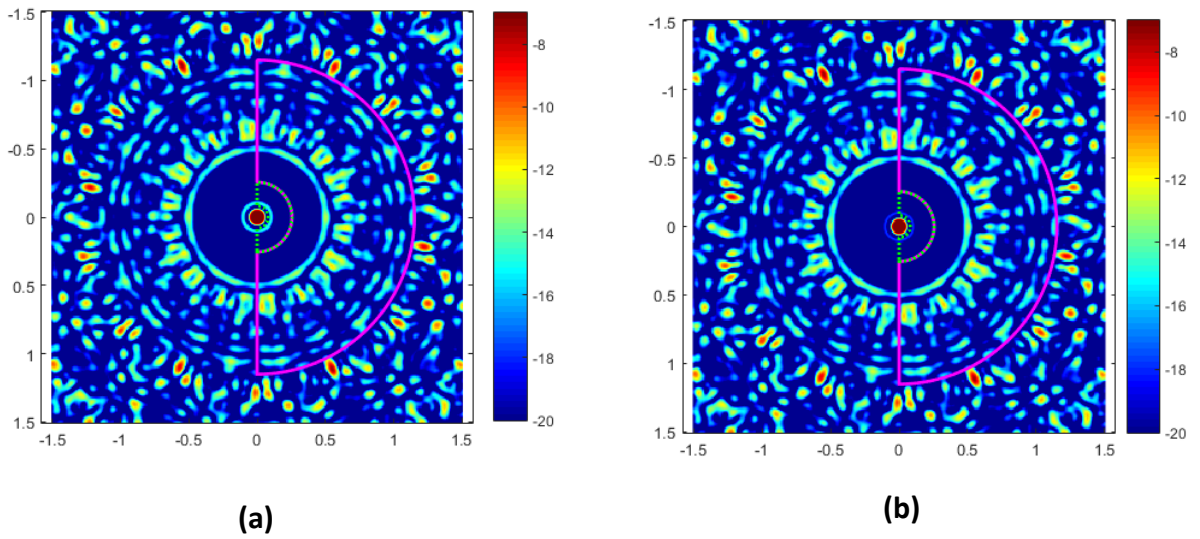

Fig. 2. 27 Array factor of the optimized compact concentric ring array using a smaller RSLL search zone for the cost function and weighting the first sidelobe by $\sqrt{2}$, at 6.9 GHz. In purple we highlight the zone in which we searched for the highest sidelobe excluding the first sidelobe and in dotted green we highlight the zone that was weighted by $\sqrt{2}$. In (a) the Array Factor of the optimal array with the weighting and in (b) without the weighting.

We can observe that the weighting factor succeeded in reducing the first ring lobe with little to no impact on the optimized value of the lobes on the first ring of grating lobes. The sidelobes in the grating lobe region were kept around -11.5 dB while the first sidelobe is at -17.8 dB.

We calculated this array's RSLL using the equations (2.10) and (2.13) as well as with a FEKO simulation (Fig. 2. 28).

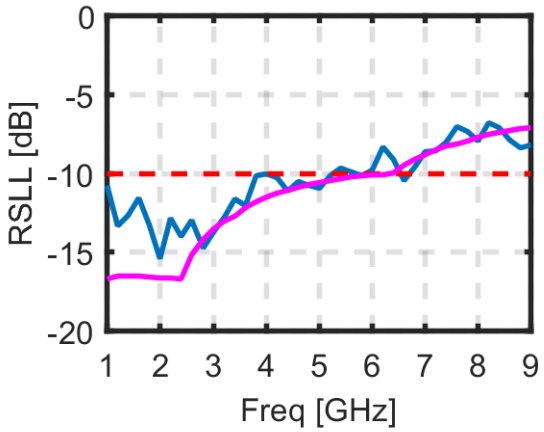

Fig. 2. 28 RSLL vs freq. for the compact concentric ring array 3rd optimization. The purple curve is the RSLL calculated using a $\cos^q$ approximation for the element pattern. The blue curve is the RSLL obtained from a FEKO simulation of the array. The dashed red line is the limit from the specifications.

We can observe that, in the mid to high frequencies, the model gives a reasonably accurate approximation of the RSLL. In the lower frequencies we can still see that the FEKO simulation wields a significantly higher RSLL, but with the new optimization procedure we were able to keep the RSLL under -10 dB.

We proceed to analyze all of the parameters of interest of the obtained array, at broadside (Fig. 2. 29) and when steering to 30° (Fig. 2. 30) , for the RHC polarization.

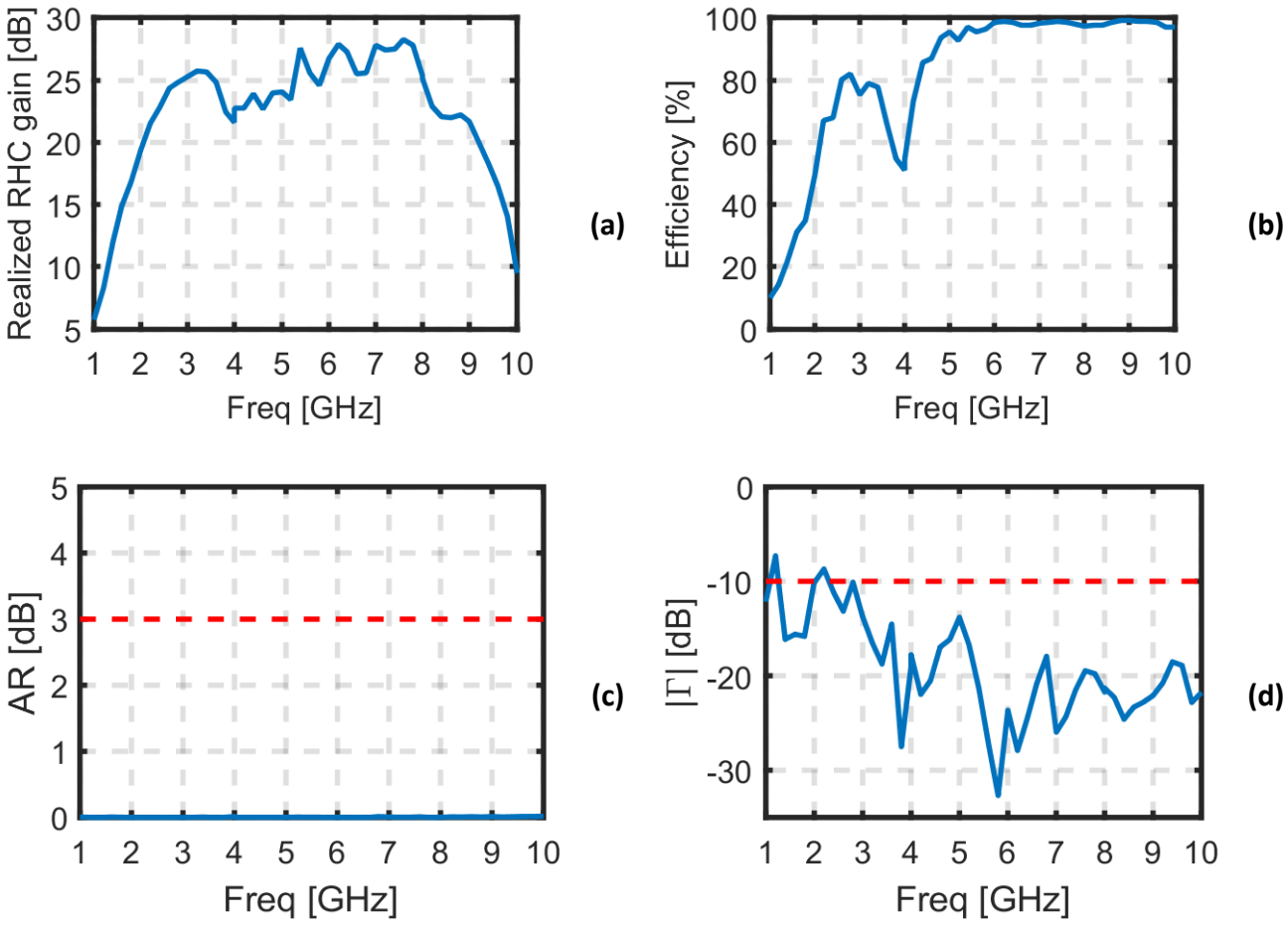

Fig. 2. 29 FEKO simulation of the concentric ring array of connecting spirals from the 3rd optimization (Table 2. 10) at broadside ((a) Gain, (b) Efficiency, (c) AR and (d) $|\Gamma|$ typical case). The dashed red lines indicate the limit from the specifications.

We can see the results from Fig. 2. 29 and Fig. 2. 7 are very similar. In Fig. 2. 29 we decided to simulate the array up to 10 GHz. We can observe a drop in gain of about 15 dB at 10 GHz, which happens because the distance between the cavity and the spiral antennas is equal to $\lambda/2$ at 10 GHz. We do not observe the same drop in gain at 10 GHz when we steer the array (Fig. 2. 30), but we can observe there is some degradation on the Axial Ratio at that frequency.

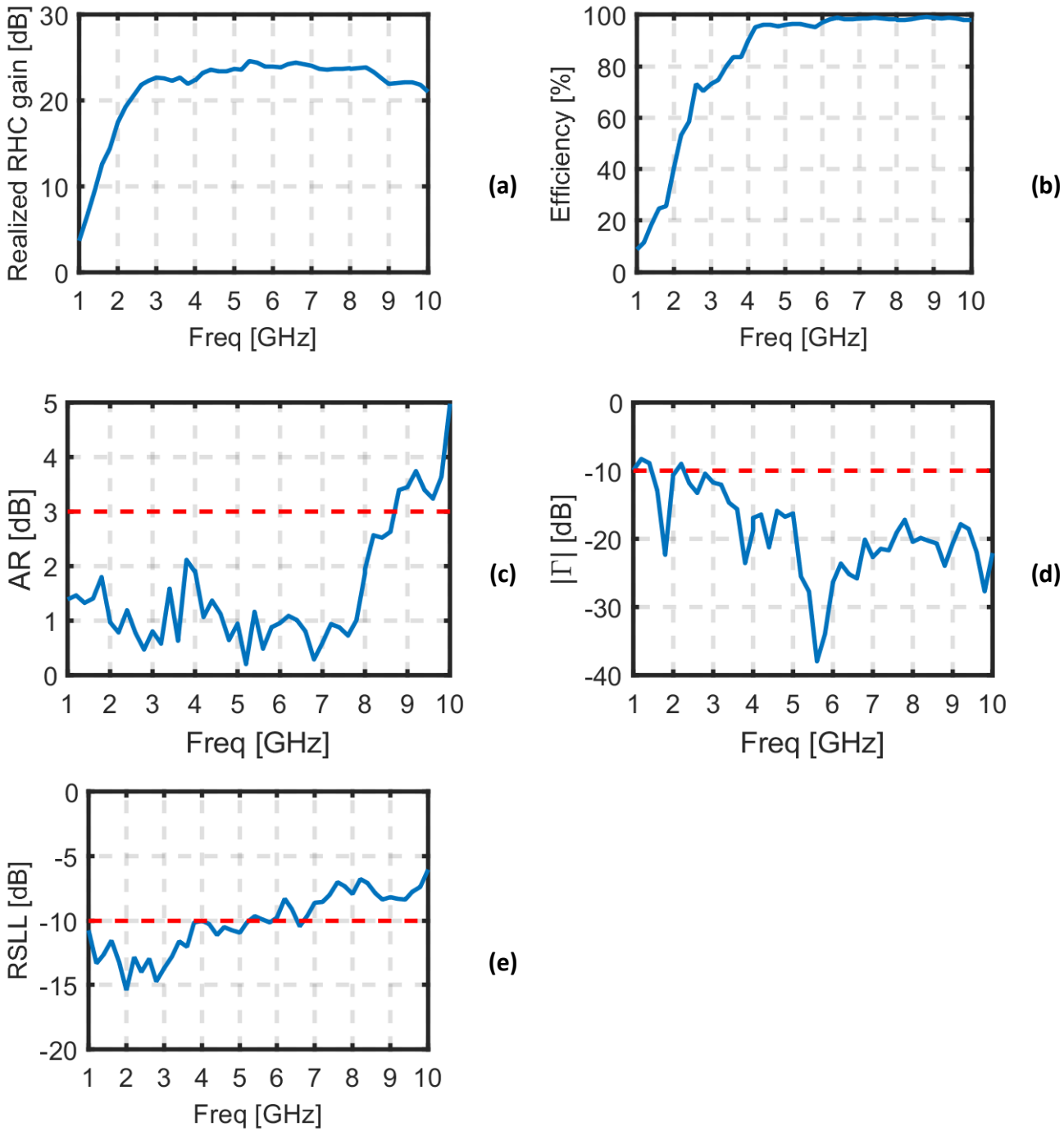

Fig. 2. 30 FEKO simulation of the concentric ring array of connecting spirals from the 3rd optimization (Table 2. 10) steered to 30° ((a) Gain, (b) Efficiency, (c) AR and (d) $|\Gamma|$ typical case and (e) RSLL). The dashed red lines indicate the limit from the specifications.

By comparing Fig. 2. 29 and Fig. 2. 30 with Fig. 2. 7 and Fig. 2. 9 we can see that we were able to find an array that has the same specifications, but occupying a much smaller area. Indeed, the

diameter of the array has been reduced from 1.28 meters to 0.70 meters, which amounts to only 29.9% of the original area (Table 2. 11).

Table 2. 11 Comparison of key parameters of the Concentric Ring Array from (Hinostroza, 2013) and the one from Table 2. 10.

	CRA (Hinostroza, 2013)	**CRA (Table 2. 10)**
N° of Antennas (half RH spirals, half LH spirals)	224	122
N° of Rings	4	4
Diameter	128 cm	70 cm
Surface	12867 cm^2	3848 cm^2

We can observe that the Relative Sidelobe Level, the Axial Ratio, the Efficiency and the Reflection Coefficient all behave in the same way for both arrays.

The Realized Right Handed Circular polarized Gain of the CRA of connecting spirals from the 3rd optimization (Table 2. 10) is smaller by about 2.5 dB compared to that from (*Hinostroza, 2013*) (Fig. 2. 7, Fig. 2. 9, Fig. 2. 29 and Fig. 2. 30), which can be explained by the smaller area occupied by radiating elements. However the final array is much less sparse, which explain why the gain did not go down as much as the area reduction ($10\ log_{10}(0.299) = -5.2$).

The designed array has a bandwidth going from 1 – 6.9 GHz while steering up to 30° with dual circular polarization and a diameter < 0.7 meter (Fig. 2. 31).

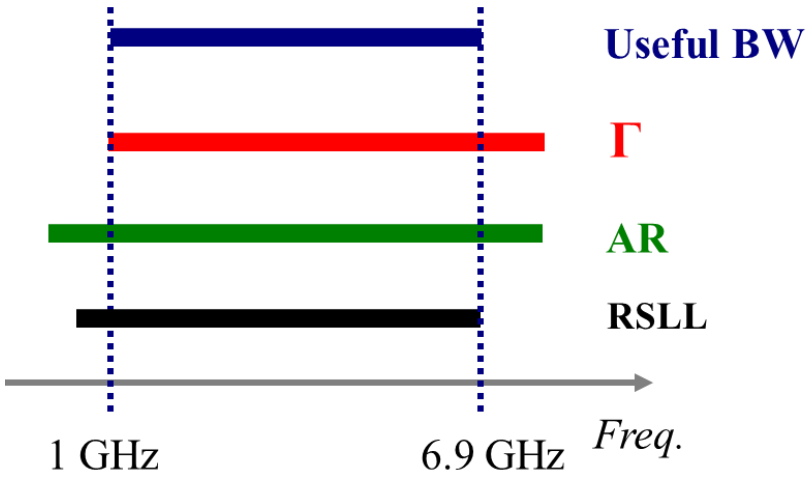

Fig. 2. 31 The bars correspond to the bandwidth definitions listed. In red we have the bar corresponding to the reflection coefficient, in green the axial ratio and in black the relative sidelobe level. The overall useful bandwidth is the intersection of these three bandwidths.

2.4. Concentric Ring Array with WAVES

With the goal of further extending the bandwidth of the array, we propose the use of the WAVES (Wideband Arrays with Variable Element Sizes) technique (*Shively and Stutzman, 1990*), which uses elements of different sizes to cover different bandwidths. We will analyze two topologies.

In one we will re-optimize the element positioning in the array in such a way that we can fit a scaled down copy of the array in its center (Fig. 2. 32). The other will be to increase the constraint on the minimal distance between rings so that we can alternate rings of different sized elements (Fig. 2. 33).

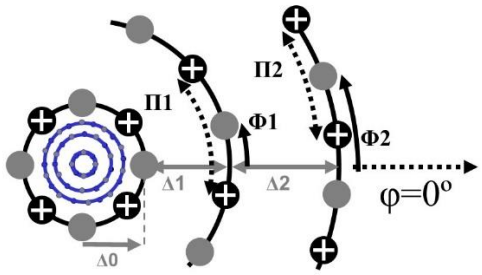

Fig. 2. 32 Scheme scaled down WAVES.

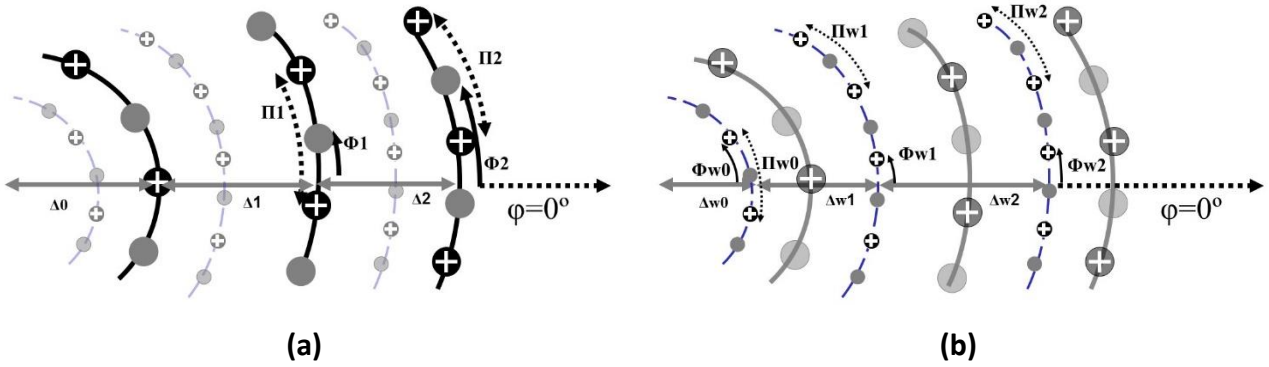

Fig. 2. 33 Scheme interleaved WAVES. Highlighted large elements (a) and small elements (b).

2.4.1. Concentric Ring Array with scaled down WAVES

In the first approach we re-optimize the Concentric Ring Array in such a way that allows us to place a size-reduced copy of the optimized array in its center (Fig. 2. 32). In this design the larger rings operate in the lower frequencies and the smaller rings operate in the higher frequencies. In the mid frequencies both the large and smaller rings can work together as the larger rings can provide a better gain and the smaller rings can help to control the sidelobe level.

2.4.1.1. Geometry

The geometry is very similar to that described in section 2.3.1.1. It consists of a concentric ring array with a scaled down copy in its center. The first question we try to answer is which scaling factor to use.

The criterion chosen was for the scaled down elements to be as big as possible. It is interesting to have some overlapping between the bandwidths of the large and small elements in the array, so that the large elements provide a better gain while the small elements help control the sidelobe level, and the larger the small elements are the larger the overlap.

However, we also want to have at least 3 rings in each of the sub arrays (larger elements and smaller elements) of the CRA (Fig. 2. 34), so that we can explore the non-uniformity in the distances between rings to mitigate the sidelobe level.

Finally, we will avoid having the rings tightly packed so that we can add a reasonable degree of freedom to the variable in the geometry optimization.

Taking those criteria in mind we have chosen empirically a scale factor of 3.5 for the scaled down elements and a base CRA with 3 rings. With the larger rings having a maximal radius of 35 cm, the smaller elements have a maximal radius of 35/3.5 cm, so 10 cm.

This way, in order to have enough empty space in the center of the array to fit the rings of smaller elements, the 3 larger rings occupy the region between the radius of 10 cm and 35 cm. If we account for the cavity size c_{size} (see equation (2.3) and Fig. 2. 12) the smaller ring in the CRA must have a radius larger de 12 cm and the larger ring must have a radius smaller than 33 cm.

2.4.1.2. Optimization

To optimize the geometry we only optimize the spacing of the large rings. The scaled down elements Array Factor will have a similar behavior as the large elements ones, with the difference being that they will present this behavior at higher frequencies.

The optimization procedure used is the same as in section 2.3.2.1. The only difference in the optimization is that there is a constraint in the radius of the first ring to allow for a scaled down copy in the center. The constraints in the geometry variables are shown in equation (2.21).

$$\begin{aligned} \sum_{i=0}^{N_r-1} \Delta_i \leq R_{max} = 33\ cm \\ \Delta_0 > R_{min} = 12\ cm \end{aligned} \tag{2.21}$$

Using equations (2.8) and (2.16) to calculate the cost function, we optimized the new topology with the range of values for the optimized variables presented in Table 2. 12.

Table 2. 12 Optimal values for the larger elements in the Concentric Ring Array with scaled WAVES

Parameter	Δ_0(cm)	Δ_1(cm)	Δ_2(cm)	Φ_1(rad)	Φ_2(rad)	$\sum_{i=0}^{N_r-1} \Delta_i$
Range	12 – 17.7	$d_{r-to-r} - 2\,d_{r-to-r}$	$d_{r-to-r} - 2\,d_{r-to-r}$	0 – Π_1	0 – Π_2	< 33 cm
Optimized Value	15.26	9.20	8.39	0	0.27 rad = 0.11 Π_2	32.85 cm

2.4.1.3. Results

In Table 2. 12 we can see the values of the optimized parameters for the CRA with scaled down WAVES. In Fig. 2. 34 we can see the elements position.

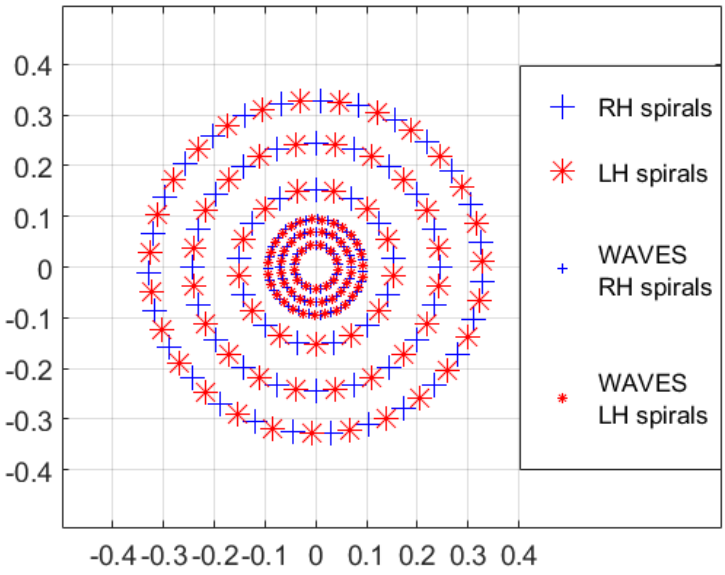

Fig. 2. 34 Elements positions for the Concentric Ring Array of connecting spirals with scaled down WAVES from Table 2. 12.

Fig. 2. 35 shows the AF of the larger elements at 6.9 GHz. Fig. 2. 36 shows the AF of the smaller elements at 6.9 GHz and at 24.15 GHz (3.5 times 6.9).

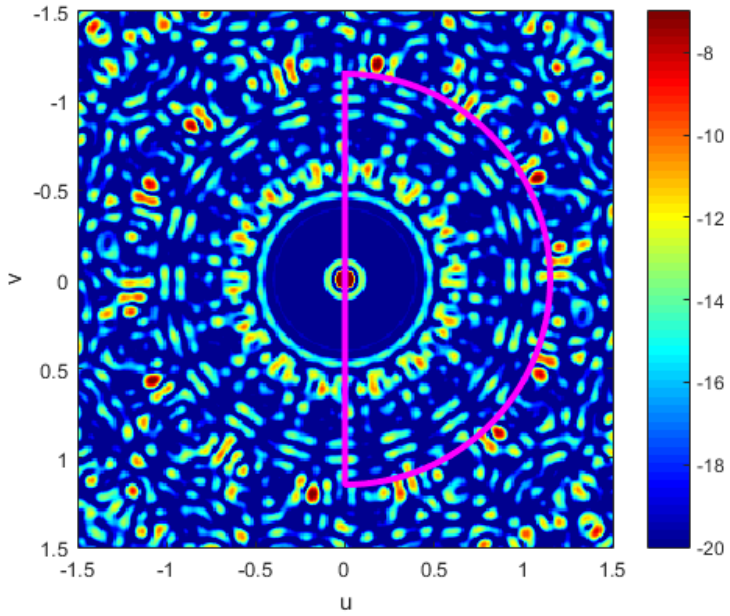

Fig. 2. 35 AF of the larger elements in the optimized Concentric Ring Array with scaled WAVES from Table 2. 12 at 6.9 GHz. In purple we highlight the region in which the sidelobes were optimized.

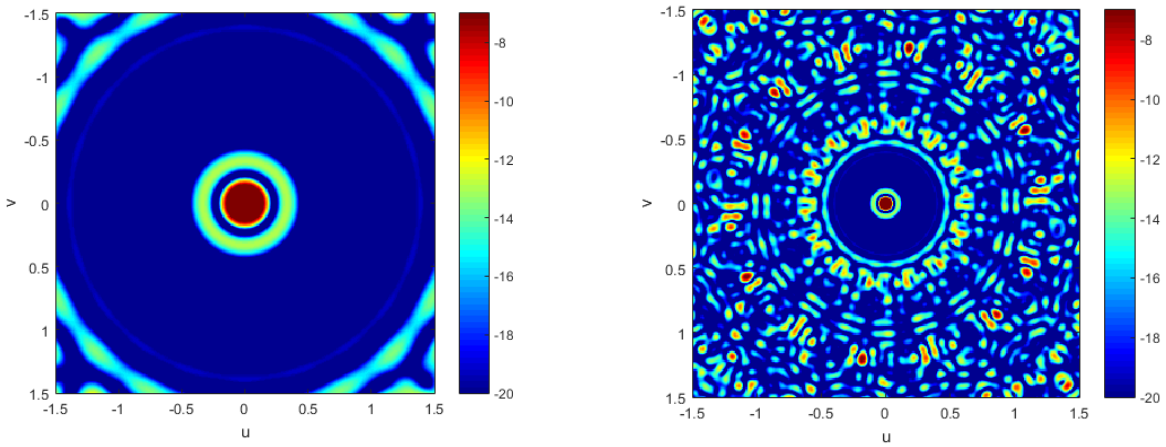

Fig. 2. 36 AF of the smaller elements in the optimized Concentric Ring Array with scaled WAVES from Table 2. 12 at 6.9 GHz (a) and 24.15 GHz (b).

We can see in Fig. 2. 35 that the sidelobes were levelled to around -10 dB in the array factor for the larger elements. The array factor of the smaller elements is simply a scaling of the array factor of the larger elements.

2.4.1.4. Analysis

In order to analyze the array our first approach was to use the approximate expression from equation (2.10) as the element pattern. In order to obtain the fields for the full array we consider three scenarios: the larger spirals turned on and the smaller ones matched to 220Ω, the smaller spirals turned on and the larger ones matched to 220Ω or all the spirals turned on, sending half the power to the larger spirals and half to the smaller spirals.

In order to obtain the RSLL for the arrays, we first calculate the radiated fields for the normal sized antennas and for the small antennas (using (2.10) and (2.12)). With those fields we can directly use (2.13) to obtain the RSLL when only the small or only the normal sized antennas are being fed.

When all antennas are being fed it is important to be careful with the normalization of the calculated electric fields. In our approach we first normalize the electric fields of the larger and smaller elements, calculated as explained in the previous paragraph, so that their radiated power is equal (obtaining E_{big} and E_{small}). Up to this point we did not consider the efficiency of the antennas, so the same input power goes to both the smaller and normal sized elements sub arrays. We use equation (2.22) to take the efficiency of the different sized elements into account.

$$E_{array} = E_{big}\sqrt{\varepsilon_{big}} + E_{small}\sqrt{\varepsilon_{small}} \tag{2.22}$$

with ε_{big} the radiation efficiency of the larger spirals and ε_{small} the radiation efficiency of the smaller spirals.

We get ε_{big} from the FEKO simulation of the CRA from Table 2. 10 (simulation results in Fig. 2. 30). We scale the results from the simulation to get ε_{small}, and for the values that we did not have any data we extrapolated to either 100% (in the higher frequencies for the normal sized elements) or 0.1% efficiency (in the lower frequencies for the smaller elements) (Fig. 2. 37).

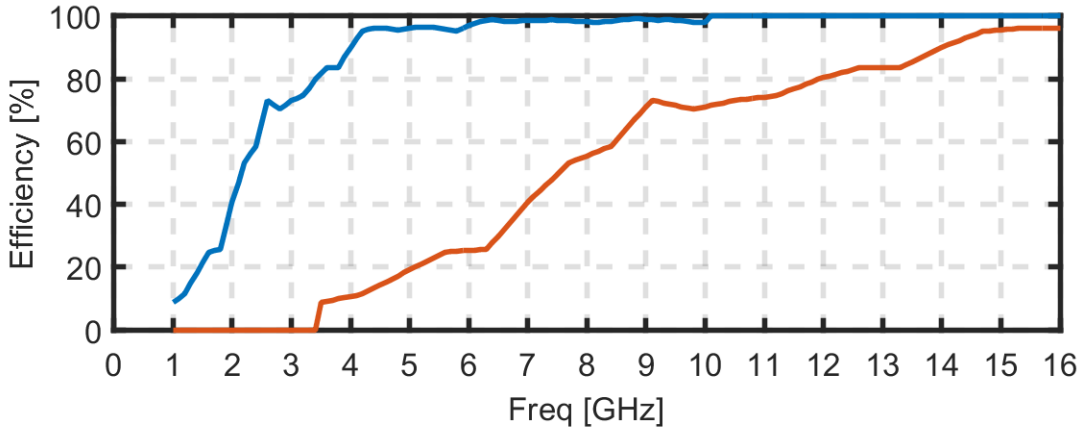

Fig. 2. 37 Efficiency model for the spiral antennas in the Concentric Ring Array with scaled WAVES (see Fig. 2. 34). The blue curve is the efficiency of the normal sized spirals, obtained from Fig. 2. 30. The red curve is the efficiency of the smaller spiral antennas, obtained from scaling the results from the larger elements.

Using this model, we obtained the curves in Fig. 2. 38.

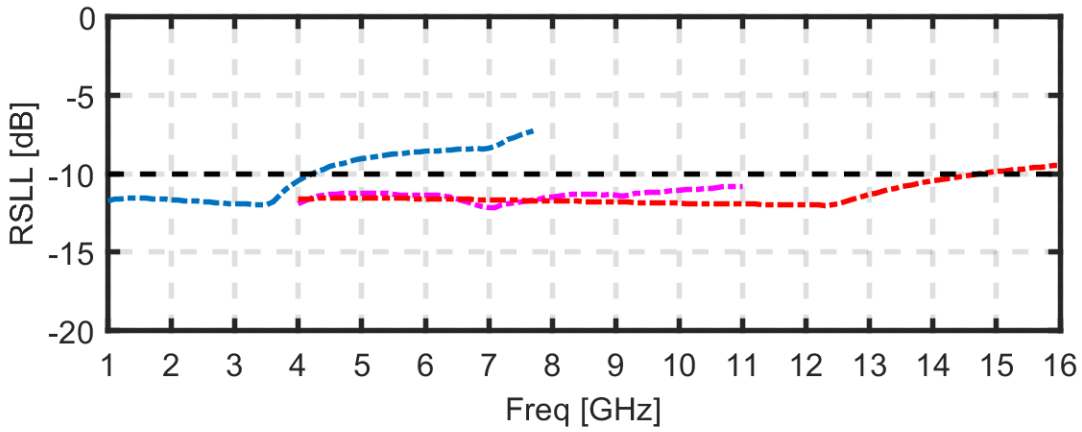

Fig. 2. 38 RSLL for the Concentric Ring Array with scaled WAVES using equation (2.13). The blue curve is the RSLL for the larger elements alone. The purple curve is the RSLL for both the smaller and the larger elements turned on together. The red curve is the RSLL when we have only the smaller elements turned on. The dashed black line is the limit from the specifications.

As we can see in Fig. 2. 38, when using only the normal sized elements (blue) we can keep the RSLL lower than -10 dB up to 4.2 GHz. When using only the small elements, we can keep the RSLL lower than -10 dB up to 14.7 GHz (which is consistent as the smaller elements sub array is simply a scaling of the larger sub array by 3.5, and 4.2 times 3.5 is equal to 14.7).

However, we can still use the larger elements up to 9.5 GHz (at 10 GHz we have a gain drop at broadside and degradation on the Axial Ratio when steering as we can see in Fig. 2. 29 and Fig.

2. 30). In between 4.2 GHz and 9.5 GHz it is desirable to use both the larger and the smaller elements together as it allows for a larger gain and, as is shown in purple in Fig. 2. 38, when we use both together the RSLL is still kept under the -10 dB requirement.

2.4.1.5. FEKO simulation

In order to validate the results, we ran a FEKO simulation of the optimized array. We simulated different scenarios, accessing the performances of the array with both the smaller and the larger elements turned on, only the larger spirals turned on and the smaller loaded with 220 Ω resistances and only the smaller spirals turned on and the larger loaded with 220 Ω resistances. We analyzed those scenarios at broadside and steered to $[\theta_s, \varphi_s] = [30°, 0°]$, for the RHC polarization.

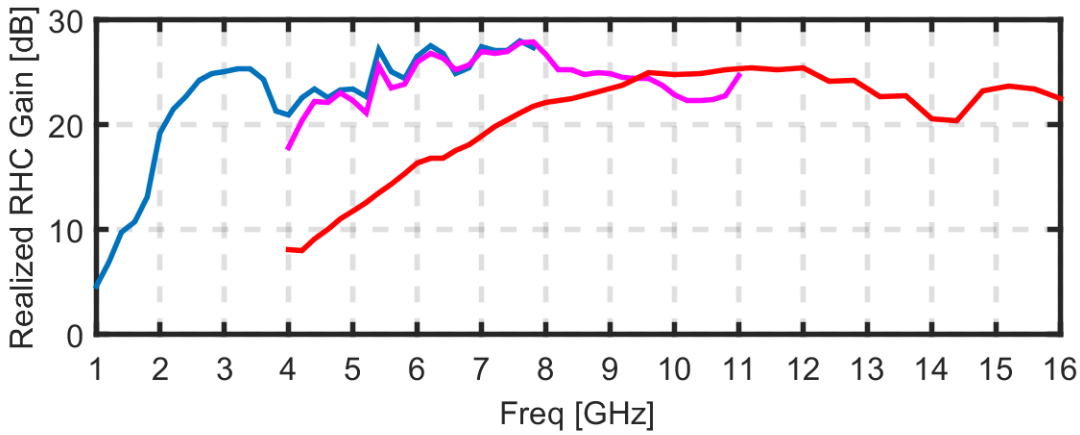

(a)

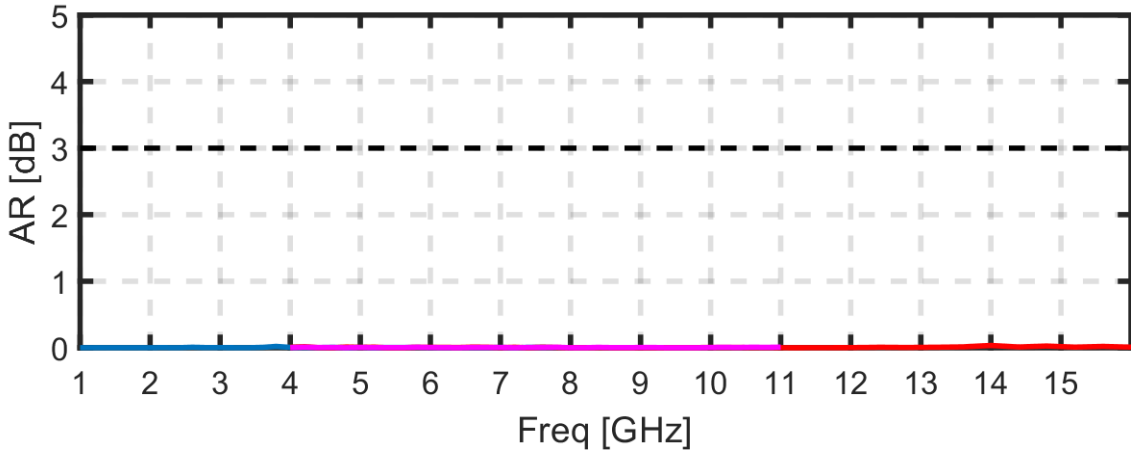

(b)

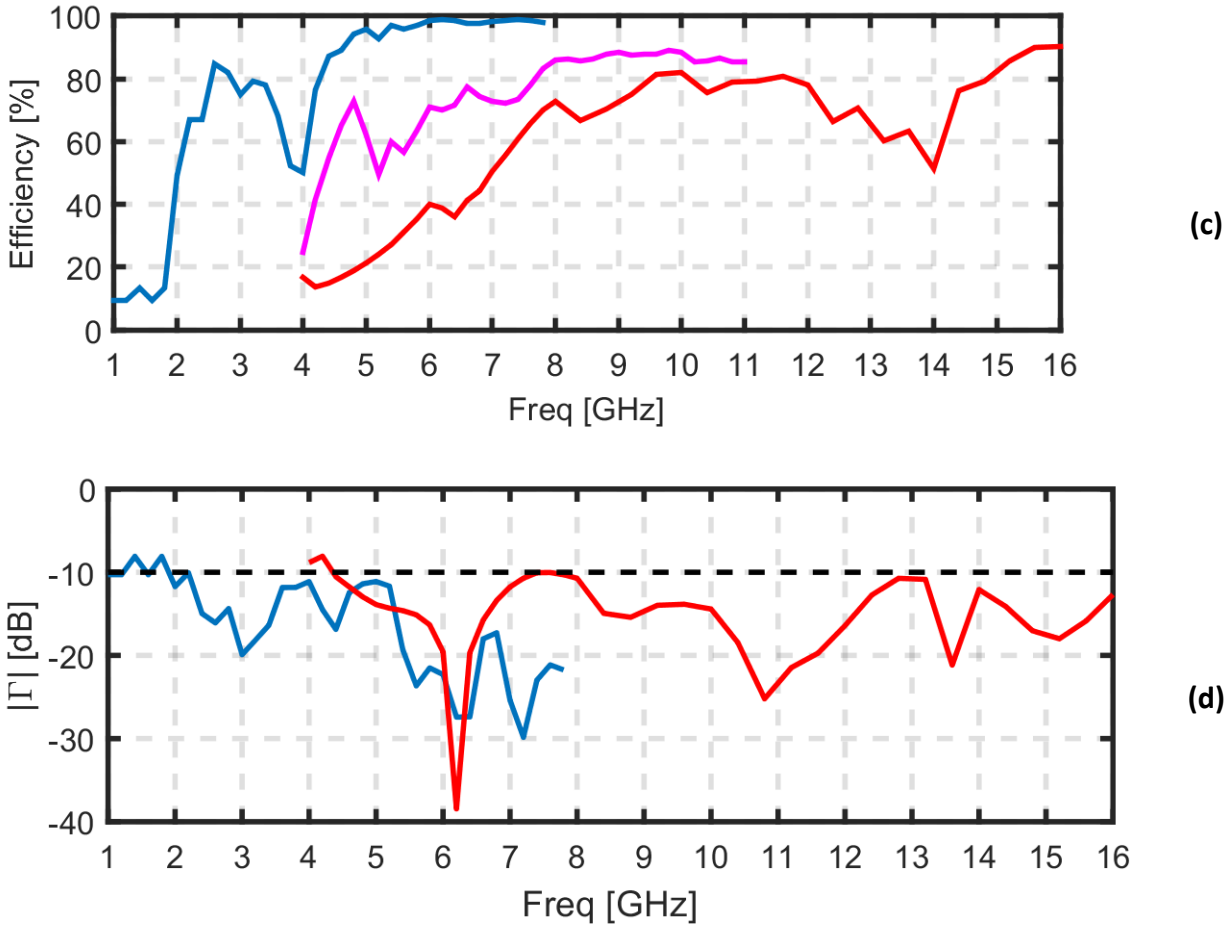

Fig. 2. 39 FEKO simulation of the optimized Concentric Ring Array of connecting Spirals with scaled WAVES of Fig. 2. 34 at broadside. In blue we have the larger elements alone. In purple we have both the smaller and the larger elements turned on together. In red we have only the smaller elements turned on. The dashed black lines indicate the limits from the specifications.

We can observe in Fig. 2. 39 and in Fig. 2. 40 that when only the larger elements are on and the smaller spirals are matched to 220 Ω (blue curves), the array behaves similar to the Concentric Ring Array without WAVES (Fig. 2. 29). However, with only 3 rings of larger spirals, the RSLL limits the band of operations to 4 GHz (Fig. 2. 40 (e), blue curve).

At 4 GHz we start using both the smaller spirals and the larger spirals turned on at the same time (purple curves). We need the smaller spirals to be turned on in order to keep the RSLL under the requirements. The larger spirals are kept on at the same time to provide a better gain compared to the smaller spirals alone.

However, for frequencies above 9.5 GHz the performance of the array starts to degrade when both the smaller and larger spirals are turned on at the same time (Fig. 2. 40 (b) and (e), purple curves) as the larger spirals no longer radiate properly (cavity height equal to $\lambda/2$, see Fig. 2. 29

and Fig. 2. 30). So, for frequencies above 9.5 GHz we use the smaller spirals turned on and the larger spirals matched to 220 Ω (red curves), and the requirements are met up to 13 GHz when the RSLL gets larger than -10 dB (Fig. 2. 40 (e), red curve) .

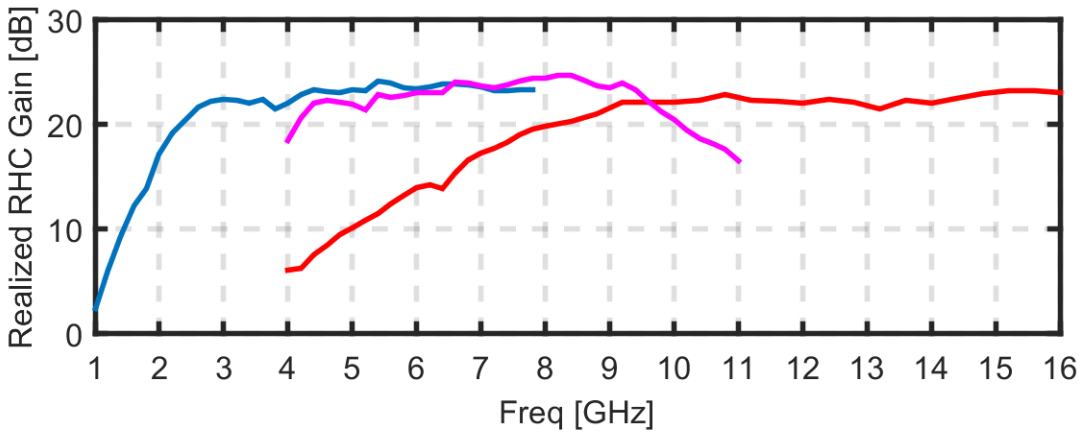

(a)

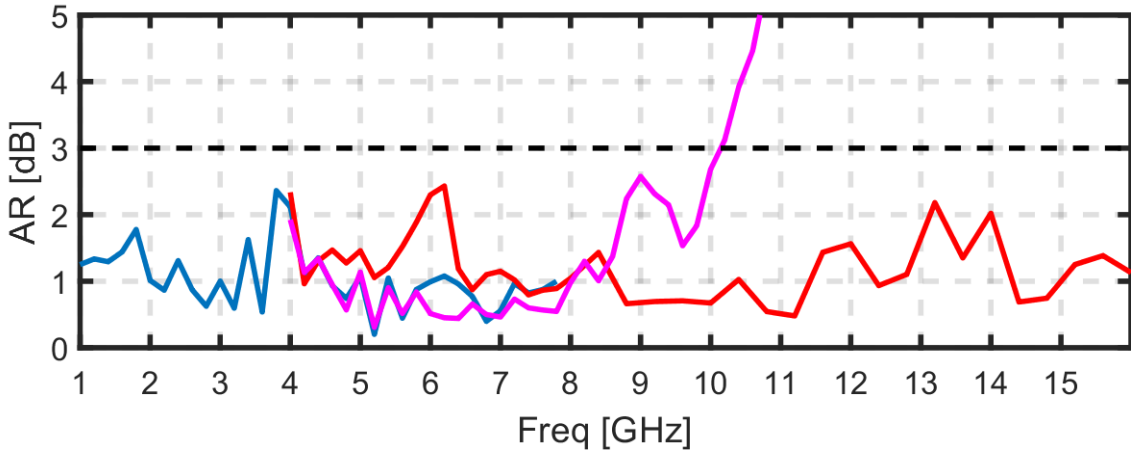

(b)

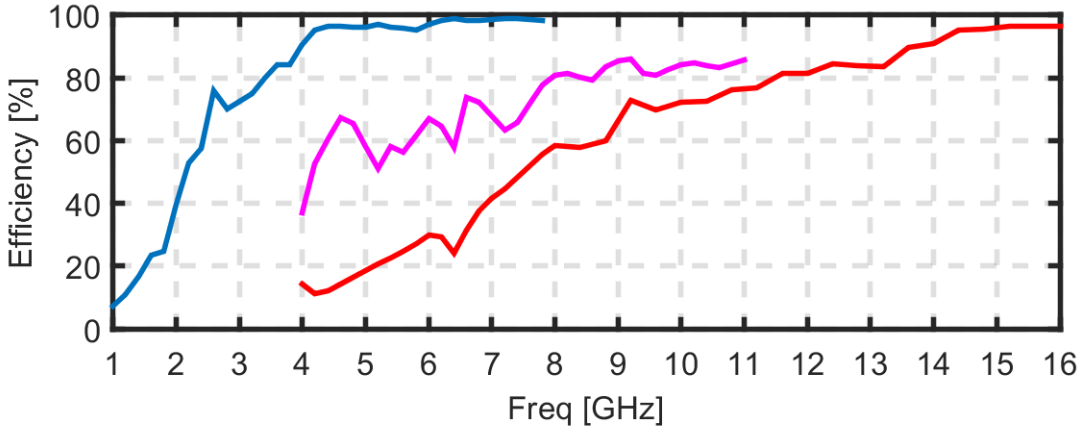

(c)

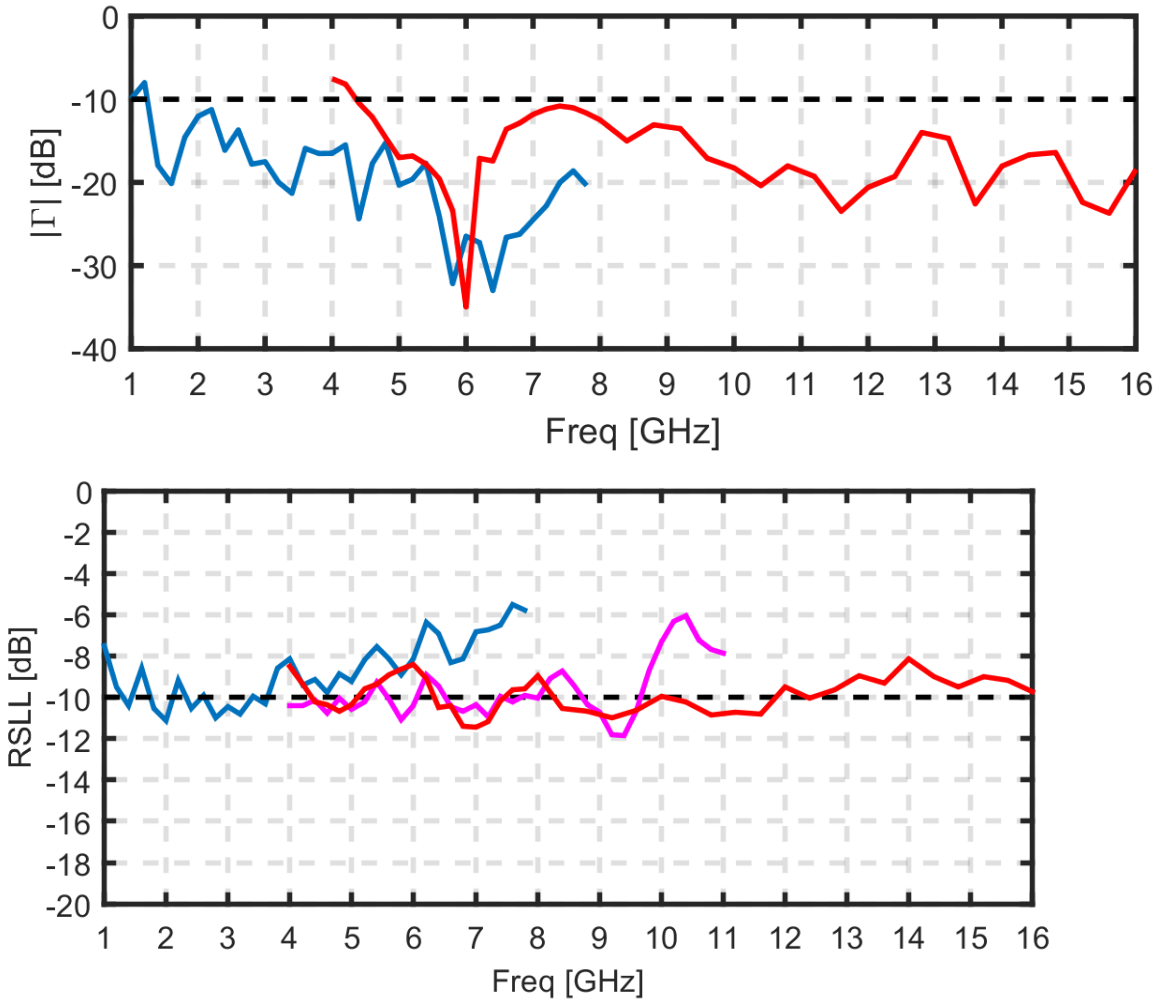

Fig. 2. 40 FEKO simulation of the optimized Concentric Ring Array of connecting Spirals with scaled WAVES of Fig. 2. 34 steering to $[\theta_s, \varphi_s] = [30°, 0°]$. *In blue we have the larger elements alone. In purple we have both the smaller and the larger elements turned on together. In red we have only the smaller elements turned on. The dashed black lines indicate the limits from the specifications.*

The designed array operates as shown in Table 2. 13 and has a bandwidth going from 1 – 13 GHz while steering up to 30° with dual circular polarization and a diameter < 0.7 meter (Fig. 2. 41).

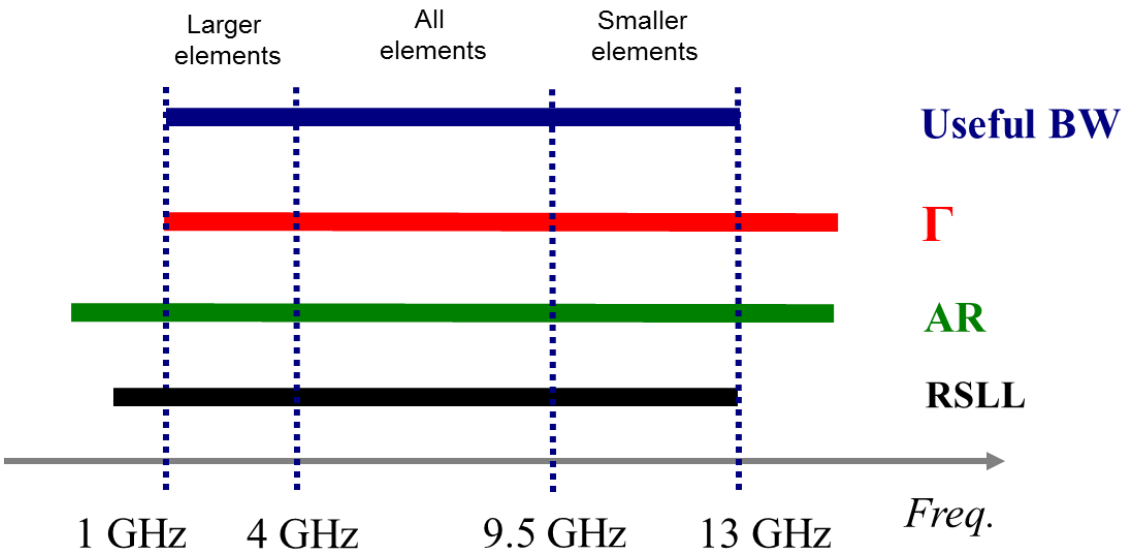

Fig. 2. 41 Frequency range of acceptable performance. The bars correspond to the bandwidth definitions listed. In red we have the bar corresponding to the reflection coefficient, in green the axial ratio and in black the relative sidelobe level. The overall useful bandwidth is the intersection of these three bandwidths.

Table 2. 13 Mode of operation for the Concentric Ring Array with scaled WAVES.

Range (GHz)	Mode of operation
1– 4	Larger elements turned ON and smaller elements matched to 220Ω
4 – 9.5	Both the larger and smaller elements turned ON
9.5 – 13	Smaller elements turned ON and larger elements matched to 220Ω.

Moreover, we can see in that the RSLL obtained in the FEKO simulation is larger than what was predicted with our approximate model (Fig. 2. 38). This happens because, as with the Concentric Ring Array, the first sidelobe is larger in the simulation than expected (e.g. Fig. 2. 26). If we take that into account in our optimization we can expect the final array to have a larger bandwidth.

2.4.1.6. Optimization with weighting of 1st lobe

As we have seen, the ring lobe around the main beam is larger than predicted by our approximate model, which reduces the array's bandwidth. In order to compensate this effect we used the cost function of 2.3.3. However, when we tried optimizing using $\gamma = \sqrt{2}$, the

optimized array had a very similar level on the first lobe, so we tried using larger values for γ. If the value of γ was too high the sidelobes on the first grating lobe region get higher, which would affect the bandwidth of the array. We found that $\gamma = 1.6$ gave a good compromise.

The parameters of the newly optimized array are shown in Table 2. 14, the AF of the optimized array is in Fig. 2. 42 and the estimated RSLL using (2.13) is in Fig. 2. 43.

Table 2. 14 Optimal values for the larger elements in the Concentric Ring Array with scaled WAVES with weighting of $\gamma = 1.6$ in the 1st lobe.

Parameter	Δ_0(cm)	Δ_1(cm)	Δ_2(cm)	Φ_1(rad)	Φ_2(rad)	$\sum_{i=0}^{N_r-1} \Delta_i$
Optimized Value	13.07	9.23	9.39	0.20 rad = 0.60 Π_1	0.01 rad = 0.05 Π_2	31.69 cm

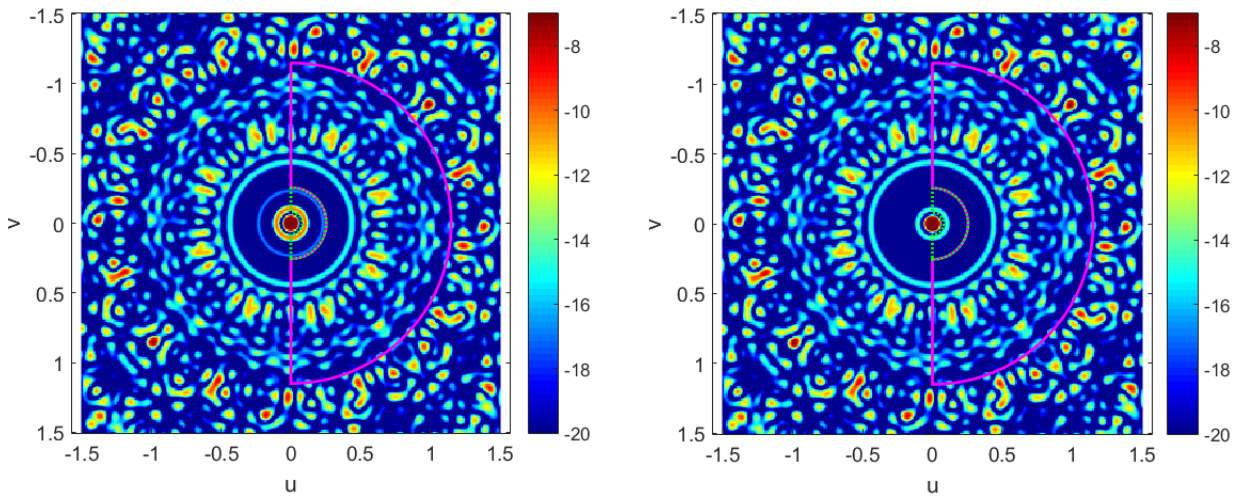

Fig. 2. 42 Array factor of the larger elements in the optimized concentric ring array with scaled WAVES weighting the first sidelobe by 1.6 (see Table 2. 14), at 6.9 GHz. In purple we highlight the zone in which we searched for the highest sidelobe excluding the first sidelobe and in dotted green we highlight the zone that was weighted by1.6. In (a) the Array Factor of the optimal array with the weighting and in (b) without the weighting.

In Fig. 2. 35 the first sidelobe is at a level of -13 dB while in Fig. 2. 42 it is at -14.3 dB, 1.3 dB lower, which should help compensate the rise in the first sidelobe observed in the FEKO simulations (Fig. 2. 40).

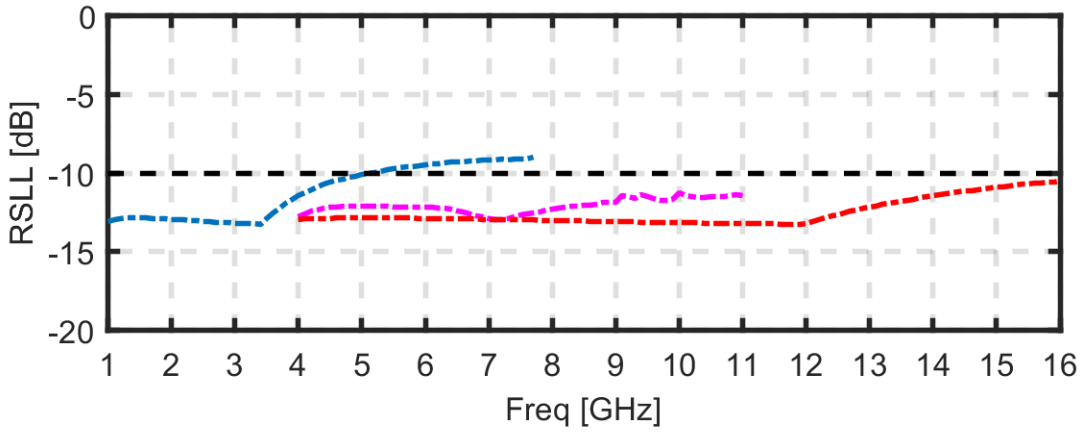

Fig. 2. 43 RSLL obtained using equation (2.13) for the Concentric Ring Array with scaled WAVES weighting the 1st lobe in the optimization (Table 2. 14). The blue curve is the RSLL for the larger elements alone. The purple curve is the RSLL for both the smaller and the larger elements turned on together. The red curve is the RSLL when we have only the smaller elements turned on. The dashed black line is the limit from the specifications.

Comparing Fig. 2. 38 and Fig. 2. 43 we can see that the RSLL predicted by our model is 1.3 dB lower in the new optimization in the lower frequencies. We did not have the time to run a FEKO simulation to validate this approach, but we expect from the results of section 2.3 that the FEKO simulations should give results similar to those in Fig. 2. 43.

2.4.2. Concentric Ring Array with interleaved WAVES

As a second approach to include smaller elements to extend the bandwidth of the Concentric Ring Array, we tested the possibility of adding rings of spirals with half the diameter in between the rings of the optimized CRA of normal sized elements. The potential advantage of this approach compared to the scaled WAVES approach is that the smaller elements are larger in comparison, which can allow for better gain in the mid frequencies where we first turn the WAVES elements to control the sidelobe level.

2.4.2.1. Geometry

The geometry consists of a 3-ring concentric ring array with dimensions as described in section 2.3.1.1, but in between those rings we add rings that can also be described as in section 2.3.1.1, but with the spirals having half the diameter (see Fig. 2. 44).

To assure that the space between the larger rings is sufficient for the smaller rings to fit we change the distance between larger rings as follows:

$$d_{r-to-r} = 2.4\, D_{spi} = 7.6\, cm \tag{2.23}$$

In Fig. 2. 33 we present the array dimensions in terms of the distance between rings and the relative rotations of the rings, in (a) for the larger rings using Δ_i for the distance between rings and Φ_i for the relative rotations, in (b) for the smaller interleaved rings using $\Delta \mathrm{w}_i$ for the distance between rings and $\Phi \mathrm{w}_i$ for the relative rotations.

It is interesting to also define the geometry of the smaller interleaved rings in terms of the relative rotations $\Phi \mathrm{w}_i$ (as before) and the radius of the rings $\mathrm{r\,w}_i$ instated of the distance between rings $\Delta \mathrm{w}_i$, with both related to each other by the equation (2.24).

$$\begin{aligned} \mathrm{r\,w}_0 &= \Delta \mathrm{w}_0 \\ \mathrm{r\,w}_i &= \sum_{j=0}^{i-1} \Delta \mathrm{w}_j \,, i > 0 \end{aligned} \tag{2.24}$$

2.4.2.2. Optimization

In order to optimize this array we use a two-step optimization. At first we optimize the larger elements positioned in the same way as in section 2.3.2. The results are shown in Table 2. 15.

Table 2. 15 Optimal values for the larger elements in the Concentric Ring Array with interleaved WAVES of Fig. 2. 44.

Parameter	Δ_0(cm)	Δ_1(cm)	Δ_2(cm)	Φ_1(rad)	Φ_2(rad)	$\sum_{i=0}^{N_r-1} \Delta_i$
Range	3.5 – 23.5	$d_{r-to-r} - 2\, d_{r-to-r}$	$d_{r-to-r} - 2\, d_{r-to-r}$	0 – Π_1	0 – Π_2	< 33 cm
Optimized Value	10.65	11.10	10.69	0.17 rad = 0.49 Π_1	0.22 rad = 0.95 Π_2	32.44 cm

Then, having the optimized array of larger elements, we calculate the feasible radius for the smaller rings in order to choose the range of values for the radius $\mathrm{r\,w}_i$ of each of the rings. Then, we optimize the position of the smaller rings.

In order to do so, we calculate the AF of the array including the large and the small elements together, and then we use the cost function from section 2.3.2, but instead of normalizing the u-v space by d_{elem}/λ as in equation (2.16) (with d_{elem} being the distance between elements of the same polarization in the larger rings) we normalize it by d_{elemW}/λ (with $d_{elemW} = d_{elem}/2$ being the distance between elements of the same polarization in the smaller rings) as in equation (2.25).

$$RSLL = max_{\left(u,v \in \left(\frac{u\, d_{elemW}}{\lambda}\right)^2+\left(\frac{v\, d_{elemW}}{\lambda}\right)^2 \leq 1.85^2, u\geq 0\ \&\ u,v \notin mainbeam\right)} (20\, log_{10}|AF_{norm}(u,v) \quad (2.25)$$

The resulting dimensions for the smaller elements positions are given in Table 2. 16

Table 2. 16 Optimal values for the smaller elements in the Concentric Ring Array with interleaved WAVES of Fig. 2. 44.

Parameter	$\mathrm{r\,w}_0$(cm)	$\mathrm{r\,w}_1$(cm)	$\mathrm{r\,w}_2$(cm)	$\Phi\mathrm{w}_0$(rad)	$\Phi\mathrm{w}_1$(rad)	$\Phi\mathrm{w}_2$(rad)
Range	1.76 – 6.83	14.46 – 17.93	25.56 – 28.62	0 – $\Pi\mathrm{w}_0$	0 – $\Pi\mathrm{w}_1$	0 – $\Pi\mathrm{w}_2$
Optimized Value	5.28	15.85	26.79	0 rad = 0 $\Pi\mathrm{w}_0$	0.22 rad = 0.96 $\Pi\mathrm{w}_1$	0.06 rad = 0.42 $\Pi\mathrm{w}_2$

2.4.2.3. Results and analysis

In Fig. 2. 44 we show the position of the elements from the optimized Concentric Ring Array with interleaved WAVES.

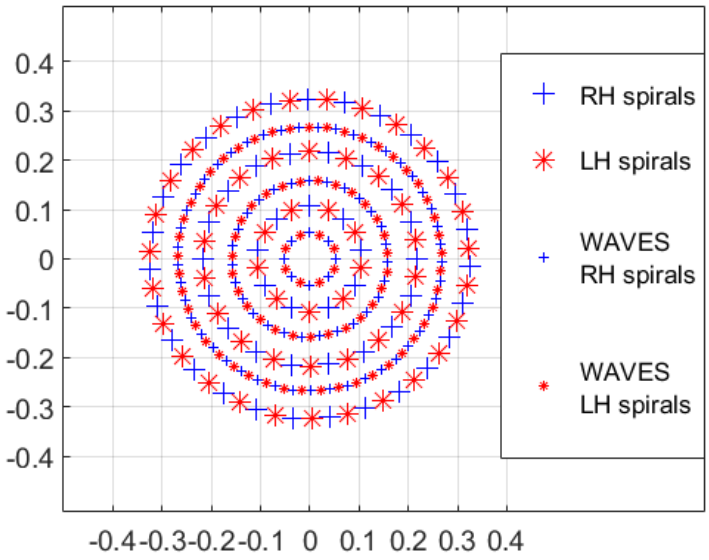

Fig. 2. 44 Elements position for the optimized concentric ring array with interleaved WAVES.

Then we used the same procedure used in section 2.4.1.4 to calculate the RSLL of the optimized array. The values of the efficiencies of the larger and smaller spirals used for the model are shown in Fig. 2. 45 and the resulting RSLL curves are shown in Fig. 2. 46.

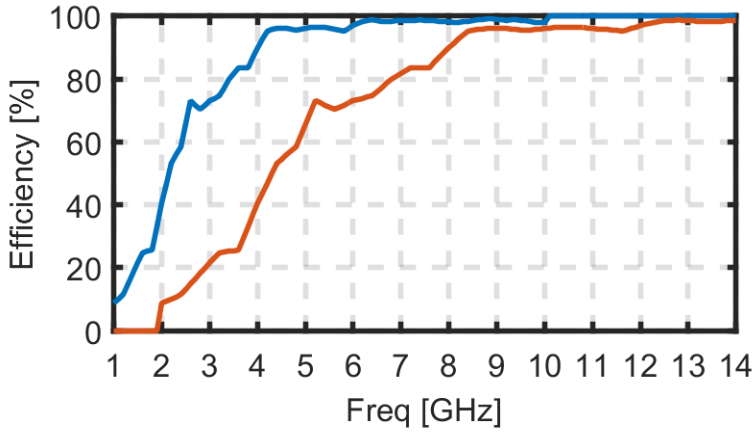

Fig. 2. 45 Efficiency model for the spiral antennas in the Concentric Ring Array with scaled WAVES of Fig. 2. 44. The blue curve is the efficiency of the normal sized spirals, obtained from Fig. 2. 30. The red curve is the efficiency of the smaller spiral antennas, obtained from scaling the results from the larger elements.

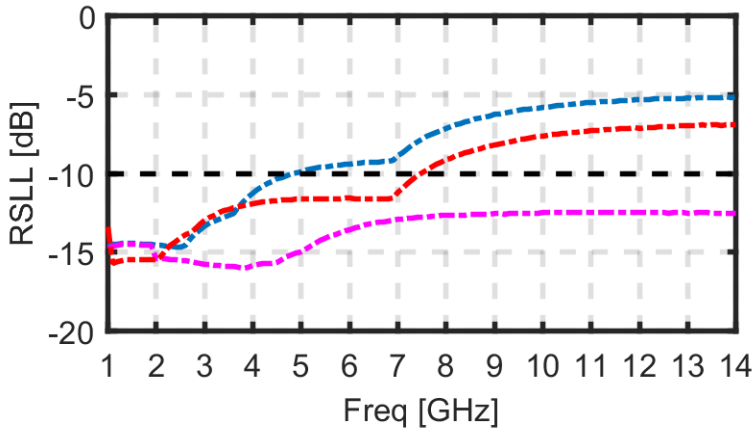

Fig. 2. 46 RSLL for the Concentric Ring Array with interleaved WAVES of Fig. 2. 44 using equation (2.13). The blue curve is the RSLL for the larger elements alone. The purple curve is the RSLL for both the smaller and the larger elements turned on together. The red curve is the RSLL when we have only the smaller elements turned on. The dashed black line is the limit from the specifications.

Observing Fig. 2. 46 we would expect the array to meet the requirements for very high frequencies. However, we should not use the larger elements above 9.5 GHz as at 10 GHz we have a drop gain at broadside and degradation on the Axial Ratio when steering (Fig. 2. 29 and Fig. 2. 30). Thus we can expect two modes of operation: one using only the larger elements from 1 GHz to 5 GHz and another from 5 up to around 9.5 GHz using both the small and large antennas together.

2.4.2.4. FEKO simulation

In order to validate the results, we decided to run a FEKO simulation of the optimized array. In Fig. 2. 47 we simulate the case when both the small and the large antennas are turned on at the same time, at broadside and steering to 30°, for the RHC polarization.

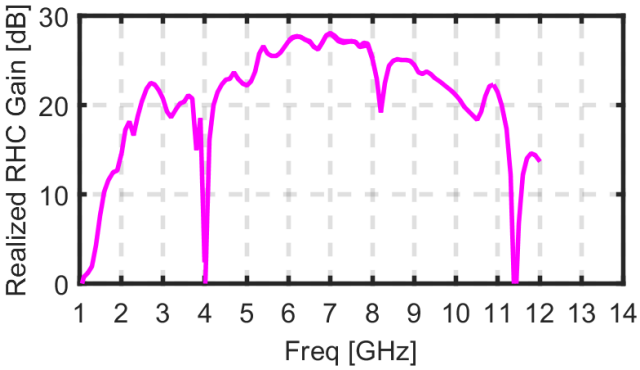

(a)

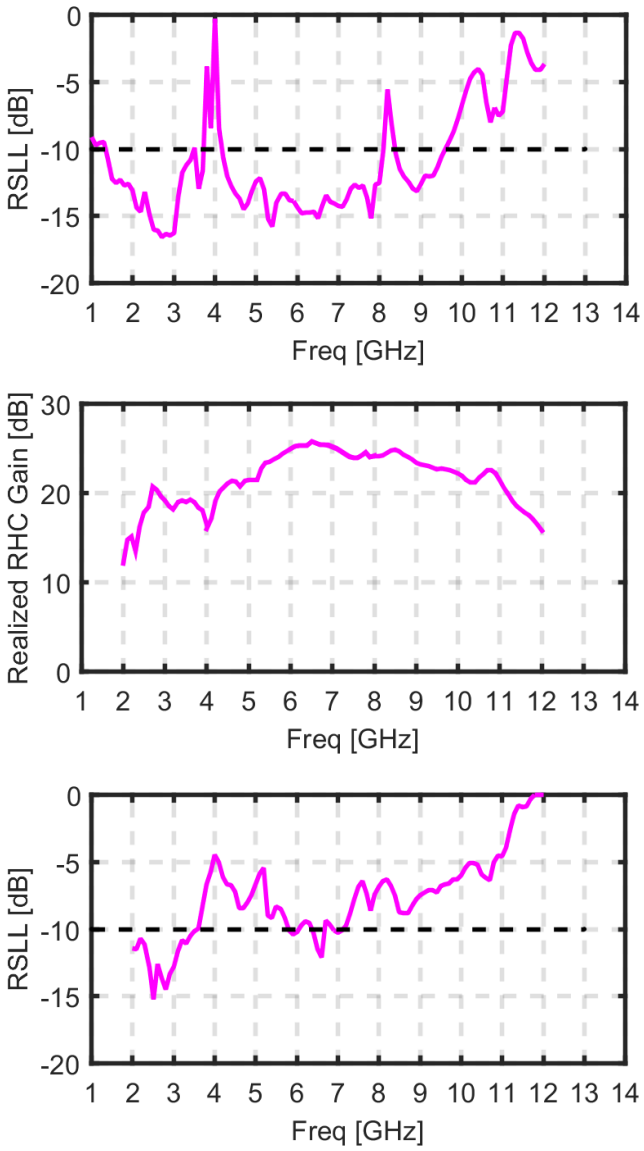

Fig. 2. 47 FEKO simulation of the optimized Concentric Ring Array of connecting Spirals with interleaved WAVES of Fig. 2. 44 with all elements turned on at broadside (in (a) the realized RHC gain and in (b) the RSLL) and steering to 30° (in (c) the realized RHC gain and in (d) the RSLL). The dashed black lines indicate the limits from the specifications.

As we can see in Fig. 2. 47 (a), there is a huge drop in the gain of the simulated array at 4 GHz and 8.2 GHz at broadside. It is probably linked to the distance between elements as $\lambda_{4\ GHz} = 7.5\ cm \sim d_{elem}$, where d_{elem} is the distance between elements of the same polarization in a ring. We have seen this effect in the Concentric Ring Array (Fig. 2. 7 and Fig. 2. 29) and in the Concentric Ring Array with scaled WAVES (Fig. 2. 39), but it is much more intense in this topology. In Fig. 2. 48 we show the radiating patterns of the array at broadside at 3 GHz and at 4

GHz. In Fig. 2. 49 we show the radiating patterns of the array at broadside at 8.2 GHz and at 8.4 GHz.

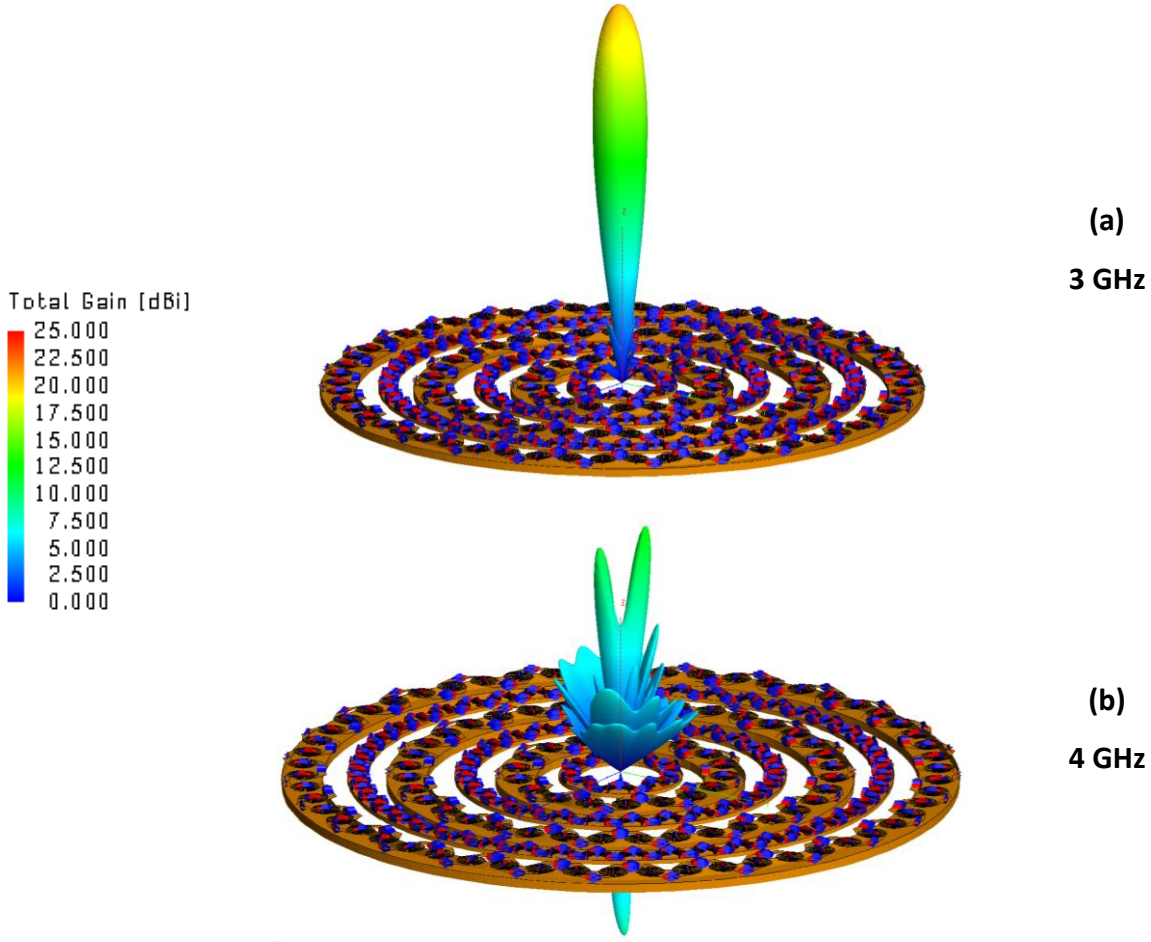

Fig. 2. 48 Radiating Pattern from the FEKO simulation of the optimized Concentric Ring Array of connecting Spirals with interleaved WAVES of Fig. 2. 44 with all elements turned on at broadside. In (a) we have the Radiating Pattern at 3 GHz and in (b) at 4 GHz.

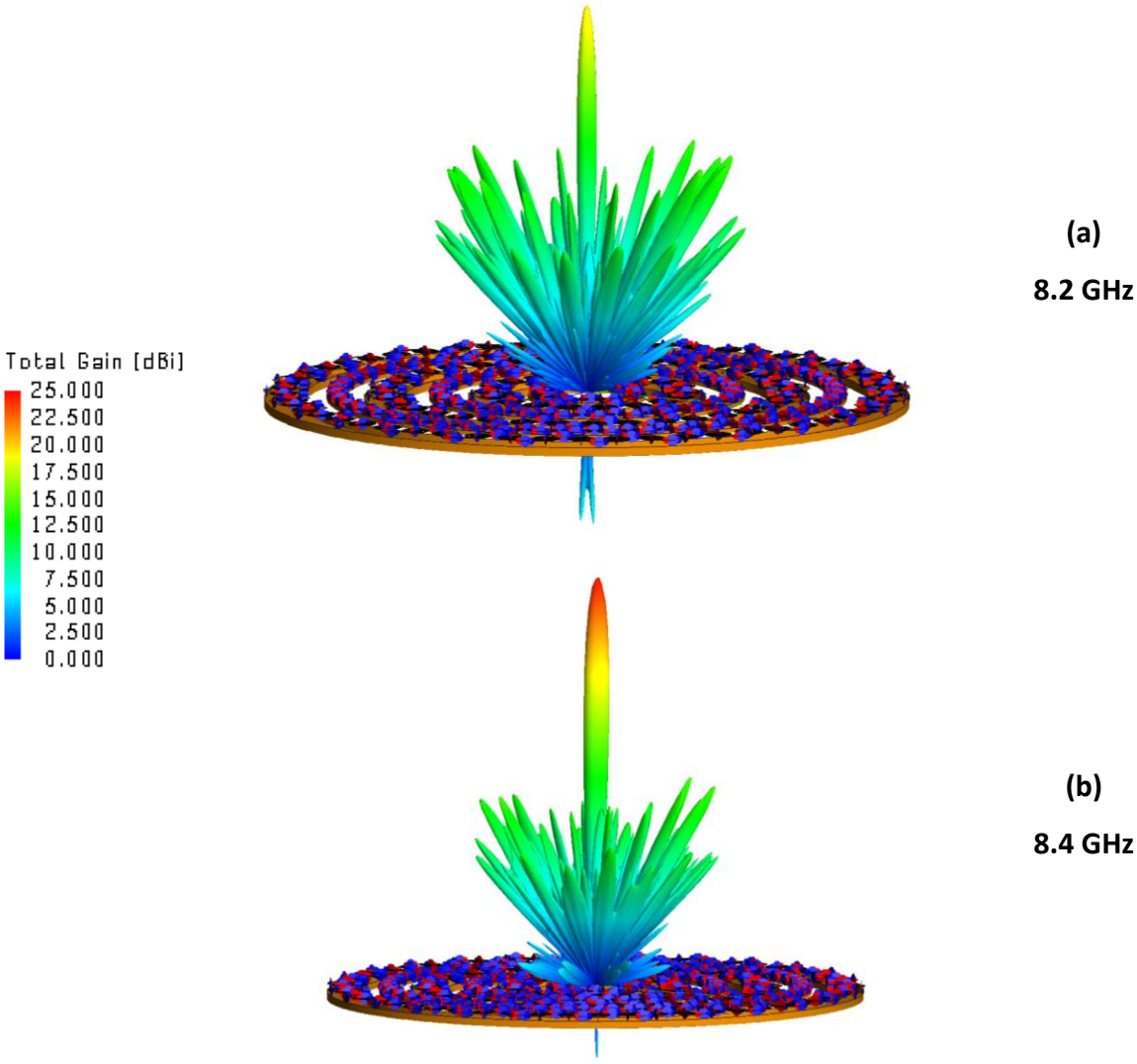

Fig. 2. 49 Radiating Pattern from the FEKO simulation of the optimized Concentric Ring Array of connecting Spirals with interleaved WAVES of Fig. 2. 44 with all elements turned on at broadside. In (a) we have the Radiating Pattern at 8.2 GHz and in (b) at 8.4 GHz.

The drop in gain is smaller when steering to 30°, but is still present as we can see in Fig. 2. 47 (c). In Fig. 2. 50 we show the radiating pattern of the array steered to 30° at 3 GHz and at 4 GHz.

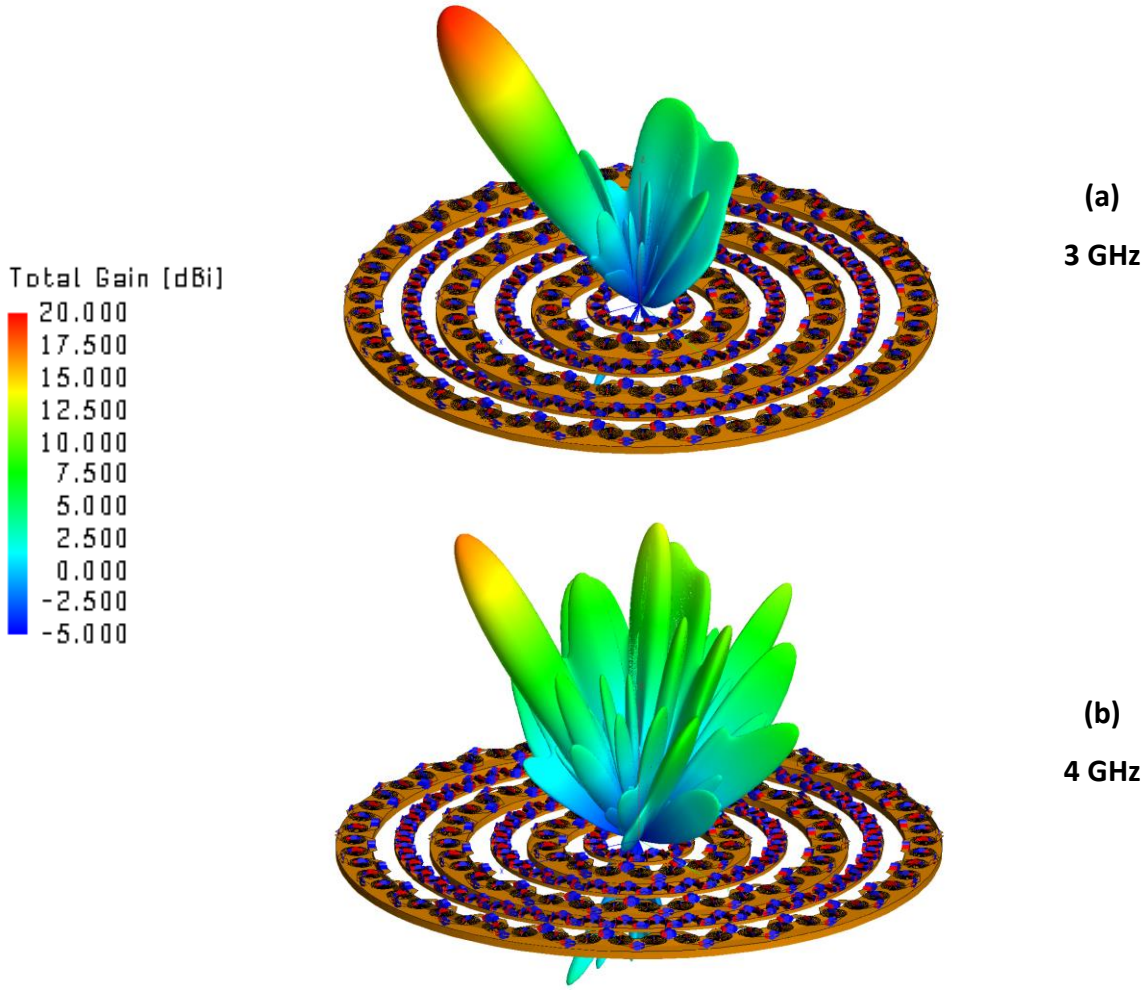

Fig. 2. 50 Radiating Pattern from the FEKO simulation of the optimized Concentric Ring Array of connecting Spirals with interleaved WAVES of Fig. 2. 44 with all elements turned on steered to 30°. In (a) we have the Radiating Pattern at 3 GHz and in (b) at 4 GHz.

At 4 GHz and 8 GHz we can also see a rise in the RSLL. In Fig. 2. 47 (b) we see that the rise in the RSLL at broadside is as sharp as the drop in the gain. I Fig. 2. 47 (d) we can see that the rise in the RSLL is broader and lower when steering to 30°, however still larger than the -10 dB requirements.

We did not have the time to further analyze the reasons for those effects, but we assume that it is due to the proximity of the rings in this topology, which probably augments mutual coupling effects that are not accounted for in our models.

Due to time constraints we chose not to simulate the other scenarios for this array.

2.4.3. Comparison CRA and CRA with WAVES

In order to understand the trade-offs in using the WAVES technique in the Concentric Ring Array design, we will compare the realized RHC gain and the RSLL performances of the Concentric Ring Array from section 2.3.3 and the Concentric Ring Array with scaled WAVES from section 2.4.1 (Fig. 2. 51 and Fig. 2. 52).

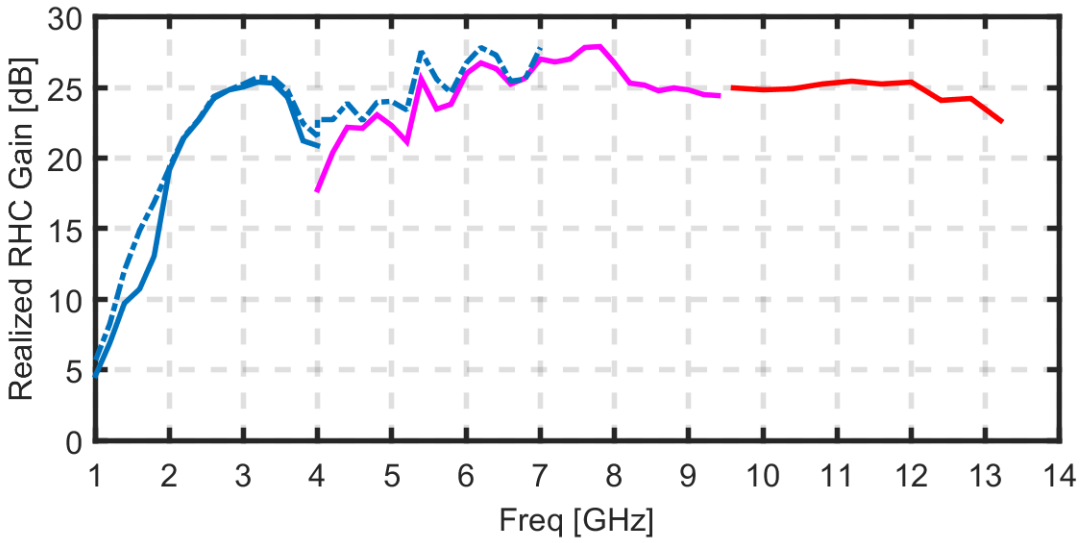

Fig. 2. 51 Realized RHC gain curves when pointing at broadside from the Concentric Ring Array of Table 2. 10 from section 2.3.3 (blue dashed line) and from the Concentric Ring Array with scaled WAVES of Fig. 2. 34 from section 2.4.1 with only the larger elements turned on (blue), both the larger and the smaller on at the same time (purple) and only the smaller elements on (red).

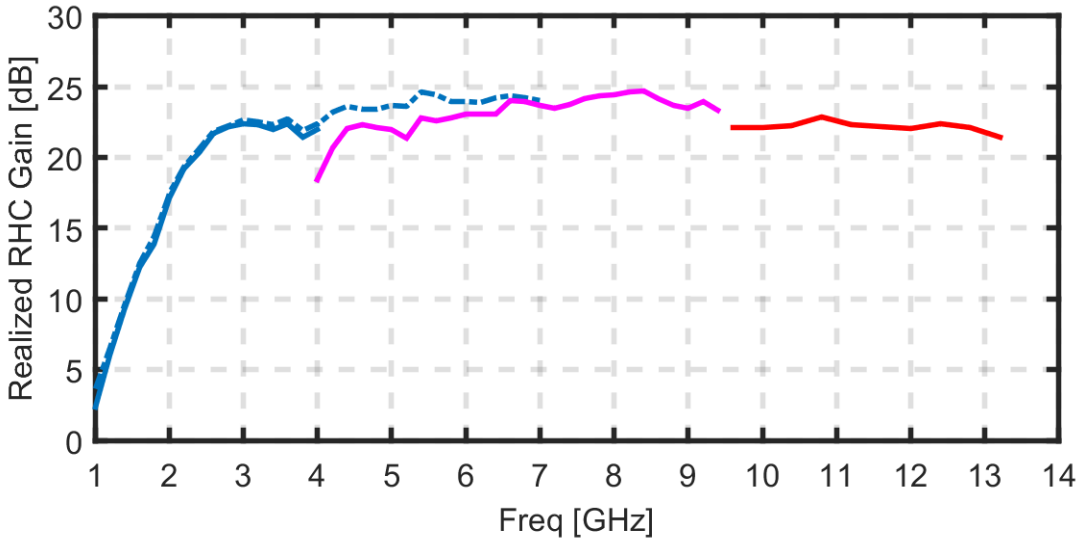

Fig. 2. 52 Realized RHC gain curves when steering to 30° from the Concentric Ring Array of Table 2. 10 from section 2.3.3 (blue dashed line) and from the Concentric Ring Array with scaled WAVES of Fig. 2. 34 from section 2.4.1 with only the larger elements turned on (blue), both the larger and the smaller on at the same time (purple) and only the smaller elements on (red).

We can observe that there is a trade-off between gain in the mid frequencies and RSLL bandwidth. With the constraints on the radius of the rings, the CRA with WAVES requires both the larger and smaller elements to be turned on for frequencies above 4 GHz to control the RSLL, which causes a reduction of about 1.7 dB in gain between 4 GHz and 6 GHz as the smaller elements have a low efficiency at those frequencies. There is also a larger complexity in operating the array with WAVES.

The upside in this trade-off is augmenting the bandwidth from 1-6.9 GHZ to 1-13 GHz.

2.5. Conclusion of chapter 2

In this chapter we explored the Concentric Ring Array of Connecting Spirals topology. A genetic algorithm optimization of the rings radius and relatives rotations has been proposed to enhance the RSLL bandwidth of the array while maintaining a compact design.

The developed array (of Table 2. 10) has a bandwidth of 1 GHz - 6.9 GHz while steering up to 30° with dual circular polarization and a diameter < 0.7 meter (Fig. 2. 53).

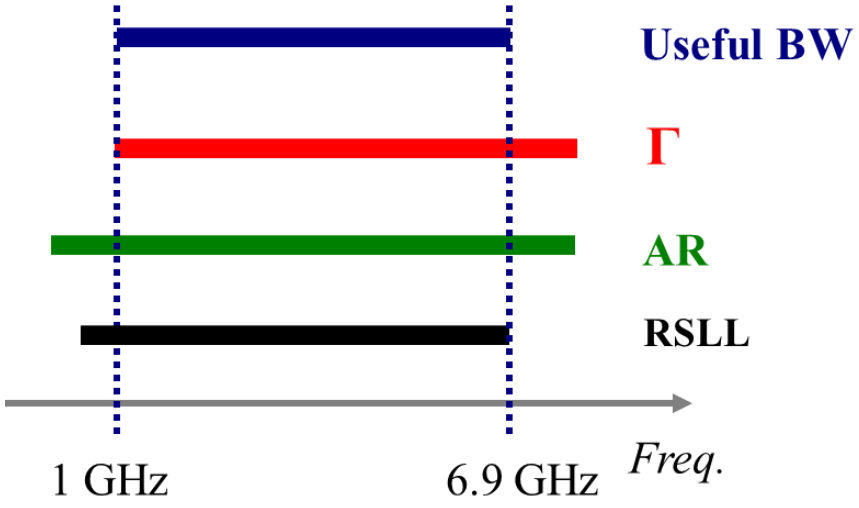

Fig. 2. 53 The bars correspond to the bandwidth definitions listed. In red we have the bar corresponding to the reflection coefficient, in green the axial ratio and in black the relative sidelobe level. The overall useful bandwidth is the intersection of these three bandwidths.

With the WAVES technique integrated into the topology, as in Fig. 2. 34, there is an extension of the bandwidth from 1 GHz – 13 GHz while steering up to 30° with dual circular polarization and a having a diameter < 0.7 meter (Fig. 2. 54).

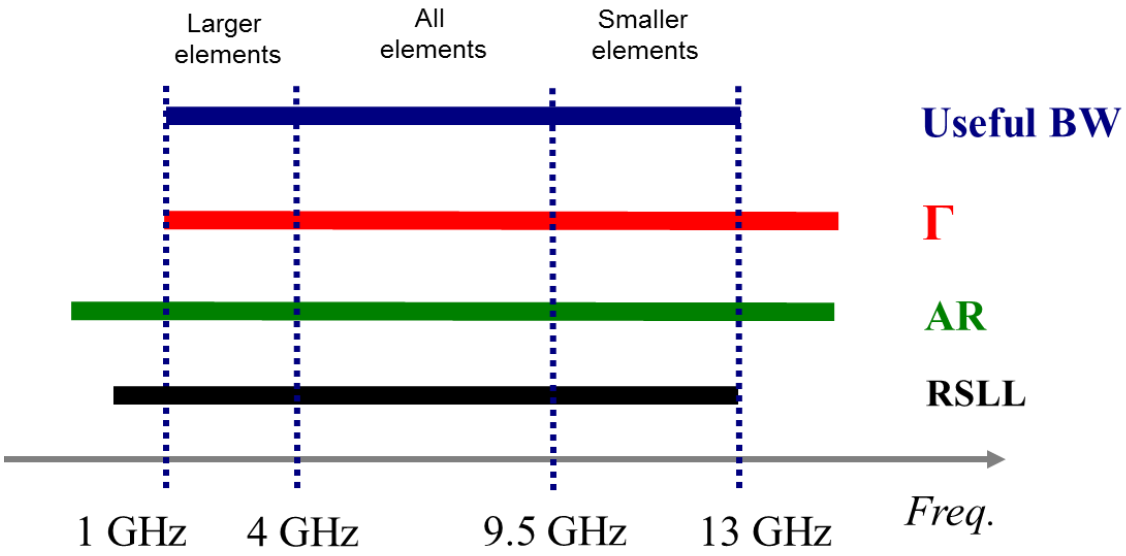

Fig. 2. 54 The bars correspond to the bandwidth definitions listed. In red we have the bar corresponding to the reflection coefficient, in green the axial ratio and in black the relative sidelobe level. The overall useful bandwidth is the intersection of these three bandwidths.

In Fig. 2. 55 we superpose the realized RHC gain of those arrays, the maximal surface gain corresponding to the 35 cm radius circle in which the arrays are inscribed (0.38 m^2) and the

maximal surface gain corresponding to the area occupied by the cavities in the arrays, that by chance is approximately the same for the Concentric Ring Array and for the Concentric Ring Array with WAVES (0.2 m^2).

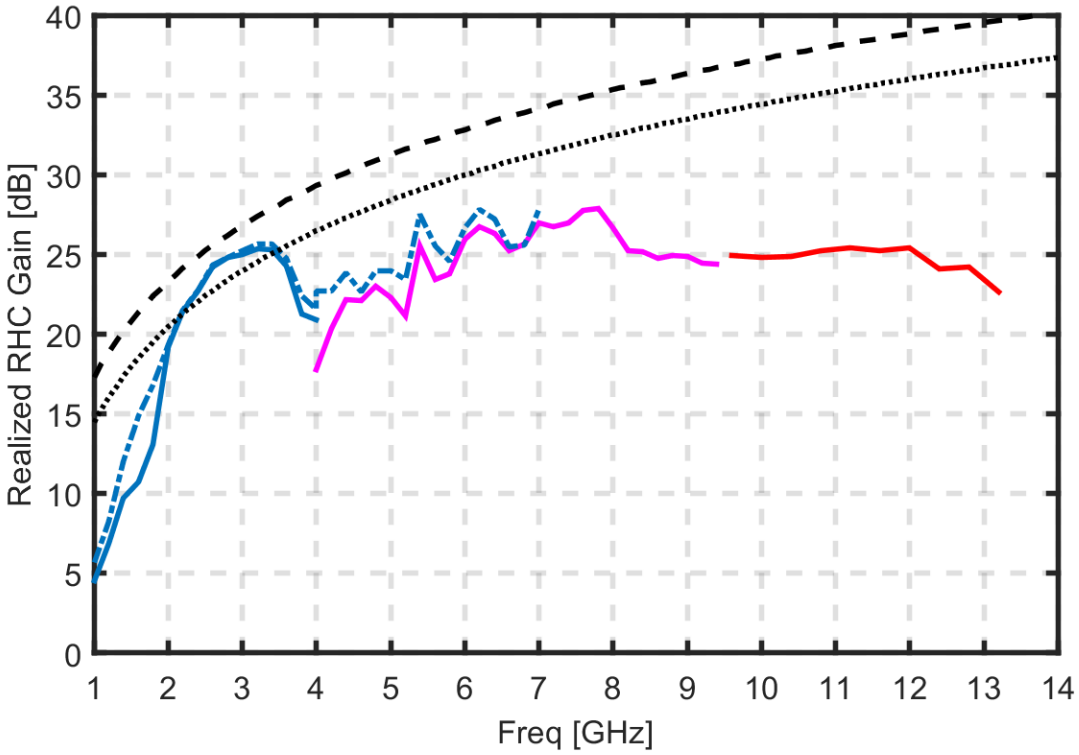

Fig. 2. 55 Realized RHC gain curves when pointing at broadside from the Concentric Ring Array from section 2.3.3 (blue dashed line) and from the Concentric Ring Array with scaled WAVES from section 2.4.1 with only the larger elements turned on (blue), both the larger and the smaller on at the same time (purple) and only the smaller elements on (red). Superposed we have the maximal surface gain corresponding to the 35 cm circle in which the arrays are circumscribed, which has an area of 0.38 m^2 , (black dashed line) and corresponding to the area occupied by the cavities of the CRA or the CRA with scaled WAVES, both which have 0.2 m^2 (dotted black line).

As we can see in Fig. 2. 55, the gain of the array around 3 GHz is almost as high as the theoretical surface gain of the disk in which the array is circumscribed.

However, we can see in Fig. 2. 55 that the gain is far from the theoretical surface gain in the lower and higher end of the bandwidth. In the lower frequencies the connections absorbs too much power (low efficiency) and in the higher frequencies the currents are concentrated in the center of the spirals (low aperture efficiency). To address this disadvantage, we propose a different topology in chapter 3.

References

Caswell, E. D., “Design and Analysis of Star Spiral with Application to Wideband Arrays with Variable Element Sizes,” Ph.D. dissertation, Virginia Polytechnic Institute and State University, Virginia, USA, 2001.

Guinvarc'h, R., Serhir, M. and Ribière-Tharaud, N., “A cavity-backed dual polarized array of connected spiral antennas,” *Proceedings of the 2012 IEEE International Symposium on Antennas and Propagation (APSURSI)*, July 2012.

Hinostroza, I., “Design of wideband arrays with Archimedean Spiral Antennas,” Ph. D. Dissertation, SUPELEC, Gif-sur-Yvette, France, 2013.

Hinostroza, I., Guinvarc'h, R., Haupt, R. L. and Louertani, K., “A dual-polarized Wideband Planar Phased Array with Spiral Antennas,” *IEEE Transactions on Antennas and Propagation*, vol. 62, no. 9, pp. 4547-4553, June 2014.

Hinostroza, I., Guinvarc'h, R., Haupt, R. L. and Louertani, K., “A 6:1 Bandwidth, Low-Profile, Dual-Polarized Ring Array of Spiral Antennas with Connecting Arms,” *IEEE Transactions on Antennas and Propagation*, vol. 64, no. 2, pp. 752-756, February 2016.

Huang, J., “A technique for an array to generate circular polarization with linearly polarized elements,” *IEEE Transactions on Antennas and Propagation*, vol. 34, no. 9, pp. 1113-1124, September 1986.

Louertani, K., Guinvarc'h, R., Ribière_Tharaud, N. and Hélier, M., "Study of the Radiated Polarization of an Antenna Array with Circular Geometry," *Progress In Electromagnetics Research C*, vol. 24, pp. 173-183, 2011.

Shively, D. G. and Stutzman, W. L., "Wideband arrays with variable element sizes," *IEE Proceedings H – Microwaves, Antennas and Propagation*, vol. 137, no. 4, pp. 238-240, August 1990.

Chapter 3: Planar Array of Connecting Spirals

3.1. Introduction

As we have observed in chapter 2, a non-uniform concentric ring has a low surface efficiency, which translates to a low realized gain. In order to obtain higher gains it is interesting to efficiently occupy the available space. One way of doing so is using uniform arrays, as long as the spacing is tight enough to avoid grating lobes. Using such an approach implies that the highest operating frequency depends on the distance between elements.

We know from (*Guinvarc'h et al., 2012*) and (*Hinostroza et al., 2016*) that adding connections between spirals allow for lower reflection coefficients in the lower frequencies. A constant issue that has been encountered is that the connections between spirals is made between spirals of opposite polarizations, thus the distance between elements becomes effectively larger and reduces the useful bandwidth due to grating lobes appearing in lower frequencies. The use of non-uniform arrays in (*Hinostroza et al., 2014*) has provided a way around this issue.

The idea behind the design presented in this section is to explore the possibility of connecting spirals of the same polarization, thus allowing for the elements to be placed closer together. This way we can avoid the use of non-uniform arrays while also obtaining a large bandwidth due to the connections between elements.

In this design the dual polarization is implemented by using both the mode 1 and the mode -1 spiral excitations.

3.2. Connecting Spirals

As a first step we will show a few infinite array simulations of connecting spirals with different numbers of arms to observe the behavior of the reflection coefficient compared to non-connected spirals. As we are interested in planar uniform arrays we will analyze infinite arrays of connecting spirals with 3 arms, 4 arms and 6 arms. FEKO implements infinite periodic boundaries (PBC) to calculate the active reflection coefficient, where mutual coupling is effectively taken into account, and the embedded element pattern (*Example Guide FEKO*).

Starting with the 3-arm spirals (Fig. 3. 1), we observe that the reflection coefficient has a stable value around -5 dB when the isolated spiral reflection coefficient is close to 0 dB. However, this design is not ideal as a -5 dB reflection coefficient is too high and, in order to feed the spirals, you need to produce phases of 0°, 120° and 240° (*Rahman et al., 2017*), which is difficult.

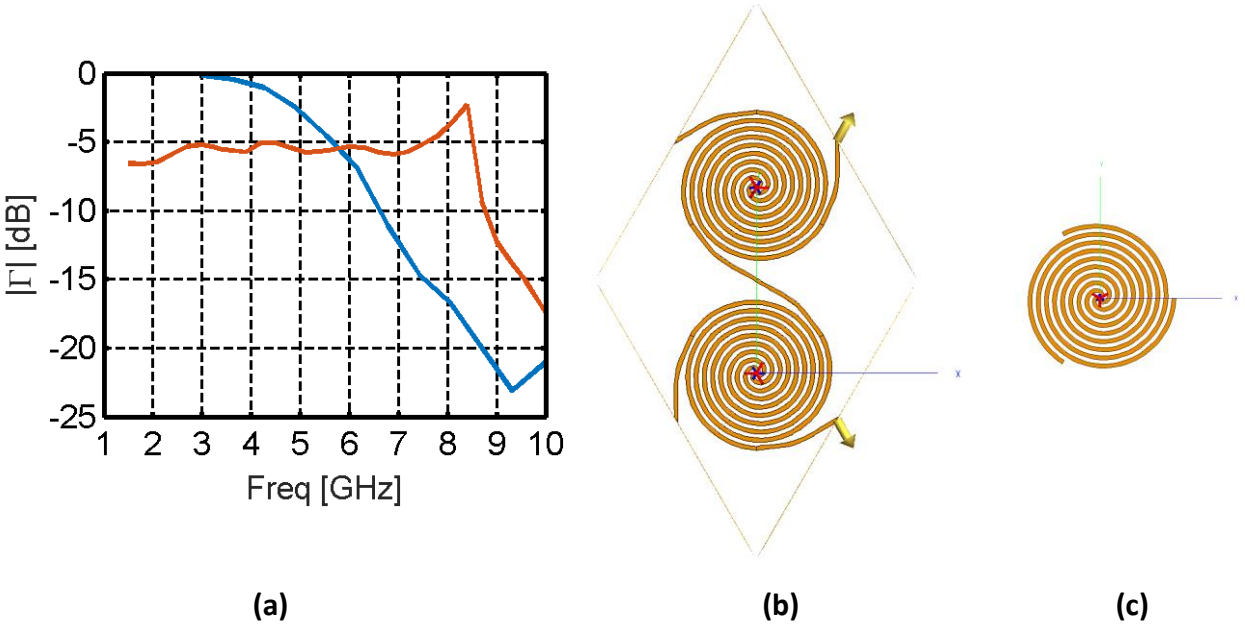

Fig. 3. 1 Reflection coefficient from FEKO simulation of a 3-arms connecting spirals infinite array (geometry in (b), red curve) and of a single 3 arms spiral (geometry in (c), blue curve) using FEKO. The spirals have radius equal to 1 cm and the spacing between neighboring spirals in the array is 2.33 cm.

We next compare the reflection coefficient of an isolated spiral with that of the 4-arm connecting spiral array (Fig. 3. 2). The reflection coefficient was obtained from a FEKO simulation using periodic boundaries. In the case of 4 arms connecting spirals the interest in connecting spirals is a lot clearer. The reflection coefficient is kept below -10 dB for very low frequencies. This configuration is also interesting because the phase necessary to feed are multiples of 90°, thus readily available.

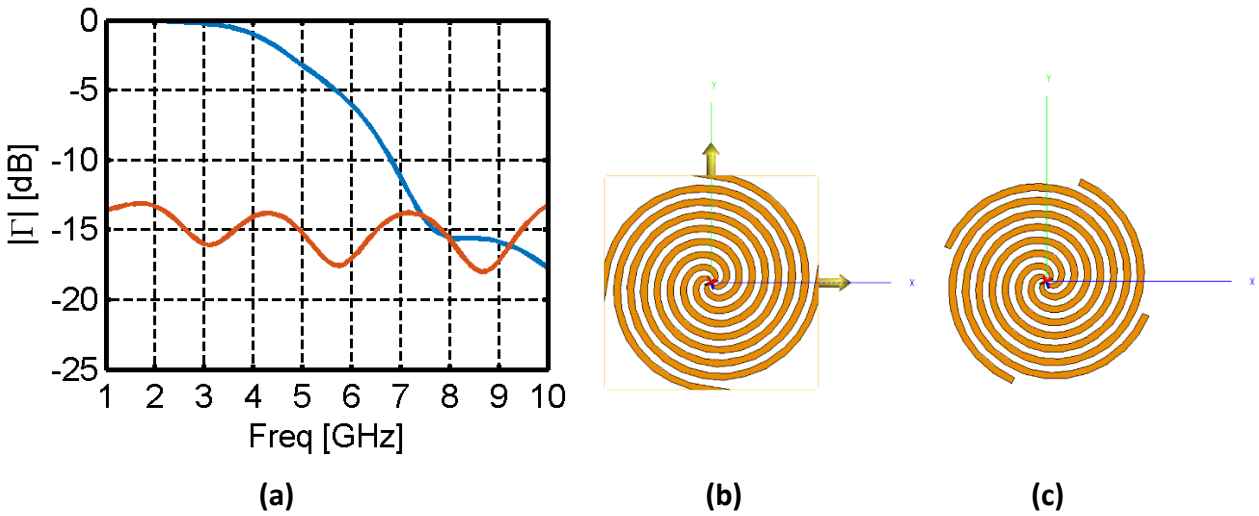

Fig. 3. 2 Reflection coefficient from FEKO simulation of a 4-arms connecting spirals infinite array (geometry in (b), red curve) and of a single 4 arms spiral (geometry in (c), blue curve) using FEKO. The spirals have a radius equal to 1 cm and the spacing between neighboring spirals in the array is 2 cm.

As a final example we will observe the case of 6-arm spirals. When simulating the array of 6-arm connecting spirals we observed resonances in the reflection coefficient (dash-dotted red line Fig. 3. 3). In order to verify if those consisted of numerical resonances, we added a few very small resistances (<1 ohm) in the arms of the 6 arms spirals, because adding asymmetry is a known way to avoid spiral resonances (*Steyskal et al., 2005*). By simulating the asymmetrical array we observe that the reflection coefficient stays under -10 dB for very low frequencies. Still, this design has the flaw of demanding feeding phases that are multiples of 60°, which are not readily available.

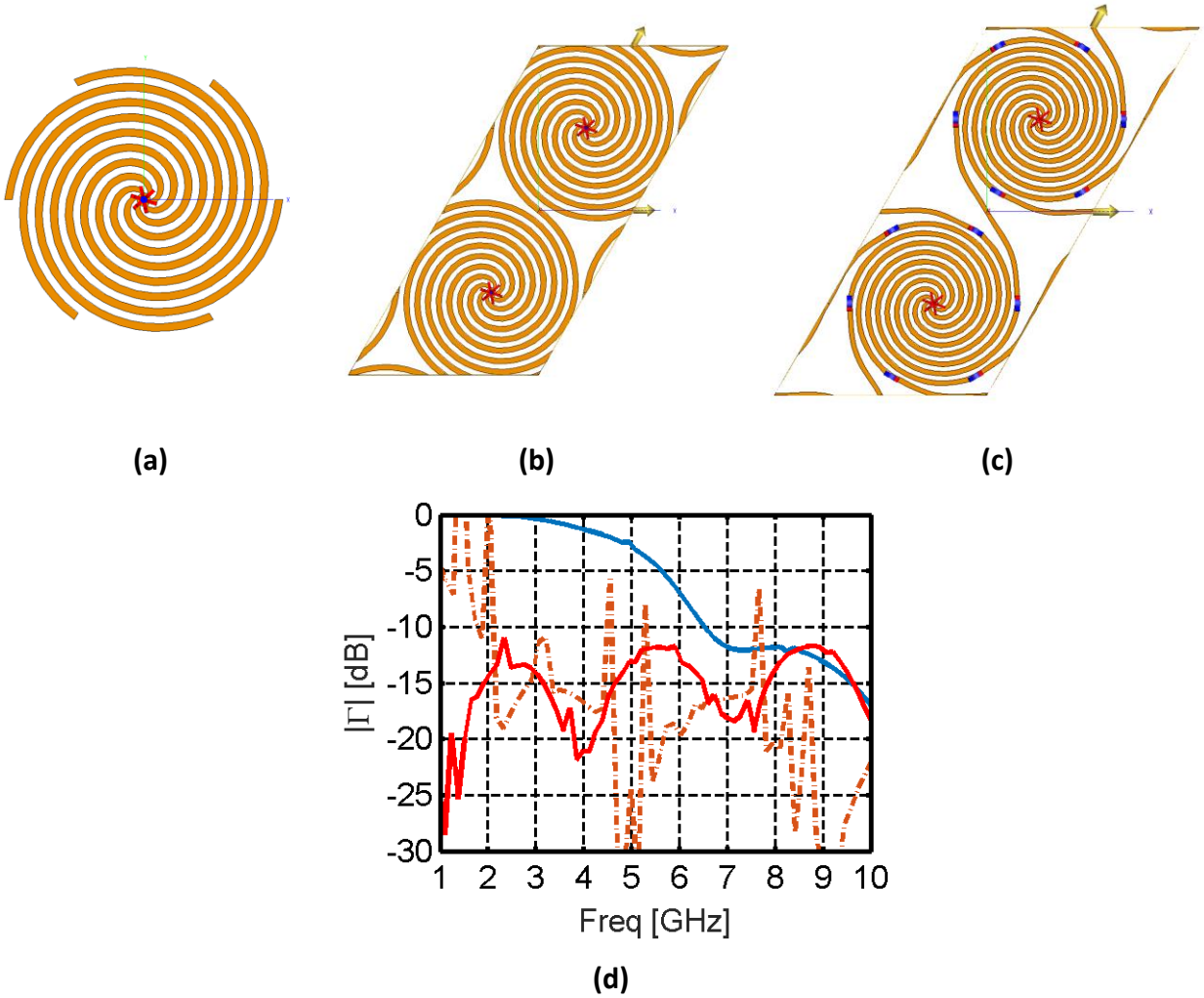

Fig. 3. 3 Reflection coefficient from FEKO simulation of a 6-arms connecting spirals infinite array with (geometry in (c), dashed red curve) and without (geometry in (b), red curve) small resistances in the arms to break resonances and of a single 6 arms spiral (geometry in (a), blue curve) using FEKO. The spirals have a radius equal to 1 cm and the spacing between neighboring spirals in the arrays is 2 cm for that without resistances and 2.5 cm for the one with resistances.

Observing the different options we chose to continue the analysis for the 4 arms spirals only, as they have shown the best behavior in simulation as well as having a reasonably simple feeding scheme, which will be interesting for prototyping later.

3.3. 4-Arm Connected Spirals

Having focused the study to the 4 arms connecting spiral array we will start by looking at the characteristics of the infinite array while comparing with the unconnected array. We will add the infinite unconnected array to the analysis to have a better base of comparison.

The spirals have a 2.4 cm radius and 2 turns.

The unconnected spirals will have the same dimensions as the connected one but with arms a little shorter, so that they will not touch the neighboring spirals, and the isolated spirals will be the same as the one from the disconnected array (Fig. 3. 4).

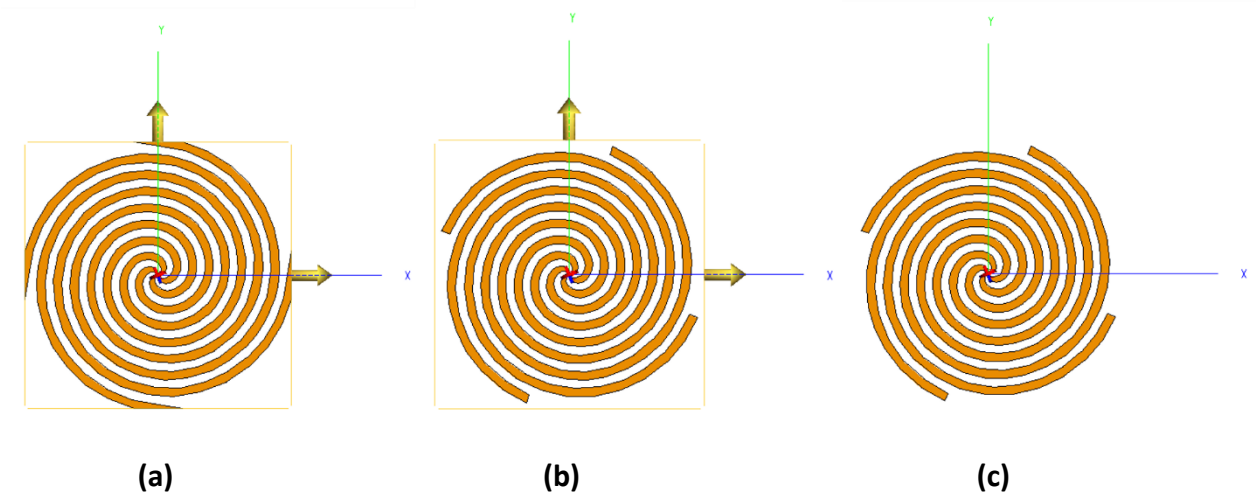

Fig. 3. 4 FEKO models of, from the left to the right, 4-arms connecting spirals infinite array (a), 4 arms disconnected spirals infinite array (b) and single 4 arms spiral (c). The spirals have a radius equal to 2.4 cm.

We will start by looking at the reflection coefficient as well as the realized gain and the axial ratio, first from the principal (mode 1) polarization, then for the secondary polarization (mode -1) (Fig. 3. 5). The gain is shown for a single cell of the periodic boundaries FEKO simulation.

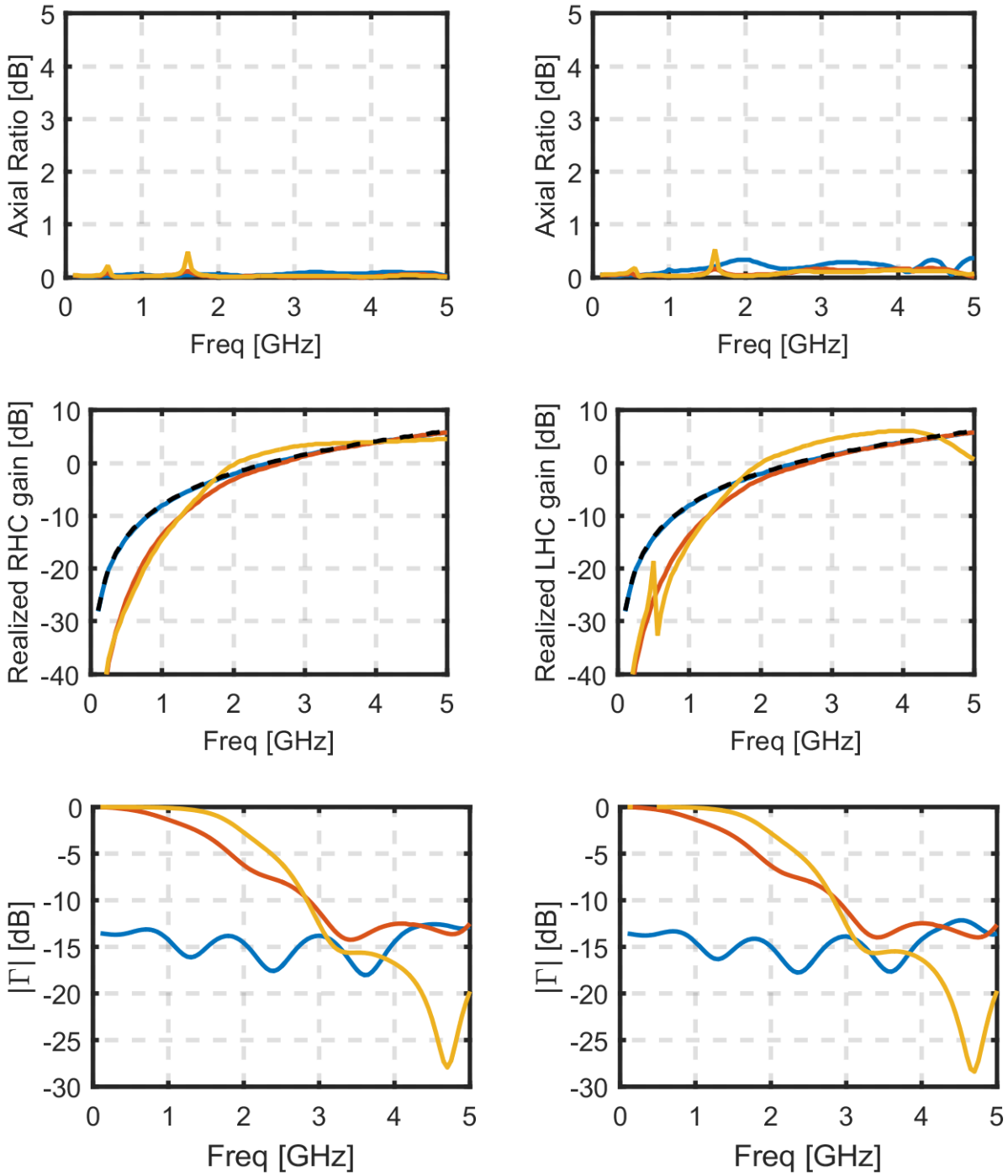

Fig. 3. 5 FEKO simulation of the 4-arms connecting spirals infinite array (blue), 4 arms disconnected spirals infinite array (red) and single 4 arms spiral (yellow). Main polarization (mode 1) on the curves to the left and secondary polarization (mode -1) on the curves to the right. In dashed black we have the maximal surface gain corresponding to the regions enclosed by the periodic boundaries, subtracting 3 dB as the antennas radiates to both sides.

In the array of spirals as well as for the isolated spiral the reflection coefficient is larger than -10 dB for frequencies smaller than 2.85 GHz, while the array of connecting spirals has a reflection coefficient smaller than -10 dB over the whole simulated bandwidth. As for the realized gain, it

follows the maximal theoretical gain for the connected array as well, discounting 3 dB due to radiating to both +z and -z. The axial ratio is also very low for all frequencies.

3.3.1. Finite Array Analysis

The natural next step in the analysis of the array is to observe its behavior with a finite number of elements. We will start of by analyzing a 5x5 array with 3x3 active elements and one layer of elements matched by 290 Ω resistances (Fig. 3. 6). The results of the FEKO simulations can be seen in Fig. 3. 7 and in Fig. 3. 8. The array was simulated with FEKO to obtain the S parameters, which were used to recompose the active reflection coefficient (Fig. 3. 8). We can observe that the reflection coefficient of the finite array has a reasonable agreement with the one from the infinite array simulation. We can also observe that the simulation from the 7x7 array (5x5 active elements with one layer of matched elements) agrees to the infinite simulation until lower frequencies than the smaller one.

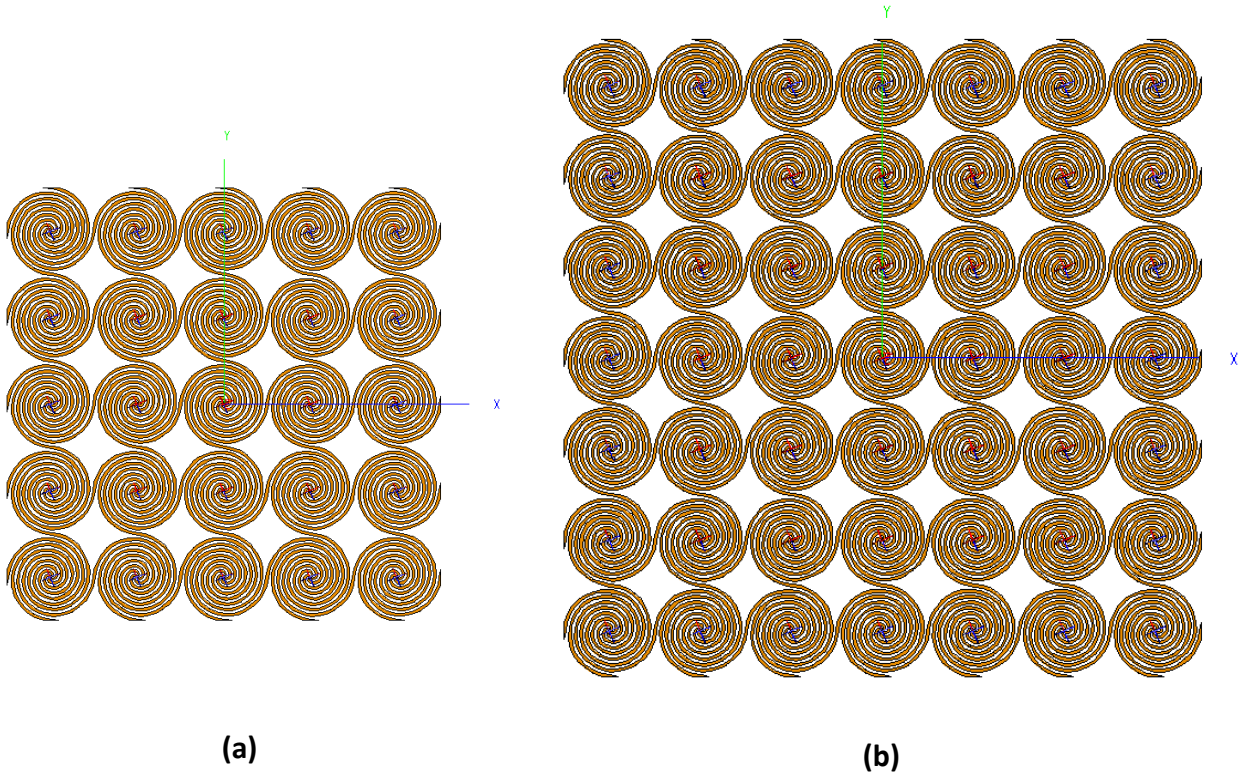

Fig. 3. 6 FEKO models of the 3x3 (a) and 5x5 (b) 4-arms connecting spiral arrays, both with one layer of elements with matching resistances of 290 Ω.

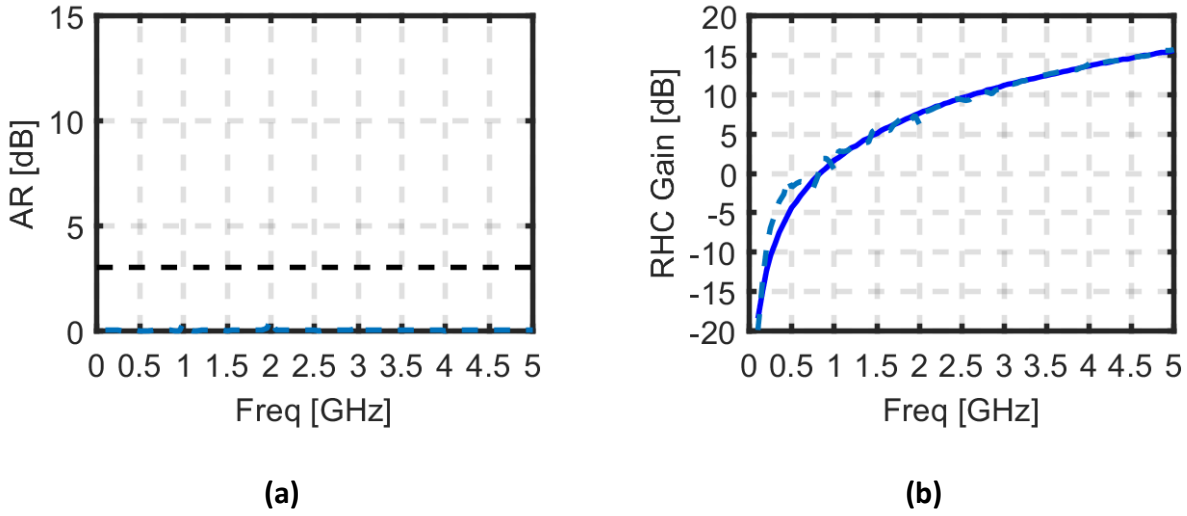

Fig. 3. 7 FEKO simulation of the 3x3 (dash-dotted blue) 4-arms connecting spiral arrays with one layer of elements with matching resistances of 290 Ω. In (a) we show the AR of the finite array and in (b) the RHC gain. The solid blue line in (b) comes from the 3x3 array of connected spirals using the embedded element pattern from the infinite simulation of the 4-arms connecting spirals infinite array for comparison.

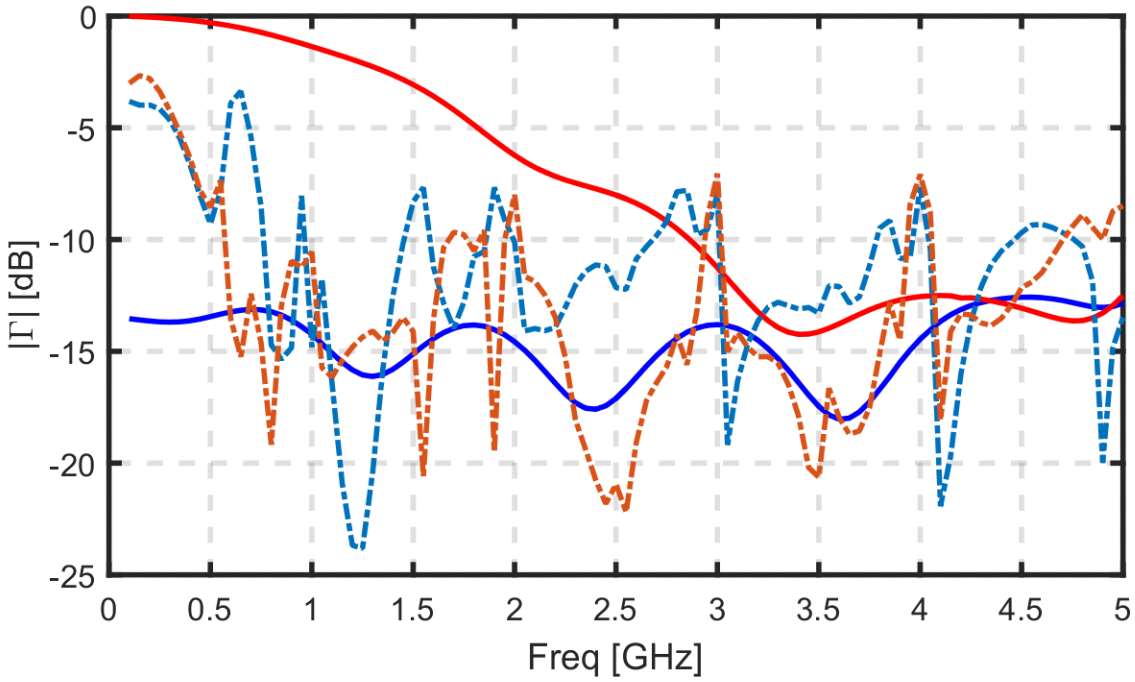

Fig. 3. 8 Reflection coefficient for the 3x3 (dash-dotted blue) and the 5x5 (dash-dotted red) 4-arms connecting spiral arrays, one layer of elements with matching resistances of 290 Ω. The reflection coefficient was calculate using the S parameters of the arrays, which were obtained from S parameter simulations using FEKO. We also have the reflection coefficient of the 4-arms connecting spirals infinite array (solid blue) and 4 arm disconnected spirals infinite array (solid red) for comparison.

3.3.2. Steering Behavior

We move on to observe the behavior of the infinite array of connecting spirals while steering to 30° (Fig. 3. 9, Fig. 3. 10 and Fig. 3. 11). The gain curves are calculated considering the embedded element pattern from the infinite simulation and using it in a 3x3 array.

We can see that resonances appear on the Axial Ratio of the disconnected array and of the connected array. However, the resonances are clearly higher on the connected array, and even more so in the mode -1 polarization (Fig. 3. 9).

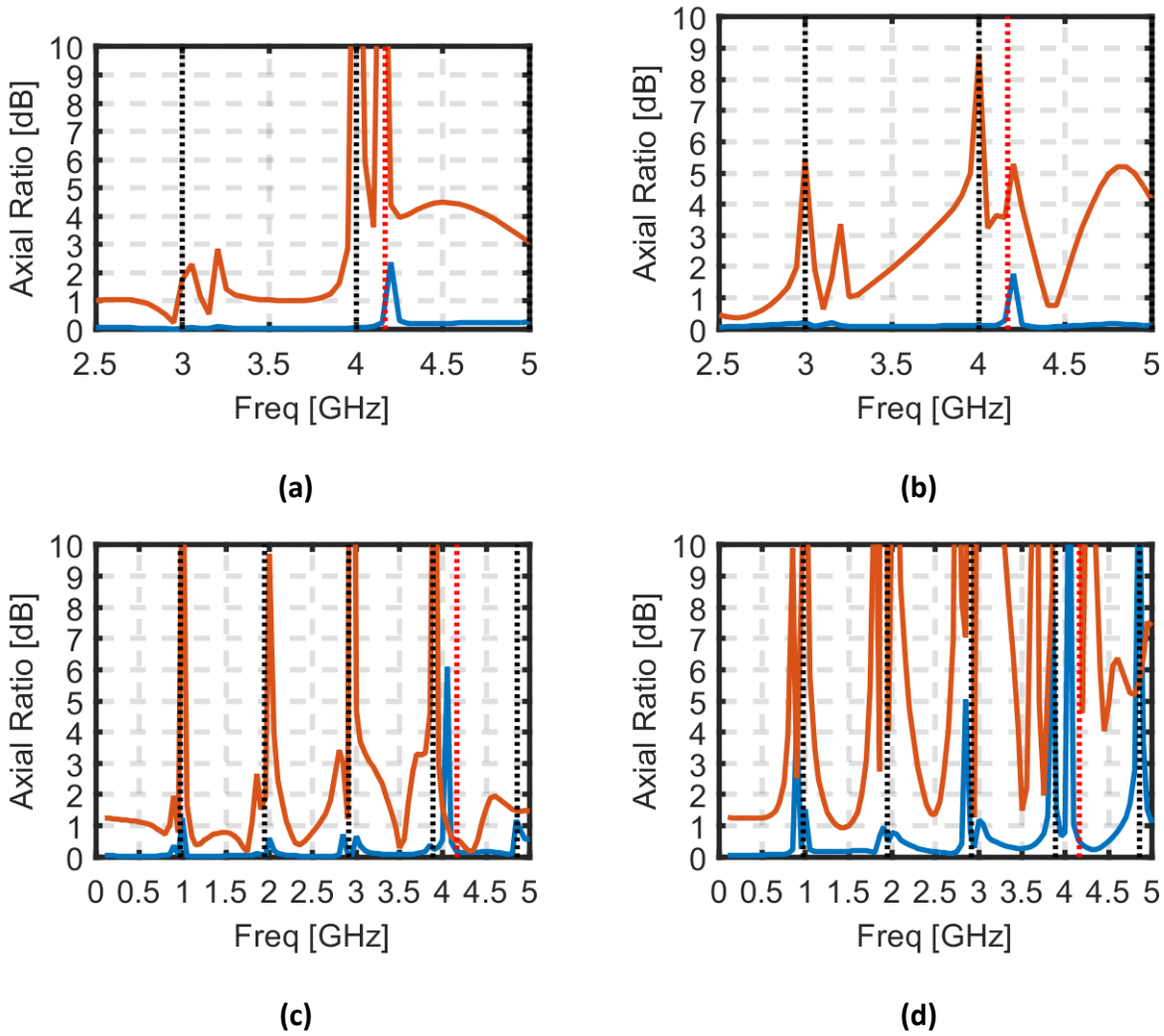

Fig. 3. 9 Axial Ratio of the 4 arm disconnected spirals infinite array in (a) and (b) and of the 4-arm connecting spirals infinite array in (c) and (d). In blue the array is steering to 5 degrees and in red to 30 degrees. In (a) and (c) we show the main polarization (mode 1) and in (b) and (d) we show the opposite polarization (mode -1). The black dotted vertical lines show the periodic spiral resonances and the red dotted vertical lines show the frequency in which the grating lobes appear when steering to 30°.

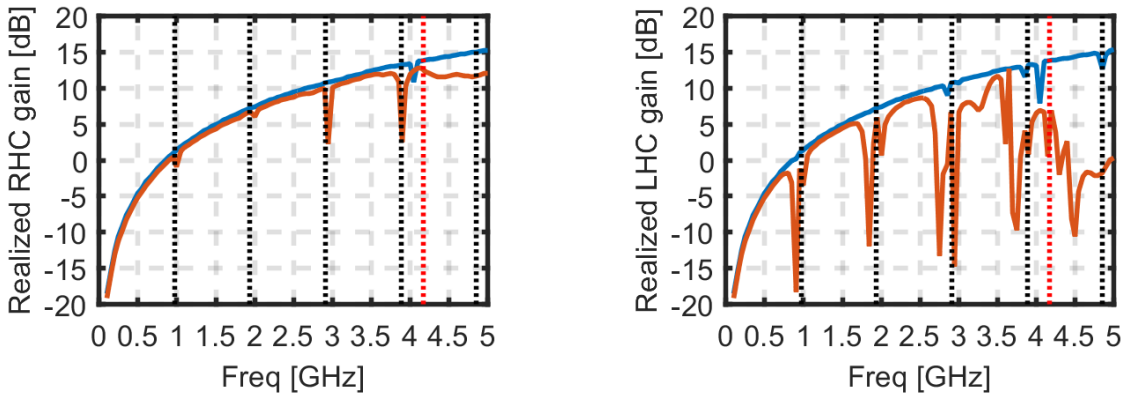

Fig. 3. 10 Realized Gain of the 4-arm connecting spirals infinite array. In blue the array is steering to 5 degrees and in red to 30 degrees. The curve to the left shows the main polarization (mode 1) and the curve to the right the opposite polarization (mode -1). The gain curves are traced considering the element pattern from the infinite simulation in FEKO in a 3x3 array. The black dotted vertical lines show the periodic spiral resonances and the red dotted vertical lines show the frequency in which the grating lobes appear when steering to 30°.

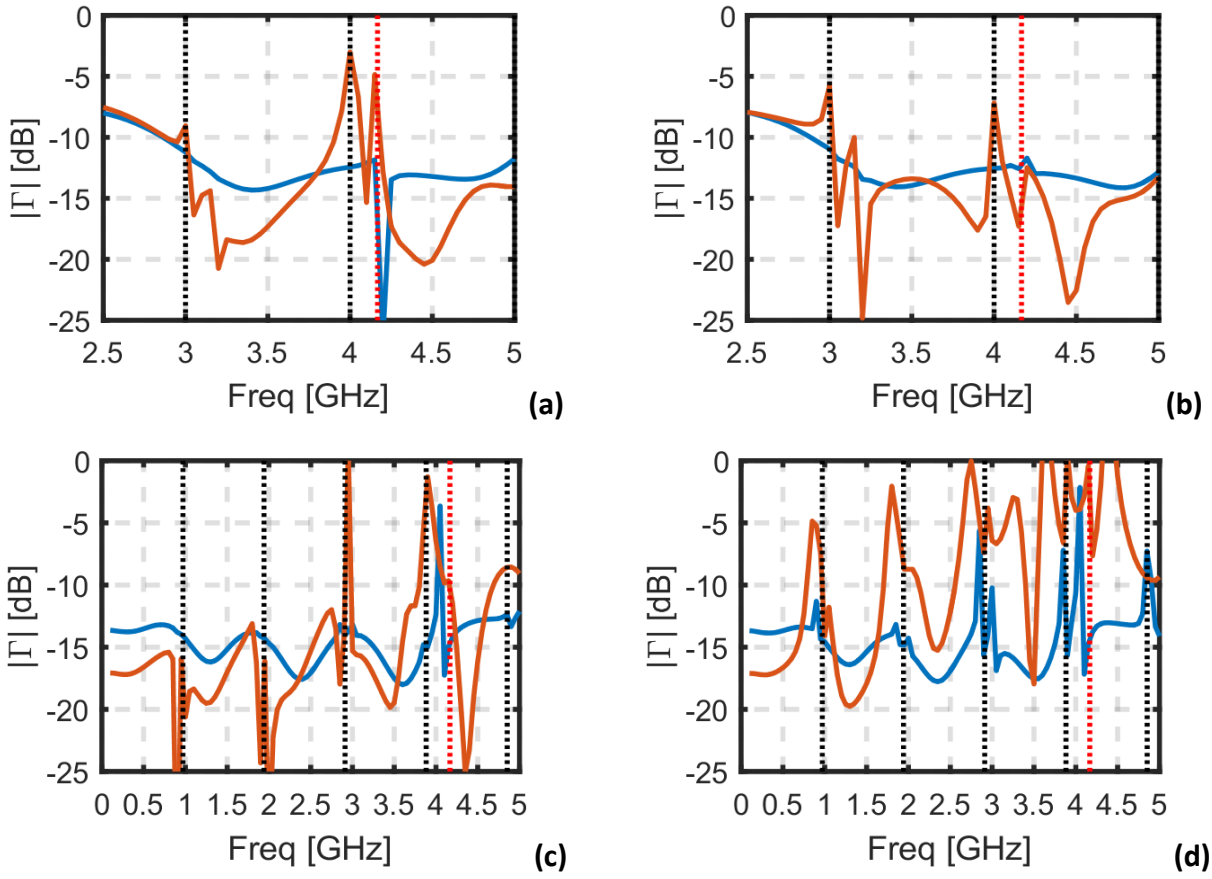

Fig. 3. 11 Reflection Coefficient of the 4 arm disconnected spirals infinite array in (a) and (b) and of the 4-arm connecting spirals infinite array in (c) and (d). In blue the array is steering to 5 degrees and in red to 30 degrees. In (a) and (c) we show the main polarization (mode 1), and in (b) and (d) we show the opposite polarization (mode -1). The black dotted vertical lines show the periodic spiral resonances and the red dotted vertical lines show the frequency in which the grating lobes appear when steering to 30°.

We can see that those resonances appear as well in the gain and in the reflection coefficient of the array, mostly on the mode -1 (Fig. 3. 10 and Fig. 3. 11).. When steering to 30°, some of the resonances around 4.16 GHz can be explained by the onset of grating lobes (the grating lobes appear at 4.16 GHz when steered to 30° and at 5.75 GHz when steered to 5°).

The resonances appear at frequencies that are multiples of 0.97 GHz for the connected array (Fig. 3. 9 (c) and (d), Fig. 3. 10 and Fig. 3. 11 (c) and (d)) and as multiples of 1 GHz for the disconnected array (Fig. 3. 9 (a) and (b) and Fig. 3. 11 (a) and (b)), and they get higher as we steer further away from broadside. It is important to point out that the length of the spiral arms is 15.45 cm in the connected array, which corresponds to $\lambda/2$ at 0.97 GHz, and equal to 15 cm for the disconnected array ($\lambda/2$ at 1 GHz). Thus, the resonances are probably linked to spiral resonances, as expected from (*Steyskal et al., 2005*).

It would be important to further analyze the steering behavior of the connected spirals array to understand those resonances and how to avoid them. We did not have the time to treat this problem due to time constraints.

3.3.3. Ground Plane Effect

For the sake of completeness, we will show a few infinite simulations with a ground plane. In Fig. 3. 12 we compare the infinite simulations without a ground plane and with ground planes at 2 cm, 4 cm and 6 cm height. There is no substrate between the elements and the ground plane in the simulations.

Here we encounter the typical problems of backing planes on wide bandwidth antennas. At low frequencies the ground plane short circuits with the antenna itself, making for a large reflection coefficient. At high frequencies the ground plane height eventually equals $\lambda/2$, causing a large reflection coefficient as well. The frequency at which we observe both effects is inversely proportional to the height of the ground plane (e.g. a larger height makes the short circuit between the ground plane and the antenna appear at lower frequencies and the point at which the height is equal to $\lambda/2$ is also at a lower frequency).

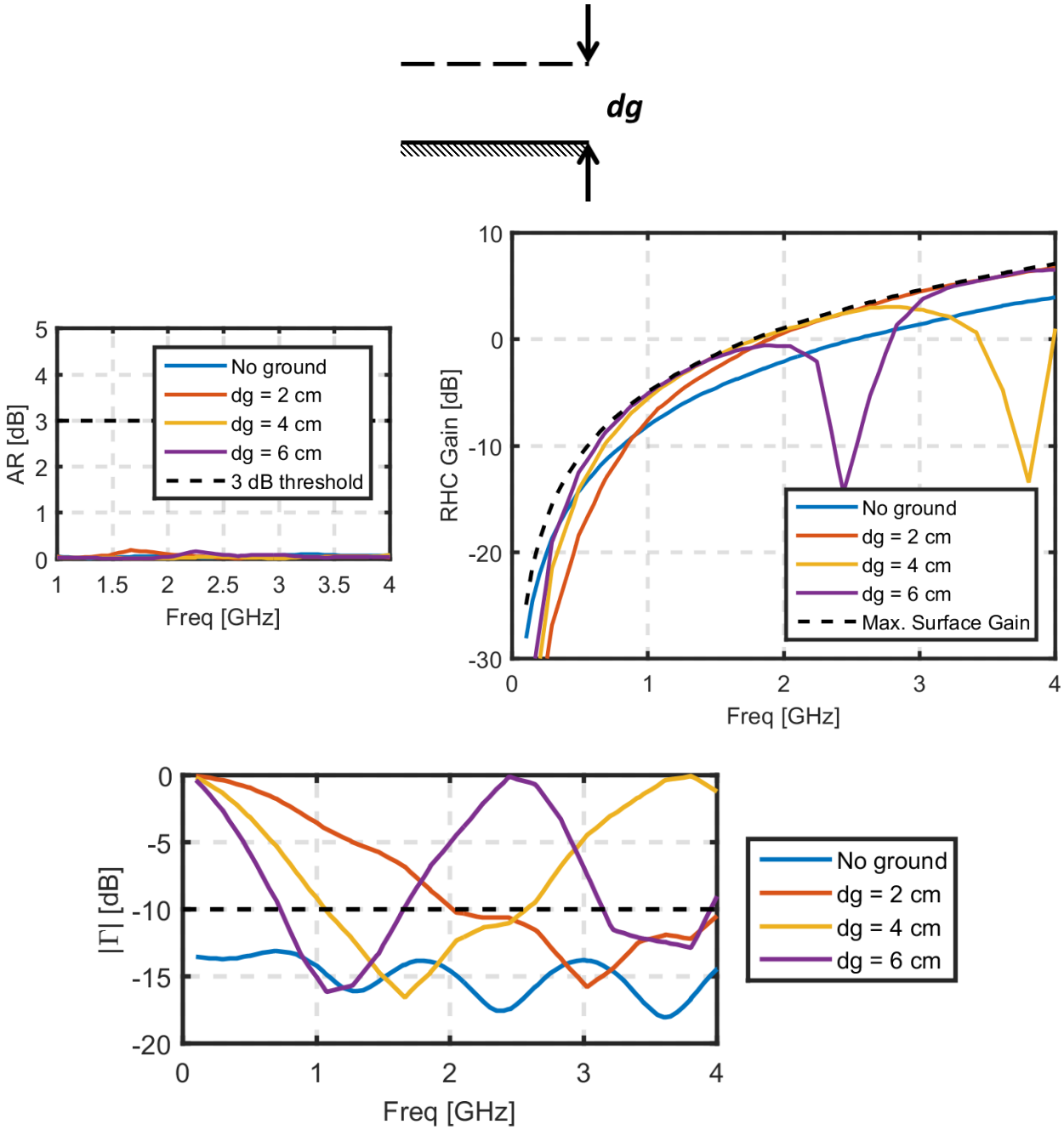

Fig. 3. 12 Axial Ratio, RHC Gain and Reflection coefficient obtained from infinite array simulations of a 4 arm connecting spiral array using FEKO. In blue there is no ground plane, in red there is a ground plane 2 cm away from the spirals, in yellow 4 cm away and in purple 6 cm away.

3.4. Prototype

In order to build a prototype and validate the simulations, a few adjustments had to be made to the design. The first important issue is the input impedance of the antennas. The impedance

between opposing arms of a self-complementary 4-arm spiral in free space is 290 Ω (Fig. 3. 13 and Fig. 3. 17) (theoretical value is 266 Ω for mode m=1 in an n=4 fold self-complementary structure c.f. equation (28) in (*Deschamps, 1959*)).

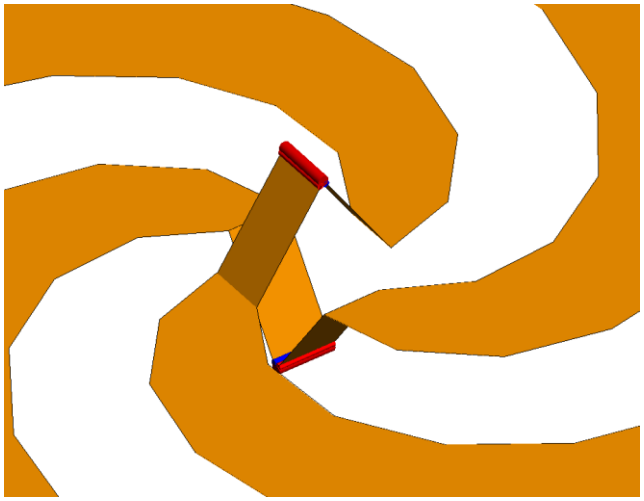

Fig. 3. 13 Feed of the simulated self-complementary 4-arms connecting spirals in FEKO.

One strategy to obtain a simple balun is to use 180° hybrid couplers (*McFadden, 2007*). We can use the configuration from Fig. 3. 14, and feed the antenna with 4 coaxial cables, 2 for each couple of opposing arms of the spirals. The 90° phase between the two pairs of opposing arms is produced by a 90° hybrid coupler (Fig. 3. 15).

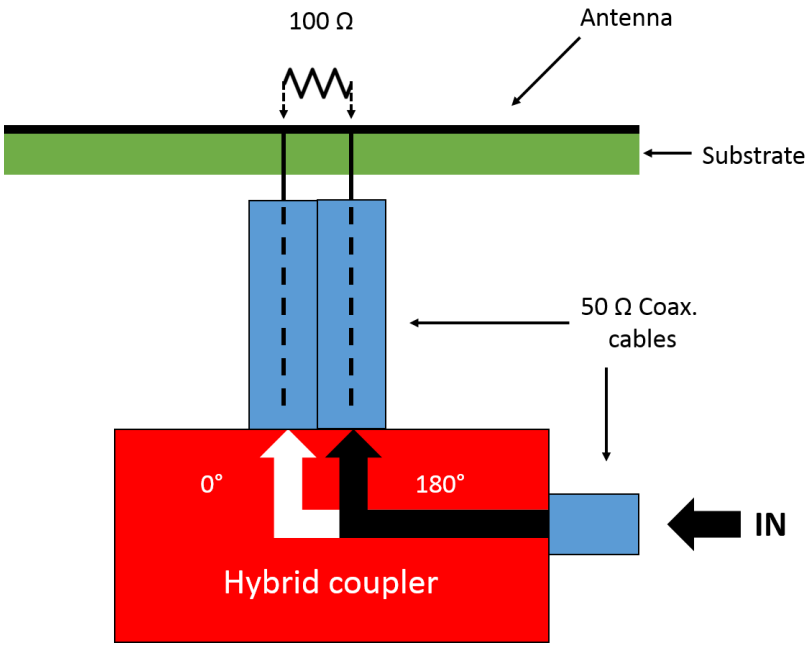

Fig. 3. 14 A simple balun with an impedance transformation from 100 Ω to 50 Ω using a hybrid coupler.

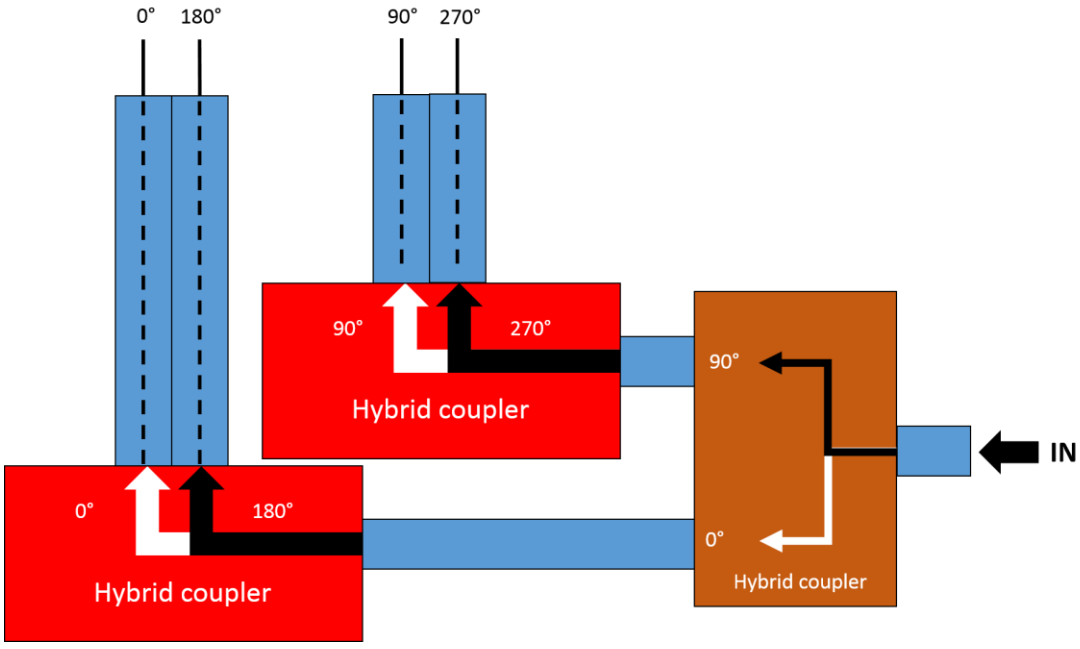

Fig. 3. 15 Connection scheme using 90° and 180 ° hybrid couplers to obtain 0°, 90°, 180° and 270° phases for a balanced feed for a 4-arm spiral antenna.

So, in order to avoid having to design a balun, we need to reduce the impedance between opposing arms of the spiral to around 100 Ω. The solution we chose to reduce the input impedance of the spiral arms was to use a non-complementary spiral (*Huffman, 2005*) over a 1.6 mm thick RO4350B substrate, $\varepsilon_r = 3.66$, (Fig. 3. 16). Each of the spiral arms occupy 81°. We can observe that the impedance is effectively reduced in this design in Fig. 3. 17.

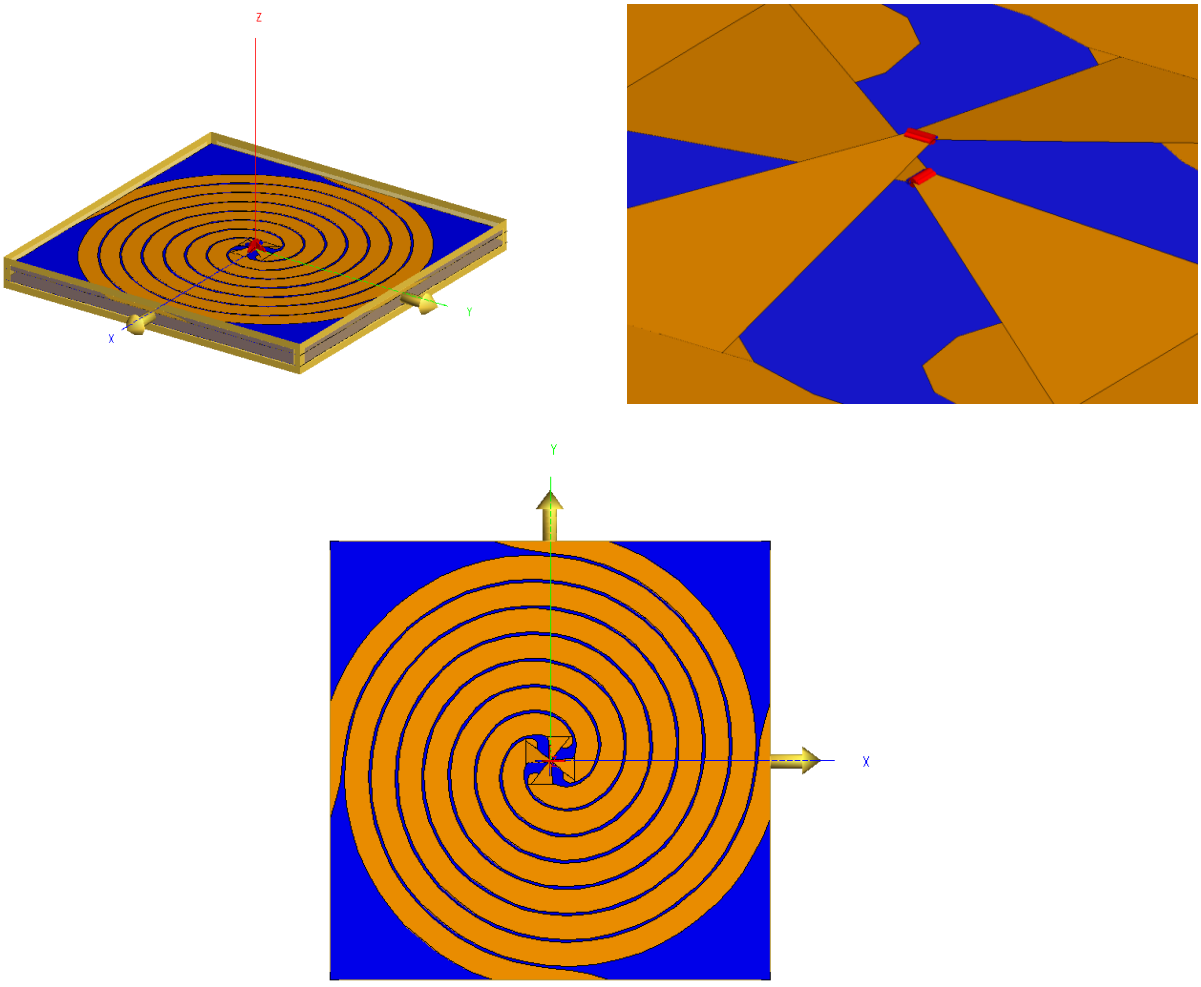

Fig. 3. 16 Unitary cell of the infinite array of non-complementary 4-arms connecting spirals over a RO4350B substrate, $\varepsilon_r = 3.66$.

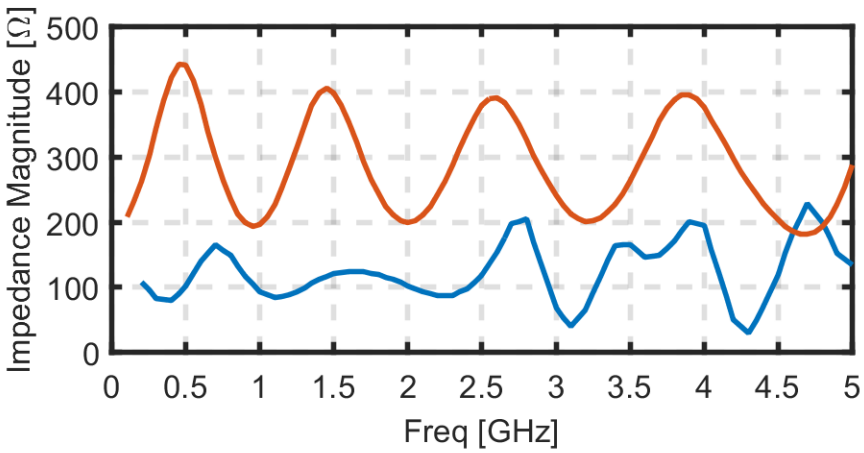

Fig. 3. 17 Simulated impedance (magnitude) from the simulated infinite array of self-complementary spirals in free space (red) and non-complementary spirals with substrate RO4350B, $\varepsilon_r = 3.66$ (blue).

The final prototype consists of a 5x5 array of connecting spirals. The spirals have a radius of 2.4 cm and are 4.8 cm apart from each other, with the arms connected. The array is centered in a RO4350B substrate, $\varepsilon_r = 3.66$, with dimensions of 30 cm x 30 cm x 1.6 mm (Fig. 3. 18).

A hole of 1 mm was made in each of the spiral arms at the feeds so we could solder the coaxial cables and the resistors. The inner 3x3 array had 25 cm long coaxial cables (Teflon dielectric, impedance 50 Ω, inner conductor with 0.94 mm diameter, dielectric with 2.92 mm diameter and outer conductor with 3.55 mm diameter) soldered to each of the spiral arms. The outer spirals in the array had resistances of 100 Ω nominal value soldered in between opposing arms (Fig. 3. 18).

Thus, for each of the spiral antennas there is a group of 4 soldered coaxial cables. The coaxial cable groups were attached together using copper tapes from the feeding level until 16 cm away from the spirals feed (Fig. 3. 18).

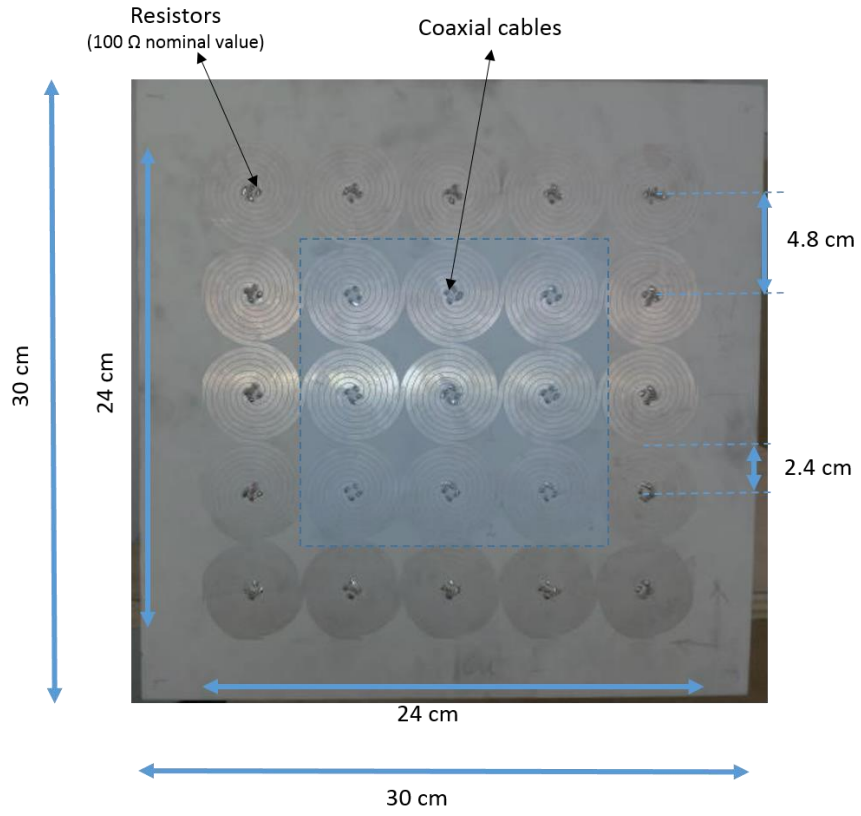

(a)

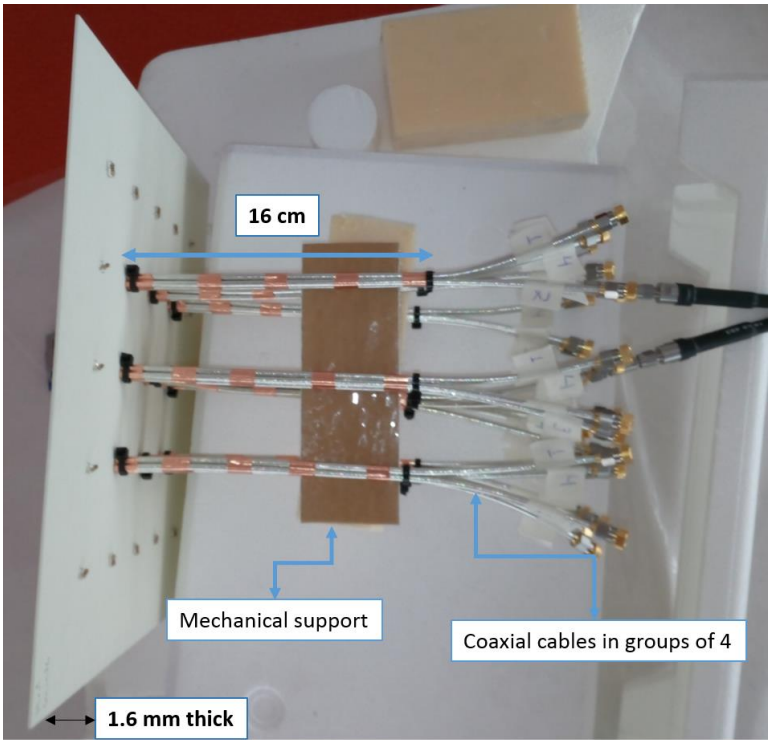

(b)

Fig. 3. 18 Photos of the prototype 4-arm connecting spirals array. In (a) we have the front view with the elements with soldered coaxial cables highlighted in blue and the dimensions indicated. In (b) we have the side view showing the soldered coaxial cables and the dimensions indicated as well.

3.4.1. Reflection Coefficient Measurement of the prototype array

In order to measure the reflection coefficient we used a network analyzer to measure the S parameters S1X, where the port 1 is one of the ports of the central spiral in the array and X are all ports from the 3x3 array of spirals that have coaxial cables.

In order to avoid the effects of the longer cables connecting the VNA to the soldered cables we made a TSOC (Through, Short, Open, Charge) calibration of those longer cables, so the measurements only take into account the array and the cables soldered to the array.

Having all of those measurements, we computed the active reflection coefficient by summing the S parameters including the corresponding feeding phases (0°, 90°, 180° or 270° depending on the spiral arm to obtain mode 1 and mode -1 excitations). In Fig. 3. 21 we compare the simulated and measured recomposed reflection coefficients.

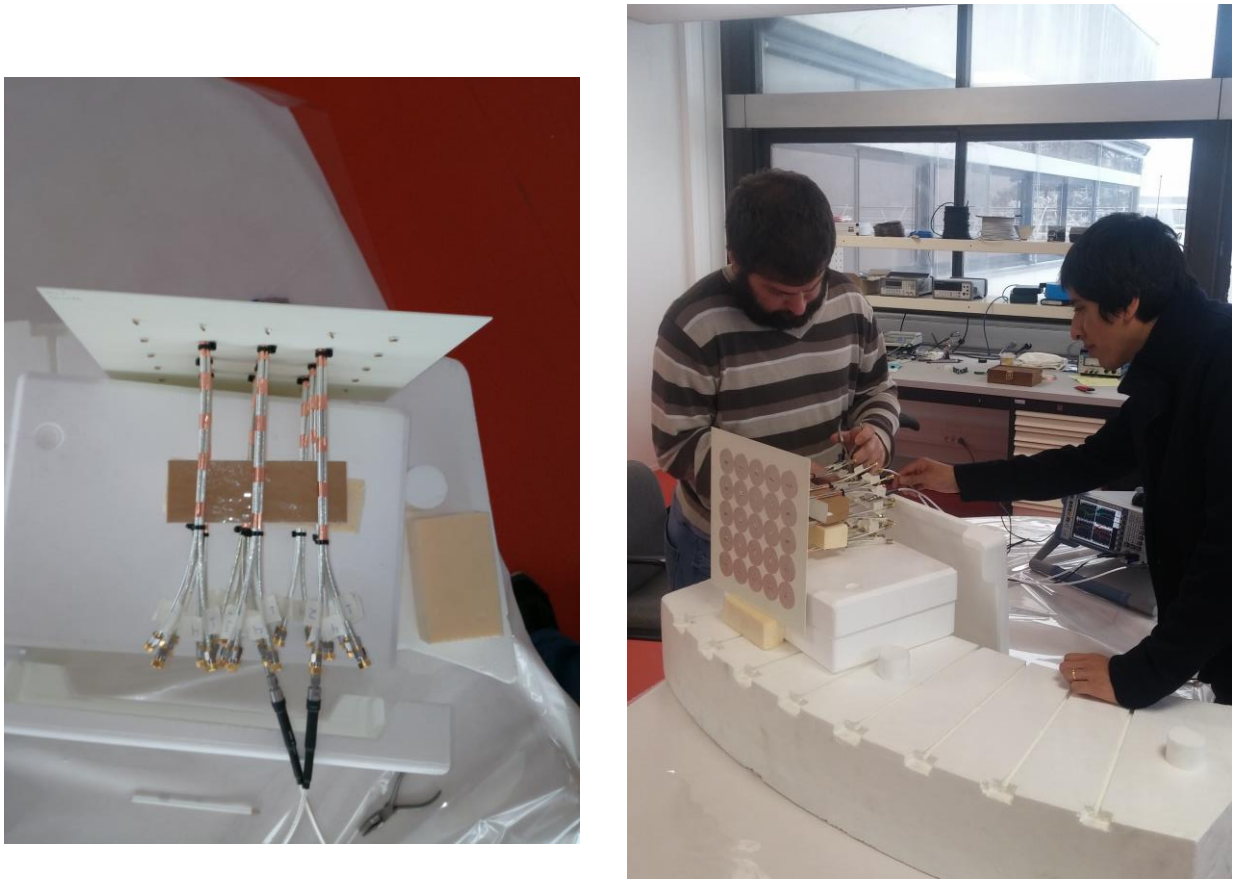

Fig. 3. 19 Measurement of the S parameters of the prototype array of 4 arms connecting non-complementary spirals.

For the simulation we used an infinite substrate, because the finite substrate simulation required too much memory (Fig. 3. 20). We found the S parameters and calculated the Reflection Coefficient in the same manner. Fig. 3. 21 shows that the reflection coefficient obtained from the measurements and from the simulated finite array have a good agreement to each other from 0.5 GHz onwards.

Moreover, from 1 GHz to 2 GHz, the results from the finite arrays, both simulated and measured, have similar trends compared with the results from the infinite simulation. It should be noted that the 9 active elements in the array (3x3 sub array) occupy a surface sized 14.4 cm x 14.4 cm, which gives about $\lambda/2$ x $\lambda/2$ at 1 GHz. For frequencies above 2 GHz they have a good agreement.

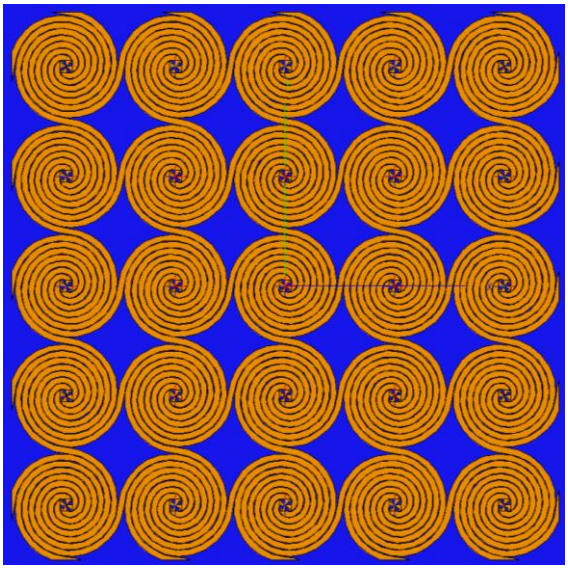

Fig. 3. 20 FEKO model of 4-arm connected spirals 5x5 array.

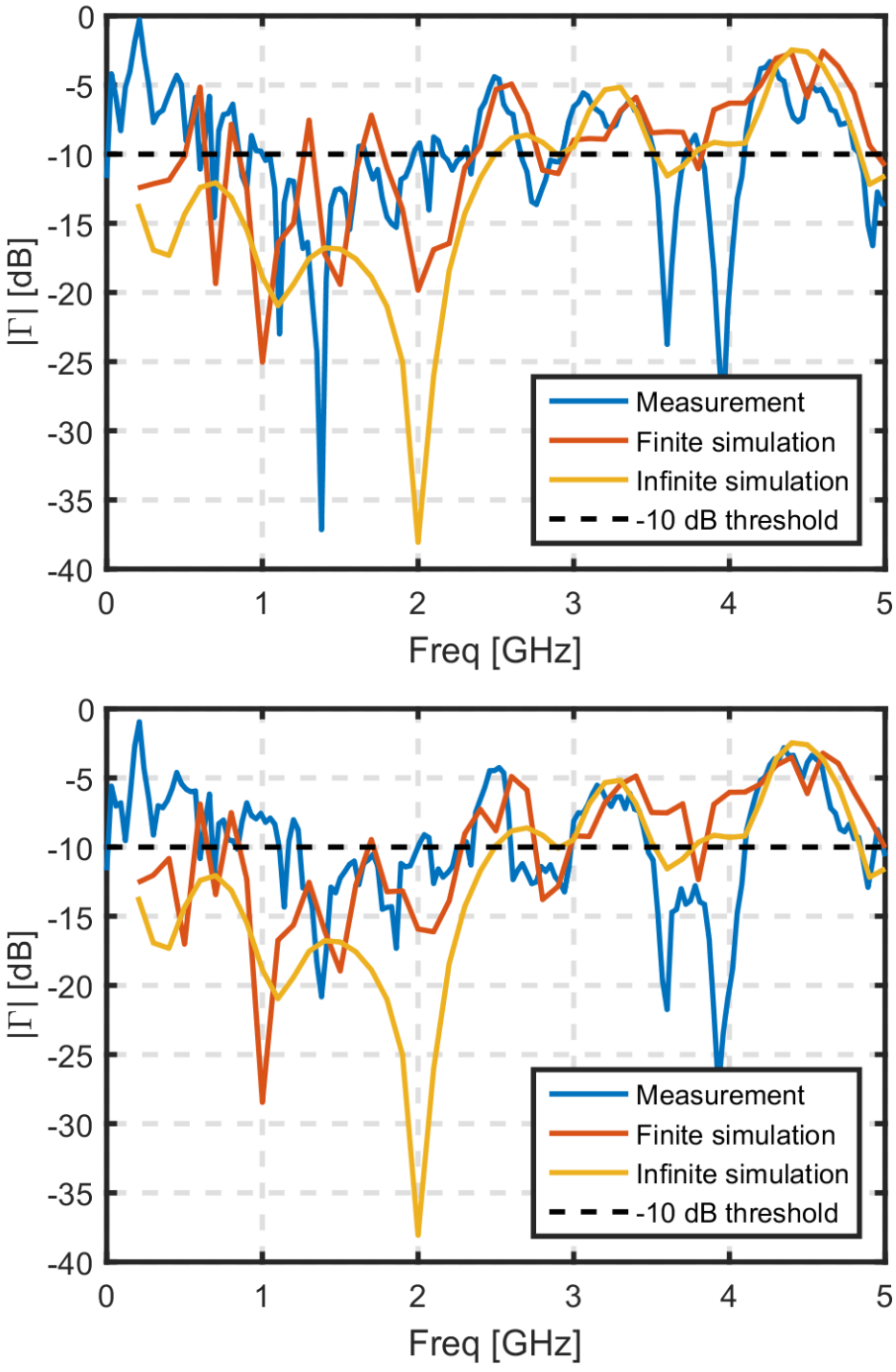

Fig. 3. 21 Reflection Coefficient from the prototype array (Fig. 3. 18), from the FEKO simulation of the 3x3 4-arm connecting non-complementary spirals array with one layer of elements with matching resistances of 100 Ω (Fig. 3. 20) and from the FEKO simulation of the infinite 4-arm connecting non-complementary spirals array. In (a) we have the RH polarized array (mode 1) and in (b) we have the LH polarized array (mode -1).

3.4.2. Gain and Electric Fields Measurements of the prototype array

Having validated the reflection coefficient simulations with measurements, we moved on to validate the gain and the electric fields radiated by the array.

Due to the measurement difficulty, only 3 antennas were fed: center, right below center and lower-right from center antenna. From Fig. 3. 22, it can be seen that the center antenna is numbered as 1, right below the center antenna there is the antenna numbered as 2, and lower-right from the center antenna there is the antenna numbered as 3.

The radiation from the other antenna elements were obtained by rotating and phasing the measured fields from the antennas numbered as 2 and 3 (Fig. 2. 56). Finally the total radiation was obtained by summing the fields of each of the antennas.

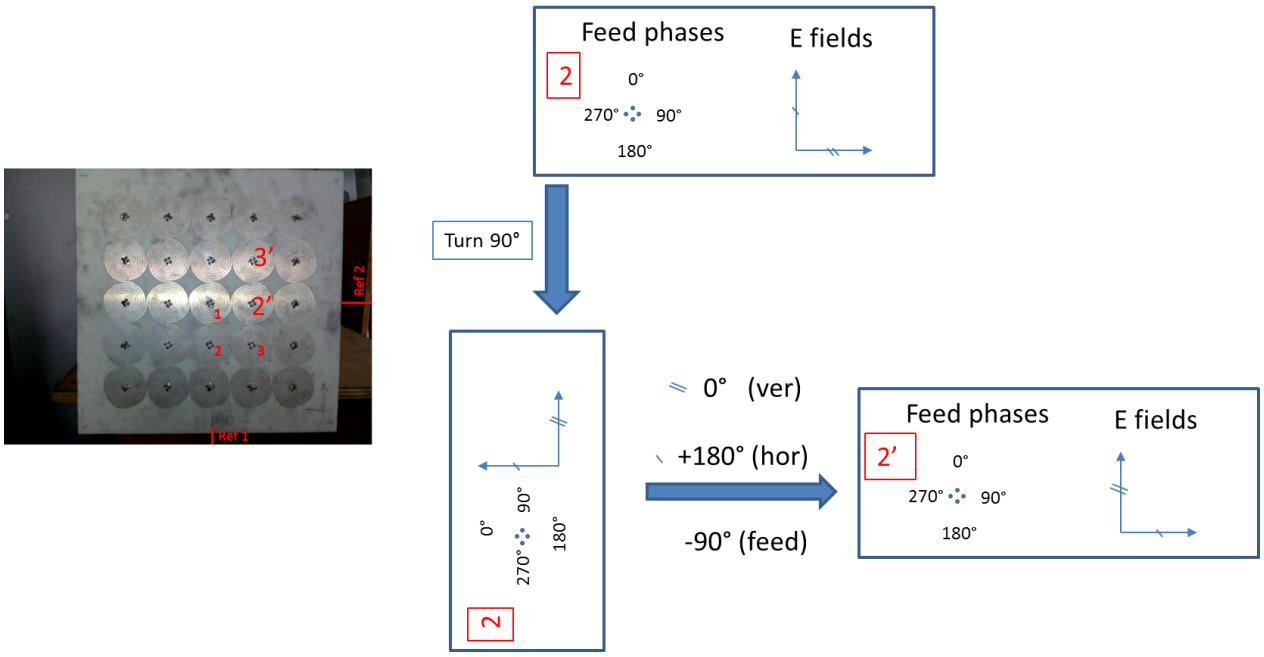

Fig. 2. 56 Scheme showing how to obtain the all the antennas radiation from the measured antennas thanks to the array symmetry. At first we have the antenna numbered 2 (3), and we rotate the fields by 90°. This way the originally vertical cut becomes the horizontal cut (one tick) and the originally horizontal cut becomes the vertical cut (two ticks). Finally, we take the negative of the horizontal cut (one tick) and we compensate the extra rotation on the feeding phases by adding a 90° phase to both cuts, resulting in 2' (3'). Subsequent rotations can provide the fields from the other antennas.

Two polarizations were considered: RH and LH. For that, each antenna was fed with two 180° hybrid couplers and one 90° hybrid coupler (Fig. 3. 14 and Fig. 3. 15). All terminations had matching loads.

The radiated fields of the 3 antennas were measured for the horizontal and vertical cuts. However the results are shown only for the horizontal cut. Because of the array's symmetry the vertical and horizontal cuts are supposed to be equal, but as we only measured the 3 numbered antennas we need both cuts in order to reconstruct the full array for any of the cuts.

In Fig. 3. 22 we can see the marks Ref 1 and Ref 2, which were used to align the axis of the array to the center of the rotating support used to perform the measurements of the different cuts (Fig. 3. 23 and Fig. 3. 24). The reference antenna was kept in place while the antenna under test (the prototype) was rotated. In our setup, when the array had the Ref 1 mark aligned to the rotating platform axis the measured cut was the horizontal one (phi=0°).

The reference antenna used was a horn S600 from Satimo and the measurements were conducted from 0.5 to 3 GHz. Since the manufacturer's stated gain of the reference antenna started at 600 MHz, and the antenna was not well adapted below that frequency, we retained measurement values from 0.6 up to 3 GHz. The distance between the reference antenna and the antenna under test (the prototype) was 4.3 m (Fig. 3. 24).

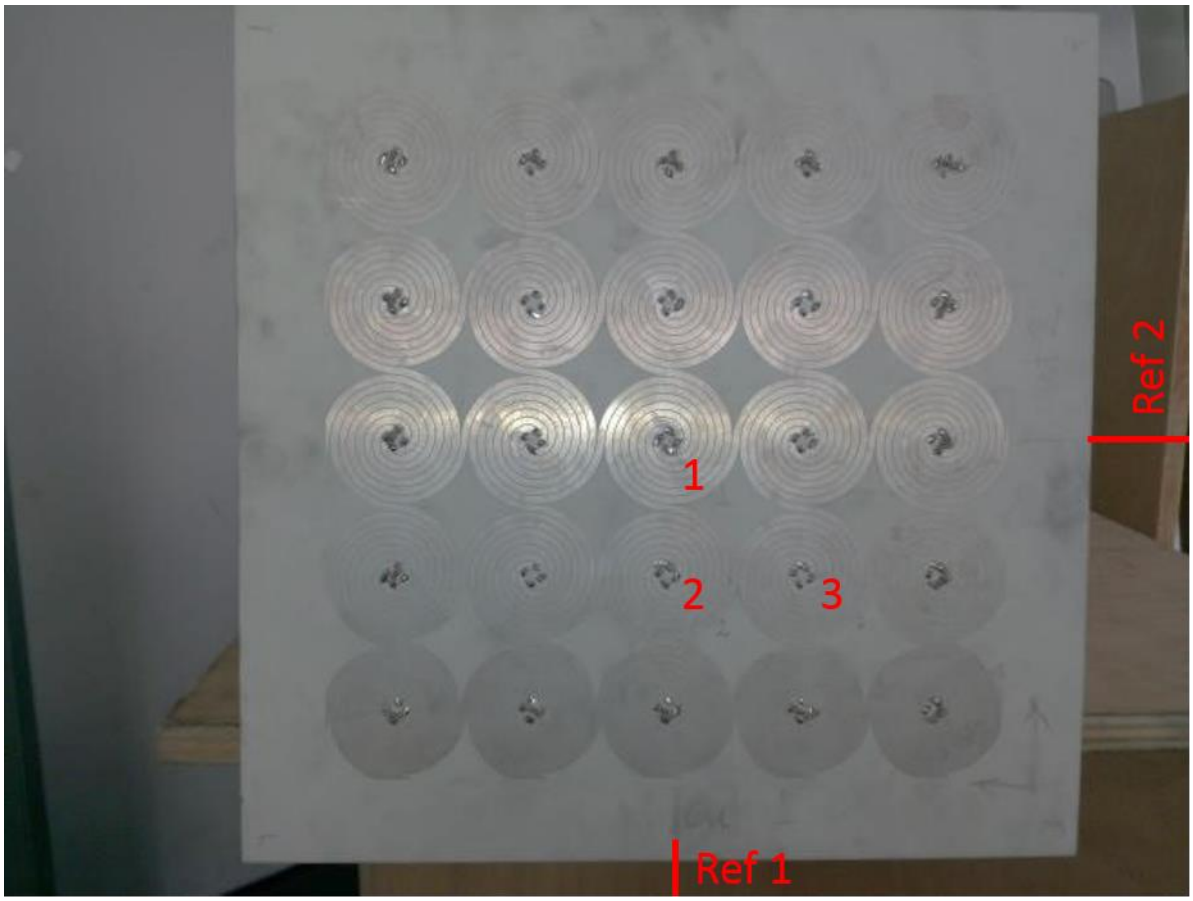

Fig. 3. 22 Antenna array Under Test. The marks Ref 1 and Ref 2 indicate that during the measurement (always the AUT is the one rotating, see Fig. 3. 24) the said Ref X is aligned to the base center marked in the support (Fig. 3. 23).

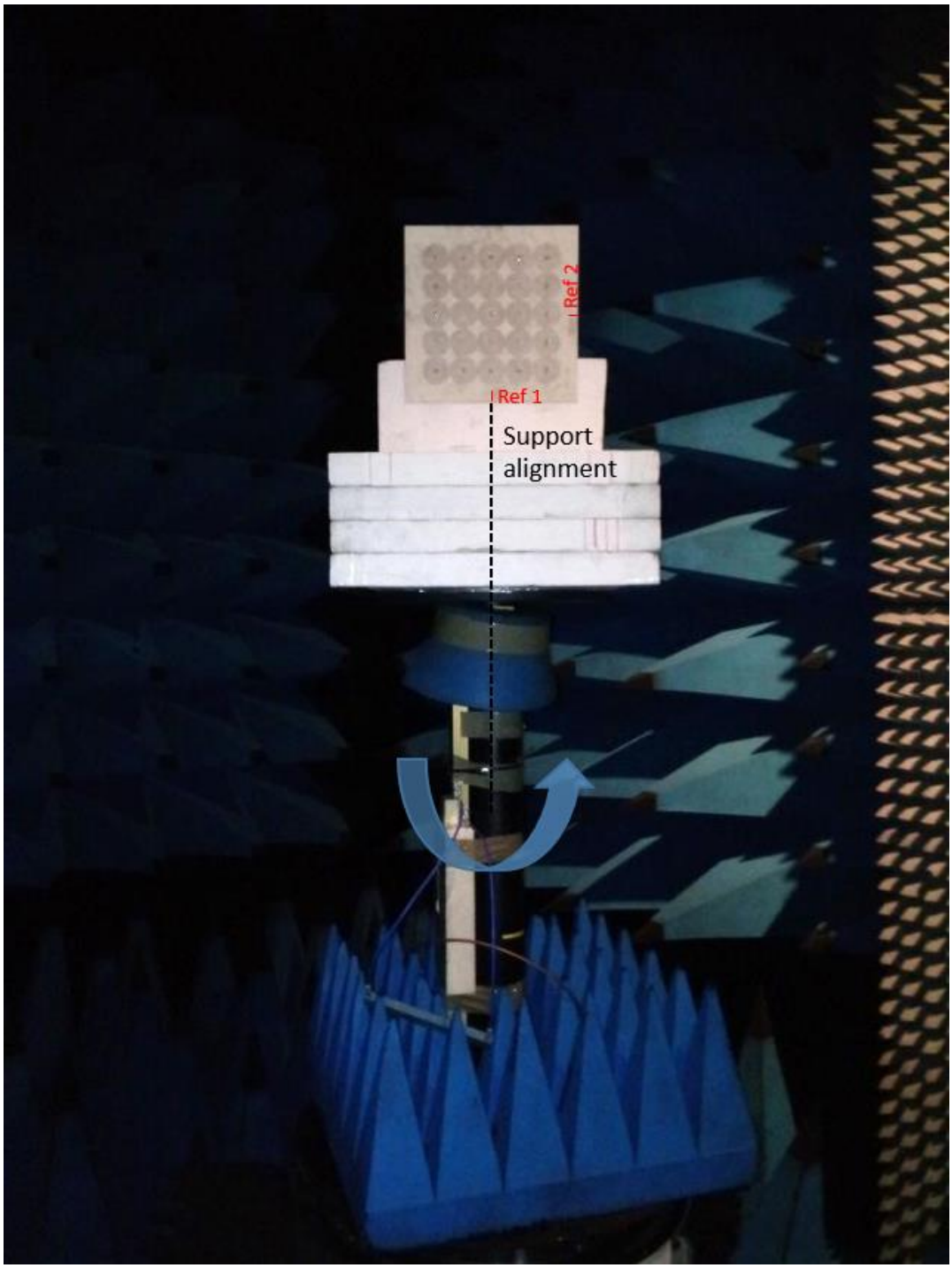

Fig. 3. 23 Antenna array Under Test on anechoic chamber.

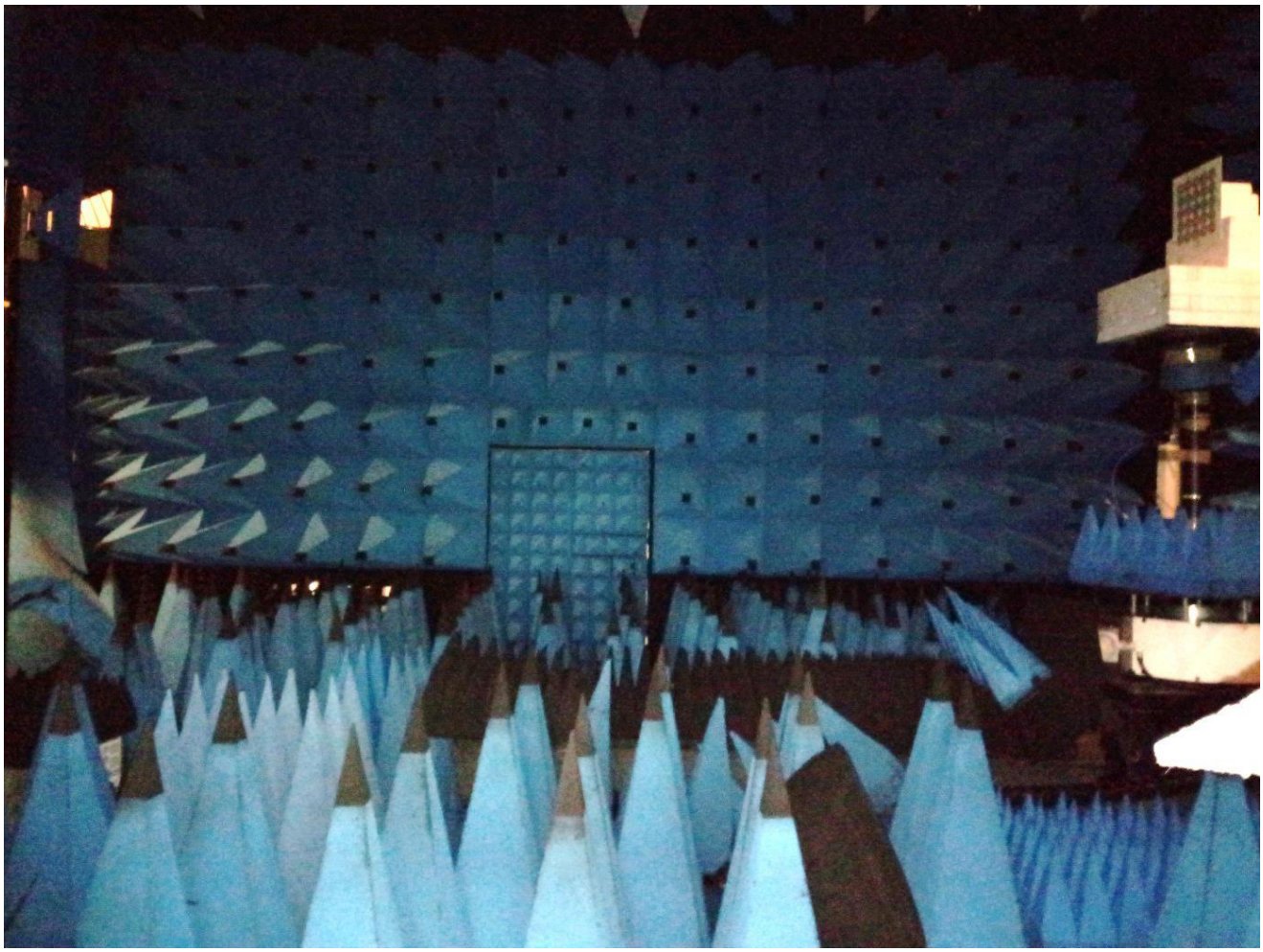

Fig. 3. 24 Spatial configuration of reference antenna and AUT. Distance between antennas is 4.3 m.

3.4.2.1. Gain measurements

Fig. 3. 25 shows the right hand circular polarization gain and the left hand circular polarization gain from the measurements and from the finite simulation in FEKO. The measurements were compensated only in amplitude for the losses in the coax cables and hybrid couplers. In between 0.7 GHz and 1.2 GHz the measured gain is 2-4 dB lower than the simulated gain. Apart from that there is a good agreement between the measurements and the simulations.

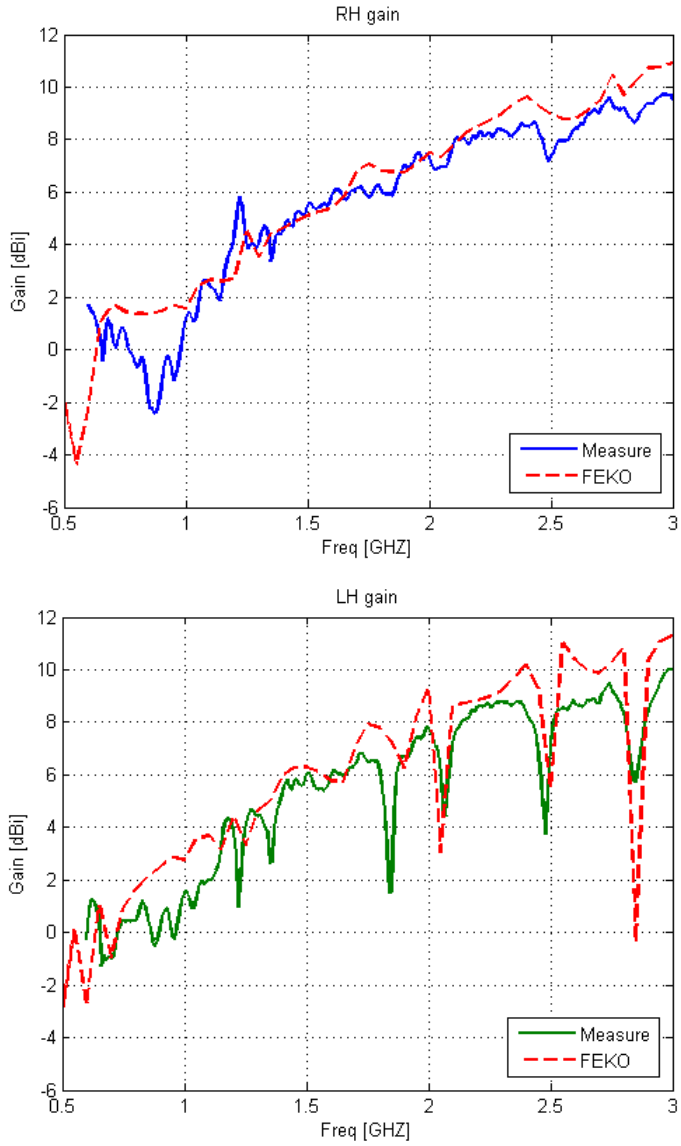

(a)

(b)

Fig. 3. 25 RHC gain (a) and LHC gain (b) from the prototype array (Fig. 3. 18) and from the FEKO simulation of the 3x3 4-arm connecting non-complementary spirals array with one layer of elements with matching resistances of 100 Ω (Fig. 3. 20).

3.4.2.2. Electric field cuts measurements

As it was explained, we took advantage of the array's symmetry and thus the electric field measurements of the prototype array were made only on the antennas numbered 1, 2 and 3 (Fig. 3. 22) and the radiated fields for the full array were reconstructed (Fig. 2. 56)from the horizontal and vertical electric field cuts obtained for those elements. Thus, the reconstructed fields obtained for the horizontal and vertical cuts of the full array were almost identical, with only small differences on the cross polarization levels (the central element was measured on

both cuts, hence the small difference in the cross polarization), and so only the horizontal cuts (phi = 0°) will be shown (Fig. 3. 26 and Fig. 3. 27).

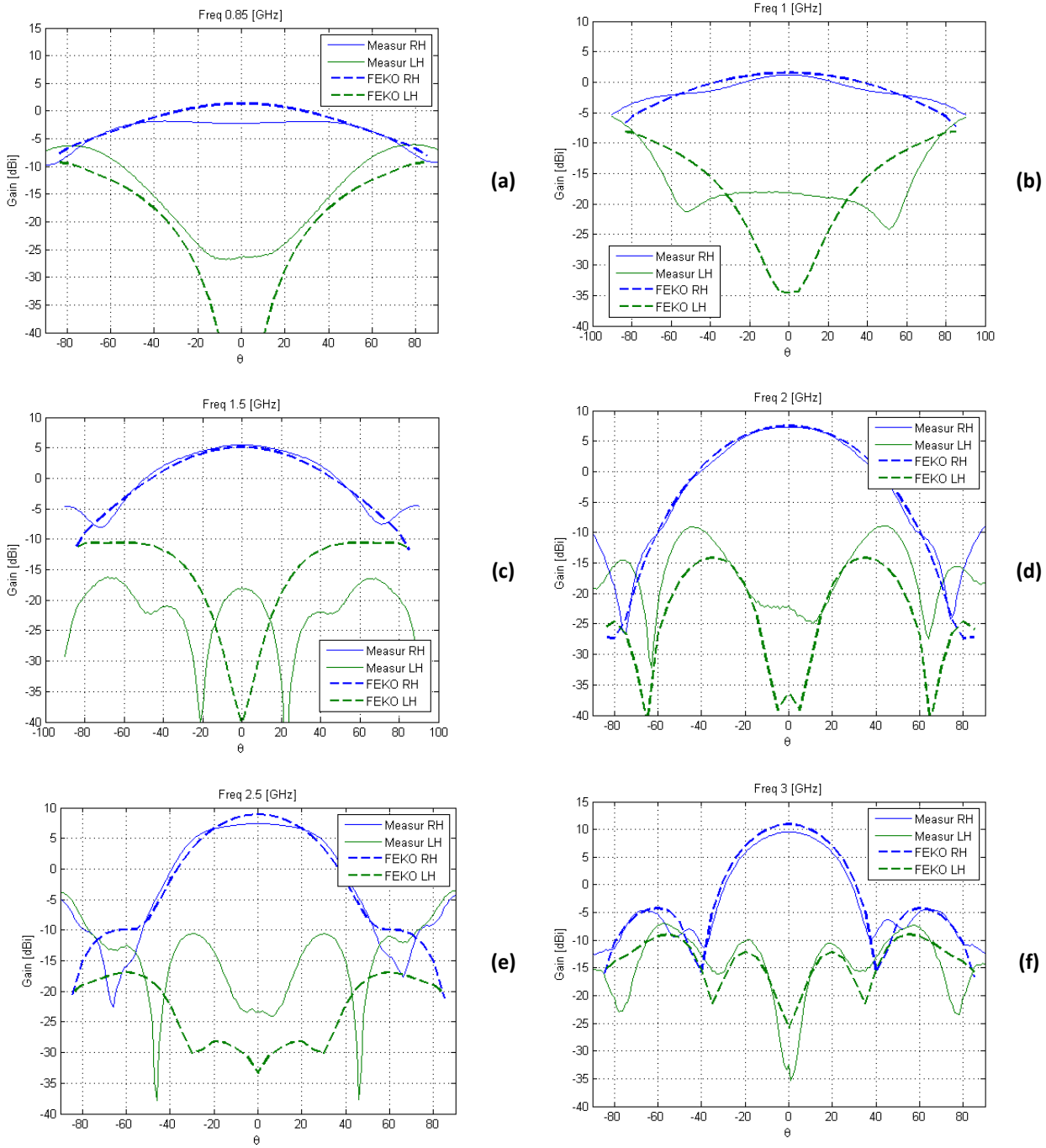

Fig. 3. 26 RH polarization (mode 1) electric field horizontal cuts from the prototype array (Fig. 3. 18) and from the FEKO simulation of the 3x3 4-arm connecting non-complementary spirals array with one layer of elements with matching resistances of 100 Ω (Fig. 3. 20).In (a), (b), (c), (d), (e) and (f) we have, respectively, the fields at 0.85 GHz, 1 GHz, 1.5 GHz, 2 GHz, 2.5 GHz and 3 GHz.

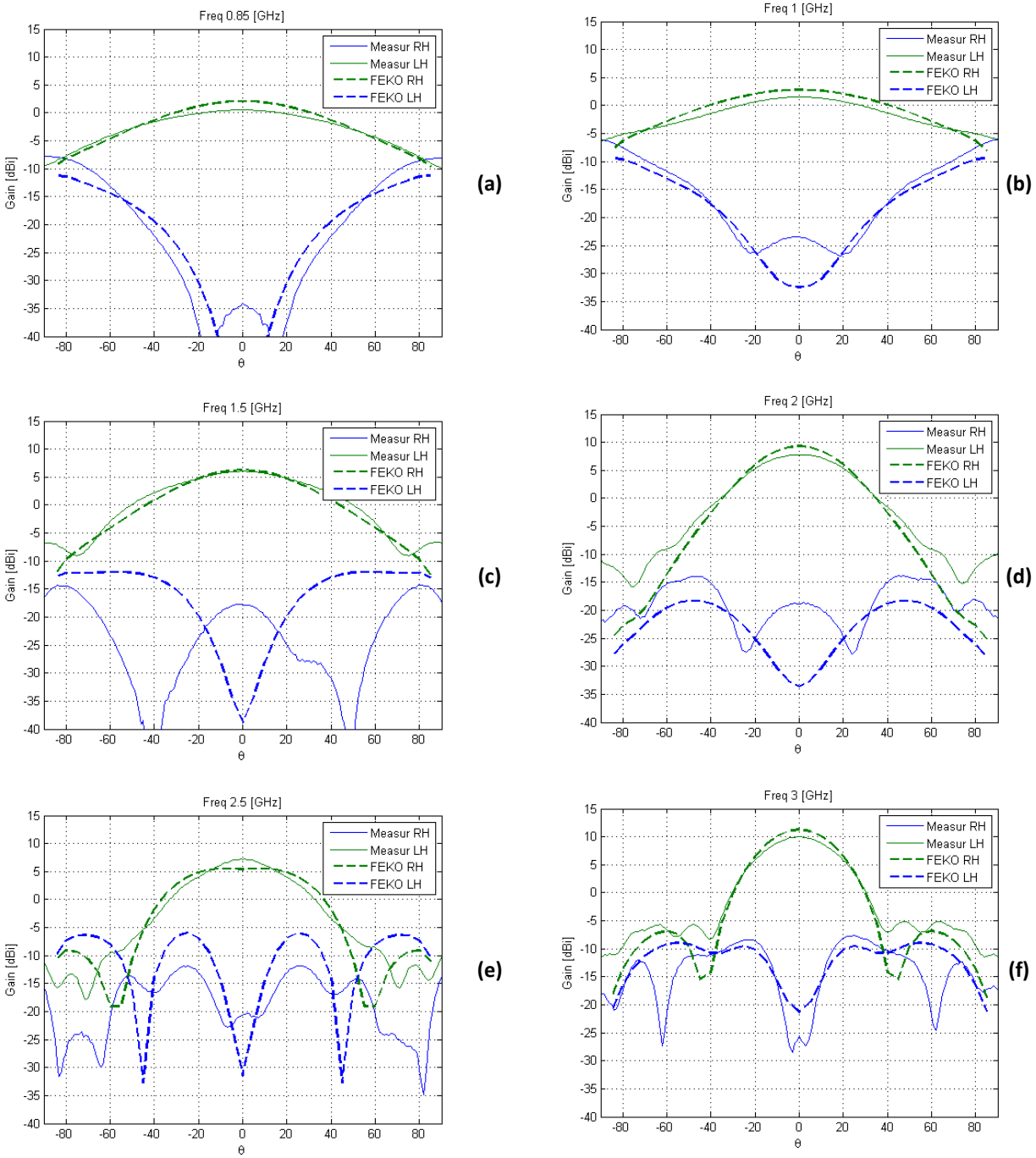

Fig. 3. 27 LH polarization (mode -1) electric field horizontal cuts from the prototype array (Fig. 3. 18) and from the FEKO simulation of the 3x3 4-arm connecting non-complementary spirals array with one layer of elements with matching resistances of 100 Ω (Fig. 3. 20). In (a), (b), (c), (d), (e) and (f) we have, respectively, the fields at 0.85 GHz, 1 GHz, 1.5 GHz, 2 GHz, 2.5 GHz and 3 GHz.

At 0.85 GHz in Fig. 3. 26 we observe a drop of 4 dB at broadside in the RH measured electric field when comparing to the simulation. Apart from that, the measurements have a good

agreement to the simulations at the co-polarization and cross-polarization for both the RH polarized array (mode 1) and the LH polarized array (mode -1).

3.5. Conclusion of chapter 3

A new concept for connecting spiral antennas in an array, consisting of directly connecting the arms of multi-armed spirals in a regular lattice, has been proposed, with examples for 3-arm, 4-arm and 6-arm connecting spiral arrays.

We focused the study on the 4-arm connecting spirals array, and we analyzed the array in infinite and finite simulations using FEKO.

The array shows the potential for an arbitrarily large bandwidth (limited by the size of the array, the larger the array the larger the bandwidth) with gain close to the theoretical maximal gain for the infinite array without a ground plane. The finite array simulations seem to approach the infinite array behavior as long as the array is sufficiently large.

A prototype has been built and the reflection coefficient and RHC and LHC gain simulations have been validated by measurements.

References

Deschamps, G. A., “Impedance Properties of Complementary Multiterminal Planar Structures,” *IRE Transactions on Antennas and Propagation*, vol. 7, no. 5, pp. 371-378, December 1959.

Guinvarc'h, R., Serhir, M. and Ribière-Tharaud, N., “A cavity-backed dual polarized array of connected spiral antennas,” *Proceedings of the 2012 IEEE International Symposium on Antennas and Propagation (APSURSI)*, July 2012.

Hinostroza, I., Guinvarc'h, R., Haupt, R. L. and Louertani, K., “A 6:1 Bandwidth, Low-Profile, Dual-Polarized Ring Array of Spiral Antennas with Connecting Arms,” *IEEE Transactions on Antennas and Propagation*, vol. 64, no. 2, pp. 752-756, February 2016.

Hinostroza, I., Guinvarc'h, R., Haupt, R. L. and Louertani, K., “A dual-polarized Wideband Planar Phased Array with Spiral Antennas,” *IEEE Transactions on Antennas and Propagation*, vol. 62, no. 9, pp. 4547-4553, June 2014.

Huffman, J. A. and Cencich, T., “Modal Impedances of Planar Non-Complementary, N-fold Symmetric Antenna Structures,” *IEEE Antennas and Propagation Magazine*, vol. 47, no. 1, pp. 110-116, February 2005.

McFadden, M. and Scott Jr., W. R., “Analysis of the Equiangular Spiral Antenna on a Dielectric Substrate,” *IEEE Transactions on Antennas and Propagation*, vol. 55, no. 11, pp. 3163-3171, November 2007.

Rahman, N., Lasser, G., Elmansouri, M., Filipovic, D. S., “3-Arm Spiral Antennas for Direction Finding Applications,” *2017 IEEE International Symposium on Antennas and Propagation & USNC/URSI National Radio Science Meeting (APSURSI)*, 9 – 14 July 2017

Steyskal, H., Ramprecht, J. and Holter, H., “Spiral Elements for Broad-Band Phased Arrays,” *IEEE Transactions on Antennas and Propagation*, vol. 53, no. 8, pp. 2558-2562, August 2005.

FEKO, Altair Engineering, Inc., www.hyperworks.com/feko, Example Guide FEKO A-16.

Conclusion and perspectives

Conclusion

In this thesis a Concentric Ring Array of Connecting Spirals has been developed. The connections between spirals of opposite polarizations reduce the reflection coefficient at lower frequencies, effectively dividing the lowest frequency of operation of the spirals by 3.3. At the same time, the concentric rings topology had the radius and relative rotations of each ring optimized using Genetic Algorithms to minimize the RSLL at higher frequencies.

The addition of a size constraint in the optimization procedure resulted in an array with a 29% smaller aperture area than the previous design while maintaining the same bandwidth. The optimized array was simulated using FEKO, and it operates from 1 GHz to 6.9 GHz and can be steered up to 30° in addition to meeting the following requirements:

- Dual circular polarization (Axial Ratio below 3 dB)
- Reflection coefficient below -10 dB
- Relative Sidelobe Level below -10 dB
- Compact design (circumscribed by a 35 cm radius circle)

This new design was further updated using the WAVES technique in order to include a scaled down copy in its center. The Concentric Ring Array of Connecting Spirals with scaled down WAVES was then simulated using FEKO in its three modes of operation: only the larger antennas turned on and the smaller elements matched to 220 Ω resistances (1 GHz - 4 GHz), all antennas turned on (4 GHz – 9.5 GHz) and only the smaller antennas turned on and the larger ones matched to 220 Ω resistances (9.5 GHz – 13 GHz).The overlapping bandwidth of the 3 modes of operation goes from 1 GHz to 13 GHz.

By comparing both designs we noticed a trade-off between gain and bandwidth. The Concentric Ring Array without WAVES has a gain about 1.7 dB larger from 4 GHz to 6 GHz, while also having a single mode of operation and thus a simpler feeding network. The bandwidth is however considerably larger in the Concentric Ring Array with WAVES.

As the Concentric Ring Array of Connecting Spirals is sparse, it has a low gain when compared to the surface gain, so we proposed a new design for the array of connected spirals. The new design consists of arranging spirals in a uniform array and connecting the arms of the neighboring spirals.

We focused our studies in the 4–arm spirals as they presented simulations with better adaptation when compared to 3-arm spirals and fewer resonances when compared to 6-arm spirals. Moreover the feeding network for 4-arm spirals require phases that are multiples of 90°, which was easy for prototyping.

The new connected 4-arm design has been analyzed in infinite array simulations and finite array simulations using FEKO. The simulations indicate that the design can have an arbitrarily large bandwidth depending on the finiteness of the array as the infinite simulations did not show a limit.

A prototype has been built and the reflection coefficient measurements as well as the gain measurements for RHC and LHC polarizations agree with the FEKO simulations.

Perspectives

Concentric Ring Array

It would be interesting the further explore the possibilities of using the WAVES technique at the Concentric Ring Array of connecting spirals. The interleaved WAVES topology that has been proposed should be further investigated to understand the origin of the drops in gain observed in simulation.

One can also imagine an array with more than two element sizes. For instance, the scaled WAVES topology proposed has the possibility of adding a third copy further scaled down, and a forth and so on. The limiting factor in this approach would be the feeding strategy. It would be necessary to conceive ways of feeding the ever smaller spirals.

In this line, an experimental realization of the conceived Concentric Ring Array with scaled WAVES would be interesting. Realizing the array with different sizes and figuring out how to

implement the inhomogeneous feeds would give insight on the practical challenges of further scaling the array.

Moreover we could study how to conform the Concentric Ring Array to different aperture shapes and topologies. In several applications it is important that the array has the shape of the platform rather than a planar topology so it would be interesting to study the implications of reshaping the concentric rings and how to maintain the arrays performances under such conditions.

We could also work on occupying different shapes of apertures, for instance square or rectangular aperture. Using circular rings when the available aperture is square or rectangular implies having unoccupied space. One way of better occupying the space is to use superellipses (*Weisstein*) instead of circles for the rings (Fig. 1). Such an approach would imply in larger sidelobes as the square or rectangular aperture would modulate the array factor, but one could turn off the corner elements at higher frequencies to avoid such issues. In would also be important to figure out how to implement the connections between spirals in such an array topology.

Among the parameters to be optimized in such an array we could propose the length of the major and minor axis, the degree p of the superquadric as well as the position of the first element in the superquadric (which corresponds to the angular position of the first elements in the concentric ring array), for each of the superellipses in the concentric superellipse ring array.

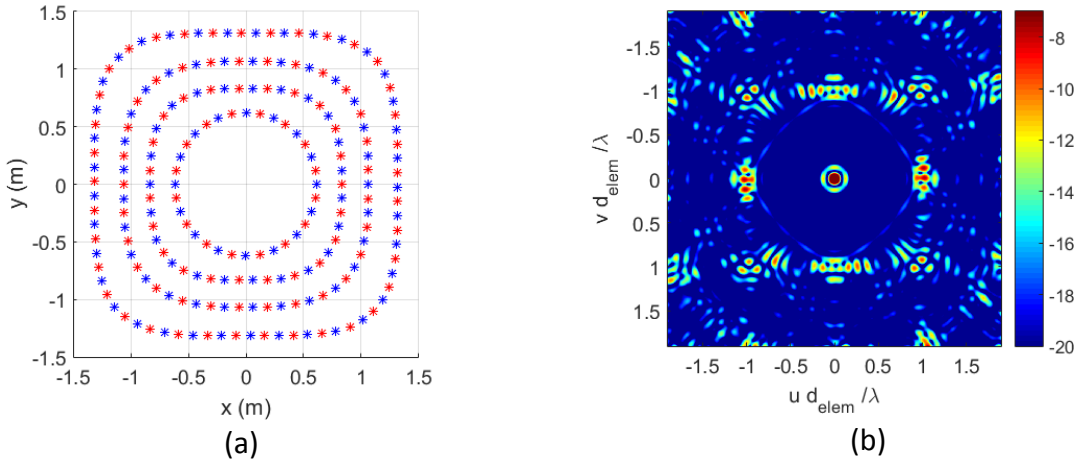

Fig. 1 Concentric superellipse ring array example. In (a) we have the elements positioning with the RHC polarized elements in blue and the LHC polarized elements in red. The first ring have a superellipse with degree 2 (a circle), both the intermediate ring have a degree of 3 and the largest ring has a degree of 4, thus being the one closer to a square. In (b) we have the array factor of the array with the axis normalized by d_{elem}/λ, with $d_{elem} = 24.34\ cm$ being the distance between two elements of the same polarization in a ring.

Finally we could analyze the effect of array errors on the radiated polarization of the full array in a similar fashion as we have done in appendix A. It is possible to extend the proposed method to include the mutual coupling between the elements by including the mutual impedance matrix of the array.

4-Arm Connected Spiral Array

Using the non-complementary spiral design for the 4-arm connected spiral array was the simplest way we found to make the spiral arms match to 50 Ω coaxial cables. However, the simulations using self-complementary spirals present better reflection coefficient in the higher frequencies. In addition the non-complementary design demands a thinner meshing, which limits the ability to analyze the array with simulations.

It would be interesting to find alternative ways of adapting the spirals as it could potentially enhance the bandwidth as well as allowing coarser meshing, thus faster simulations.

We could try different lattices for the array. The prototype array was designed for a square lattice, but we could easily dislocate each other row of spirals by half the spacing to obtain a triangular lattice, which would make the grating lobes appear at higher frequencies. It could also be interesting to observe how the array behaves when conformed to different topologies.

The influence of the shape of the connection could be studied as well. In previous works the shape of the connection had to be optimized for the connections between spiral arms to work properly, so we could imagine such an approach could enhance the design.

Another important step to take is to explore the behavior of larger arrays. In the current prototype there is only one central element, it would be important to analyze the active reflection coefficient of the other elements as well.

The steering behavior of the array should be further explored. We have observed that the resonances that appear when the connected spiral antennas are steering are related to the length of the spiral arms and are more intense as the steering angle is larger, much like in arrays of disconnected spirals. In arrays of disconnected spirals such resonances are not observed in measurements, so it would be important to verify if the same happens for the connected spirals.

Up to this point the study of the connected spiral array has been done without a backing plane. For many applications the array needs to be unidirectional. Hence, another point to be further studied is the use of a ground plane or of a cavity, which is quite challenging for an ultrawideband array.

Finally it would be interesting to obtain a theoretical model of the array, being it a circuit model, a transmission line model, etc. The simulations of the array take a long time and that considerably limits the power to analyze larger arrays in different scenarios. Having a relatively reliable model would be of great help.

References

Weisstein, E. W., “Superellipse.” From MathWorld – A Wolfram Web Resource. http://mathworld.wolfram.com/Superellipse.html

List of Publications

Journal

Ruiz, P. M., Hinostroza, I., Guinvarc'h, R. and Haupt, R. L., "Genetic algorithm optimization of a dual polarized concentric ring array," *ACES Express Journal (2017 Italy Conference special edition)*, accepted.

Ruiz, P. M., Hinostroza, I., Guinvarc'h, R. and Haupt, R. L., "Impact of array errors on the Axial Ratio of Planar Arrays,", in submission.

Ruiz, P. M., Hinostroza, I., Guinvarc'h, R. and Haupt, R. L., "A multi-octave planar array of connected 4-arm spirals," in preparation.

Conference

Ruiz, P. M., Hinostroza, I., Guinvarc'h, R. and Haupt, R. L., "Size Constraint in Design of Concentric Ring Array," *Proceeding of the 2015 IEEE International Symposium on Antennas and Propagation & USNC/URSI National Radio Science Meeting (APSURSI)*, Vancouver, BC, Canada, 19-24 July 2015

Ruiz, P. M., Hinostroza, I., Guinvarc'h, R. and Haupt, R. L., "Phase error analysis of a dual polarized concentric ring array," *Proceeding of the 2016 IEEE International Symposium on Antennas and Propagation (APSURSI)*, Fajardo, Puerto Rico, 26 June – 01 July 2016

Ruiz, P. M., Hinostroza, I., Guinvarc'h, R. and Haupt, R. L., "Genetic algorithm optimization of a dual polarized concentric ring array," *Proceeding of the 2017 International Applied*

Computational Electromagnetics Society Symposium – Italy (ACES), Florence, Italy, 26-30 March 2017.

Ruiz, P. M., Hinostroza, I., Guinvarc'h, R. and Haupt, R. L., "Concentric ring array of connecting spirals with WAVES," *Proceeding of the 2017 IEEE International Symposium on Antennas and Propagation & USNC/URSI National Radio Science Meeting (APSURSI)*, San Diego, CA, USA, 9-14 July 2017.

Ruiz, P. M., Hinostroza, I., Guinvarc'h, R. and Haupt, R. L., "Concentric ring array of connecting spirals with interleaved WAVES," *Proceedings of the 2018 United States National Committee of URSI National Radio Science Meeting (USNC-URSI NRSM)*, Boulder, CO, USA, 4-7 January 2018.

Ruiz, P. M., Hinostroza, I., Guinvarc'h, R. and Haupt, R. L., "Antenna Pattern Effects in a Low Sidelobe Circularly Polarized Planar Array Due to Element Errors," *Proceedings of the International Conference on Electromagnetics in Advanced Applications (ICEAA-IEEE APWC), Cartagena, Colombia, 10-14 September 2018, accepted.*

Appendix A – Impact of Array Errors on the Axial Ratio of Planar Arrays

Circularly polarized antenna arrays have many practical applications in communications and radar systems. Satellite communication arrays rely on circular polarization due to Faraday rotation of the signal as it passes through the ionosphere. Meteorological radar arrays must have very high isolation between vertical and horizontal polarization in order to distinguish between different types of precipitation. Calibrating errors enhances the polarization isolation (*Fulton, 2010*) (*Fulton, 2016*).

Random array errors due to manufacturing tolerances, equipment aging, and temperature change the axial ratio of circularly polarized arrays. Traditionally, random errors in arrays have been analyzed to determine the impact on the sidelobe level. This appendix looks at how random amplitude and phase errors change the axial ratio of a dual or circularly polarized planar array.

Ruze first analyzed the impact of aperture errors on antenna patterns (*Ruze, 1966*). Random errors in an array are considered statistically independent from element to element. These errors produce very broad array patterns that are superimposed on the no-error patterns resulting in "filled-in" nulls and the increased gain of low sidelobes (*Brookner, 1991*) (*Haupt, 2010*).

In this appendix, position errors and random element failures are ignored, but amplitude and phase errors are not.

The goal of this appendix is to model a circularly polarized planar array by an array of crossed dipoles with errors on the feeding currents in order to quantify the impact of array errors on the polarization.

A.1 Axial Ratio expression

Having the linear polarized fields (E_θ and E_ϕ), we can calculate the right handed and left hand polarized electric fields (E_{rhp} and E_{lhp}) using the following equations:

$$E_{rhp} = \frac{1}{\sqrt{2}} \left(E_\theta - j\, E_\phi \right) \tag{A.1}$$

$$E_{lhp} = \frac{1}{\sqrt{2}} \left(E_\theta + j\, E_\phi \right) \tag{A.2}$$

We can then calculate the cross polarization ratio and find the AR with the following equations:

$$xpolr^2 = \frac{\left| E_{rhp} \right|^2}{\left| E_{lhp} \right|^2} \tag{A.3}$$

$$AR_{dB} = 20\, log_{10} \left(\frac{xpolr + 1}{xpolr - 1} \right), xpolr > 1 \tag{A.4}$$

which means that $\left| E_{rhp} \right| > \left| E_{lhp} \right|$ (a reasonable assumption for a right handed polarized antenna).

By taking the Laurent series of $ln\left(\frac{x+1}{x-1}\right), x \to \infty$ we get $\frac{2}{x} + O\left(\frac{1}{x^3}\right)$, which gives an approximation for the AR expression, that becomes the following by combining (A.3) and (A.4):

$$AR_{dB} = \frac{40}{ln(10)} \sqrt{\frac{\left| E_{lhp} \right|^2}{\left| E_{rhp} \right|^2}} \tag{A.5}$$

A.2 Crossed Dipoles Model

In this section we present a model of a circularly polarized planar array of crossed dipoles with random amplitude and phase errors. In order to find the AR of the crossed dipoles array, we calculate the orthogonal linear electric fields of the array. We restrict the analysis to right handed polarized crossed dipoles in this paper, but the results apply to left handed polarized

arrays as well. If the two crossed dipoles have the same length, with one along the x-axis and the other along the y-axis (*Haupt, 2004*):

$$E_\theta = -j\frac{\omega\mu L e^{-jkr}}{4\pi r}\left[I_h\cos(\theta)\cos(\phi) + I_v e^{j\frac{\pi}{2}}\cos(\theta)\sin(\phi)\right] \tag{A.6}$$

$$E_\phi = -j\frac{\omega\mu L e^{-jkr}}{4\pi r}\left[-I_h\sin(\phi) + I_v e^{j\frac{\pi}{2}}\cos(\phi)\right] \tag{A.7}$$

where ω is the angular frequency, μ is the space magnetic permeability, k is the wave number, r is the distance from the antenna to the observation point, I_h is the current on the horizontally oriented dipole, I_v is the current on the vertically oriented dipole, L is the length of the dipoles, θ is measured from the z-axis and ϕ is measured from the x-axis.

If we neglect the mutual coupling between the different elements but feed each of the crossed dipoles with a different current, then the electric field of an array of N crossed dipoles is given by

$$E_\theta = -j\frac{\omega\mu L e^{-jkr}}{4\pi r}\sum_{i=1}^{N}\left\{e^{-j\delta_{pos_i}}\left[I_{hi}\cos(\theta)\cos(\phi) + I_{vi}e^{j\frac{\pi}{2}}\cos(\theta)\sin(\phi)\right]\right\} \tag{A.8}$$

$$E_\phi = -j\frac{\omega\mu L e^{-jkr}}{4\pi r}\sum_{i=1}^{N}\left\{e^{-j\delta_{pos_i}}\left[-I_{hi}\sin(\phi) + I_{vi}e^{j\frac{\pi}{2}}\cos(\phi)\right]\right\} \tag{A.9}$$

$$\begin{aligned}\delta_{pos_i} = \frac{2\pi}{\lambda}\{&[\sin(\theta)\cos(\phi) - \sin(\theta_s)\cos(\phi_s)]x_i \\ &+ [\sin(\theta)\sin(\phi) - \sin(\theta_s)\sin(\phi_s)]y_i\}\end{aligned} \tag{A.10}$$

where $[x_i, y_i]$is the position of the i-th crossed dipoles element. Errors are assumed to be amplitude and phase deviations from the desired current.

$$I_{hi} = I\,(1 + \delta I_{hi})e^{-j\delta\phi_{hi}} \tag{A.11}$$

$$I_{vi} = I\,(1 + \delta I_{vi})e^{-j\delta\phi_{vi}} \tag{A.12}$$

where I_{hi}, I_{vi}, $\delta\phi_{hi}$ and $\delta\phi_{vi}$ are, respectively: the horizontal dipole normalized amplitude error, the vertical dipole normalized amplitude error, the horizontal dipole phase error and the vertical dipole phase error for the i-th crossed dipoles element.

A.3 Axial Ratio Derivation

This section presents the derivation of the AR expression for the crossed dipoles array with errors. By means of a simple normalization, observing the broadside radiation without steering ($[\theta, \phi] = [\theta_s, \phi_s] = [0°, 0°]$) and using (A.11) and (A.12), (A.8) and (A.9) reduces to the following equations:

$$E_\theta = \sum_{i=1}^{N}(1 + \delta I_{hi})e^{-j\delta\phi_{hi}} \tag{A.13}$$

$$E_\phi = e^{j\frac{\pi}{2}}\sum_{i=1}^{N}(1 + \delta I_{vi})e^{-j\delta\phi_{vi}} \tag{A.14}$$

At this point we consider the errors to be small and make the Taylor expansion $e^x = 1 + x + O(x^2)$, as well as neglect the terms $\delta I_{hi}\delta\phi_{hi}$ and$\delta I_{vi}\delta\phi_{vi}$. Next, decomposing the fields into right and left handed polarization components using (A.1) and (A.2) results in:

$$E_{rhp} = \frac{1}{\sqrt{2}}\sum_{i=1}^{N}(2 + \delta I_{hi} + \delta I_{vi} - j\delta\phi_{hi} - j\delta\phi_{vi}) \tag{A.15}$$

$$E_{lhp} = \frac{1}{\sqrt{2}}\sum_{i=1}^{N}(\delta I_{hi} - \delta I_{vi} - j\delta\phi_{hi} + j\delta\phi_{vi}) \tag{A.16}$$

These equations simplify to:

$$E_{rhp} = \frac{1}{\sqrt{2}}(2N + \delta I_+ - j\delta\phi_+) \tag{A.17}$$

$$E_{lhp} = \frac{1}{\sqrt{2}}(\delta I_- - j\delta\phi_-) \tag{A.18}$$

where:

$$\delta I_- = \sum_{i=1}^{N}(\delta I_{hi} - \delta I_{vi}) \tag{A.19}$$

$$\delta\phi_- = \sum_{i=1}^{N}(\delta\phi_{hi} - \delta\phi_{vi}) \tag{A.20}$$

$$\delta I_+ = \sum_{i=1}^{N}(\delta I_{hi} + \delta I_{vi}) \tag{A.21}$$

$$\delta\phi_+ = \sum_{i=1}^{N}(\delta\phi_{hi} + \delta\phi_{vi}) \tag{A.22}$$

Finally, by using (A.5), (A.17) and (A.18) we get:

$$AR_{dB} = \frac{20}{N\ ln(10)}\sqrt{\frac{{\delta I_-}^2 + {\delta\phi_-}^2}{\left[\left(1 + \frac{\delta I_+}{2N}\right)^2 + \left(\frac{\delta\phi_+}{2N}\right)^2\right]}} \tag{A.23}$$

Assuming that the terms $\frac{\delta I_+}{2N}$ and $\frac{\delta\phi_+}{2N}$ to be small enough to neglect, then we get:

$$AR_{dB} = \frac{20}{N\ ln(10)}\sqrt{\delta I_{-}{}^{2} + \delta\phi_{-}{}^{2}} \tag{A.24}$$

The AR of the array depends on the difference between the amplitudes and phases of the horizontal and vertical dipole currents. Random errors at the elements average, so (A.24) is proportional to $\frac{1}{N}$.

A.4 Results

In order to validate (A.24), we calculated the AR of one crossed dipole element with errors 10^6 times. The errors are zero-mean, normally distributed with standard deviations of $\sigma_{\phi_h} = \sigma_{\phi_v} = 0.2$ (11.46°) and $\sigma_{I_h} = \sigma_{I_v} = 0.1$ (10%). We calculated the AR using (A.24), then created the histograms in Fig. A. 1 and calculated the figures of merit shown in equations (A.25), (A.26), (A.27) and (A.28).

$$\left|AR_{dB} - AR_{dB_{(A.24)}}\right|_{99\%} = 0.68\ dB \tag{A.25}$$

$$\left|AR_{dB} - AR_{dB_{(A.24)}}\right|_{95\%} = 0.32\ dB \tag{A.26}$$

$$\frac{1}{N}\sum_{i=1}^{N}\left|AR_{dB^i} - AR_{dB_{(A.24)^i}}\right| = 0.088\ dB \tag{A.27}$$

$$\frac{1}{N}\sum_{i=1}^{N}\left|\frac{AR_{dB^i} - AR_{dB_{(A.24)^i}}}{AR_{dB^i}}\right| = 3\% \tag{A.28}$$

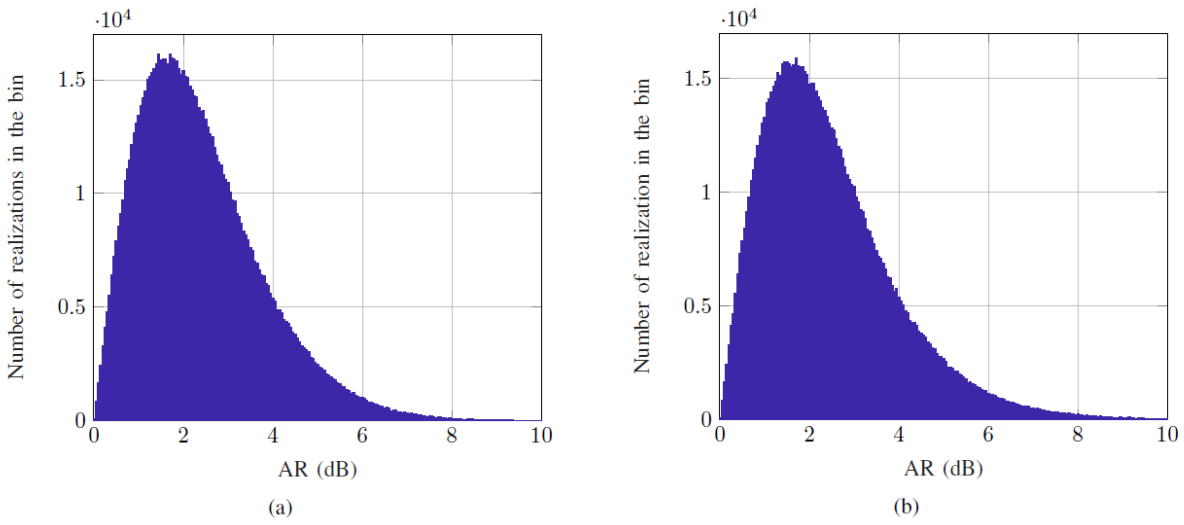

Fig. A. 1 Histogram of the Monte Carlo simulations of the AR calculations for a single crossed dipoles element at broadside. (a) with approximations in (A.24) (b) without approximations. The bins in the histogram have a 0.05 dB width.

As we can see, the results obtained by the equation (A.24) are rather close to those obtained without any approximations (using equations (A.1), (A.2), (A.3), (A.4), (A.13) and (A.14)).

In the case where all the errors are independent identically distributed Gaussian with zero mean, we can identify (A.24) as a Rayleigh distribution. By looking at the histograms (Fig. A. 1) we can see that, even when the errors have different standard deviations we still observe a Rayleigh-like behavior.

In order to observe the effect of having more than one element, we made the same test for a small uniform 5x5 planar array with a spacing of $\lambda/2$ (Fig. A. 2). We can observe that, as it can be predicted from (A.24), the more elements we add to the array, the smaller the variance on the results, which get closer to the ideal case without errors.

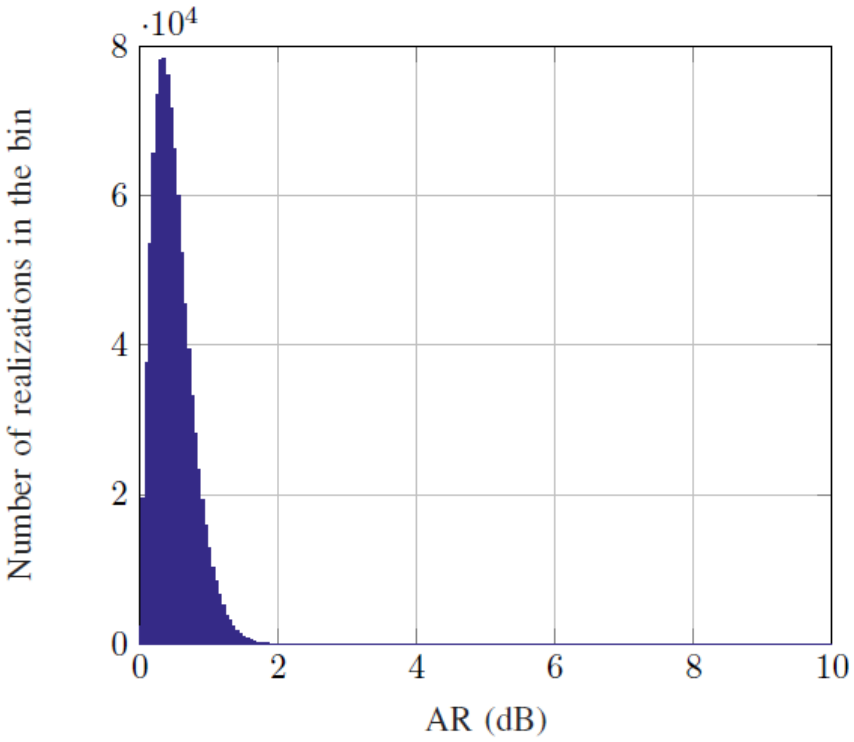

Fig. A. 2 Histogram of the Monte Carlo simulations of the AR calculations without approximations for 25 crossed dipoles elements looking at broadside. The bins in the histogram have a 0.05 dB width.

A.4.1. Example with steering

Scanning the main beam away from broadside makes the calculations for the AR much more complicated. However, it is simple to make a Monte Carlo simulation of the AR at the steering direction. Using (A.8), (A.9) and (A.10) and making ($[\theta, \phi] = [\theta_s, \phi_s]$ we get:

$$E_\theta = -j\frac{\omega\mu L e^{-jkr}}{4\pi r}\sum_{i=1}^{N}\left[I_{hi}\cos(\theta_s)\cos(\phi_s) + I_{vi}e^{j\frac{\pi}{2}}\cos(\theta_s)\sin(\phi_s)\right] \quad \text{(A.29)}$$

$$E_\phi = -j\frac{\omega\mu L e^{-jkr}}{4\pi r}\sum_{i=1}^{N}\left[-I_{hi}\sin(\phi_s) + I_{vi}e^{j\frac{\pi}{2}}\cos(\phi_s)\right] \quad \text{(A.30)}$$

In the steering direction, the radiated fields are not a function of the element positions but are a function of the number of elements.

For this simulation, we will consider first a single element looking at the steering direction (Fig. A. 3), then a small uniform 5x5 planar array with a spacing of $\lambda/2$ (Fig. A. 4). The errors are independent Gaussian distributed, with the amplitude errors having a standard deviation $\sigma_{I_h} = \sigma_{I_v} = 0.1$ (10%) and the phase errors $\sigma_{\phi_h} = \sigma_{\phi_v} = 0.2$ (11.46°). For the simulation we will consider a steering of $[\theta_s, \phi_s] = [30°, 0°]$, which give an AR of 1.25 dB for an array without errors.

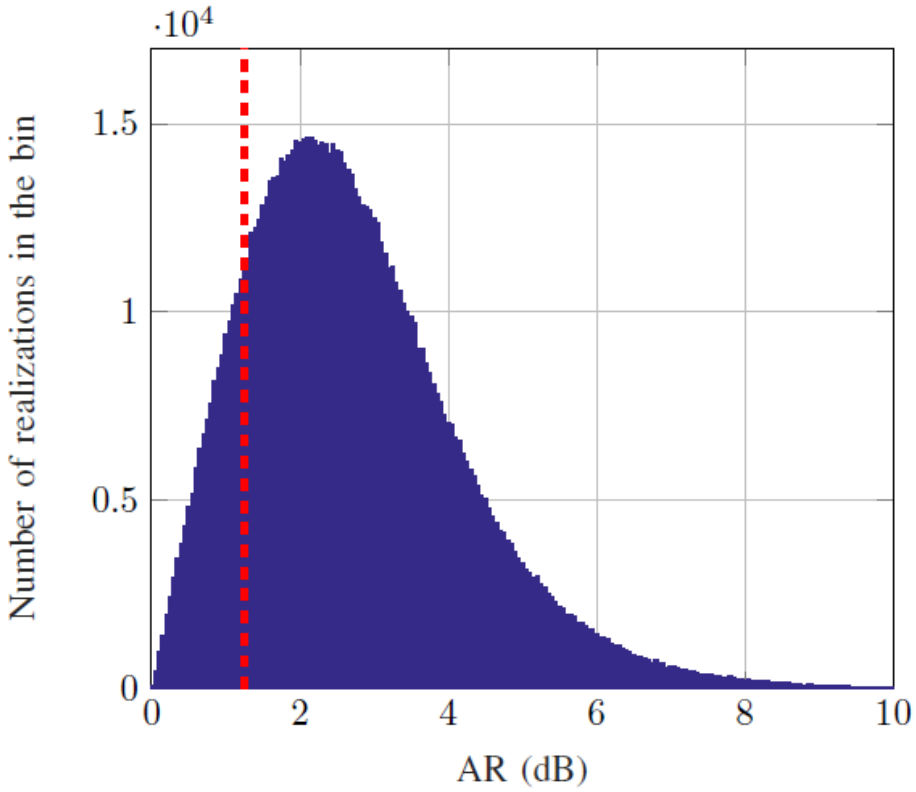

Fig. A. 3 Histogram of the Monte Carlo simulations of the AR calculations without approximations for a single crossed dipoles element at 30°. In dashed red we have the AR without errors (1.25 dB). The bins in the histogram have a 0.05 dB width.

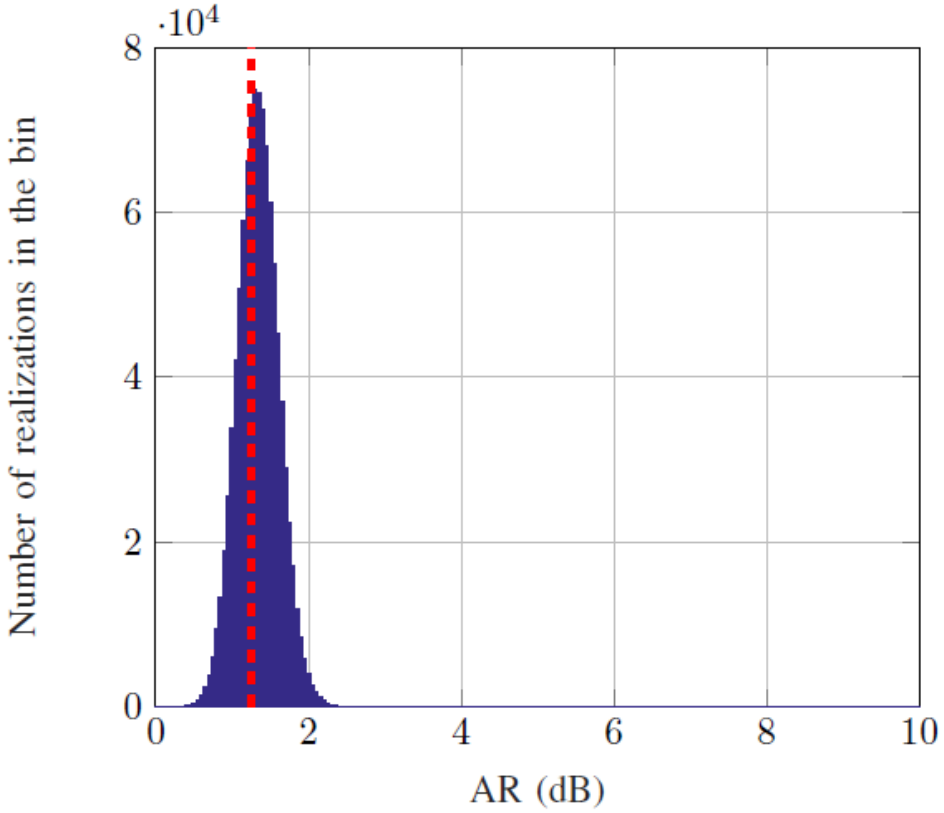

Fig. A. 4 Histogram of the Monte Carlo simulations of the AR calculations without approximations for 25 crossed dipoles elements scanned to 30°. In dashed red we have the AR without errors (1.25 dB). The bins in the histogram have a 0.05 dB width.

Fig. A. 3 shows that the AR of the isolated element at the steering direction degrades when errors are considered. Comparing the broadside case in Fig. A. 1 with the scanned case in Fig. A. 3, we observe that the AR degrades off-broadside.

In Fig. A. 4, we observe that the AR from the Monte Carlo runs is nearly the same as the estimate calculated using errorless feeding currents. The Monte Carlo runs get closer to the errorless case as the number of elements in the array increases.

A.5 Conclusions of Appendix A

By analyzing the equations for a radiating element composed of two crossed dipoles with errors in amplitude and phase, we were able to find a simple formulation for the resulting AR. This

estimate depends on the difference between the amplitudes and phases of the horizontal and vertical dipole currents. Monte Carlo simulations validate the approximate formulas for broadside arrays and are used to explore scanned arrays.

We observe that, considering the feeding errors to be independent identically distributed Gaussian variables, the expression in (A.24) leads to a Rayleigh probability density function. Still from (A.24), we expect that, as the number of elements (N) in the array gets larger, random errors have less impact on the AR of the array due to averaging, which can be observed in Fig. A. 2 and Fig. A. 4.

References

Brookner, E., *"Antenna Array Fundamentals Part 2," Practical Phased Array Antenna Systems*, Artech House, Norwood, 1991.

Fulton, C. and Chappell, W. J., "Calibration of a Digital Phased Array for Polarimetric Radar," *Proceedings of the 2010 IEEE MTT-S International Microwave Symposium*, pp. 161-164, 2010

Fulton, C., Yeary, M., Thompson, D., Lake, J. and Mitchel, A., "Digital Phased Arrays: Challenges and Opportunities," *Proceedings of the IEEE*, vol.104, no. 3, pp. 487-503, March 2016.

Haupt, R. L., "Adaptative Crossed Dipole Antennas Using a Genetic Algorithm," *IEEE Transactions on Antennas and Propagation*, vol. 52, no. 8, pp.1976-1982, August 2004.

Haupt, R. L., *Antenna Arrays, a Computational Approach*, John Wiley & Sons, New Jersey, USA, 2010.

Ruze, J., “Antenna Tolerance Theory - A Review,” *Proceedings of the IEEE*, vol. 54, pp. 633-640, April 1966.

université PARIS-SACLAY
ÉCOLE DOCTORALE
Physique et ingénierie : électrons, photons, sciences du vivant (EOBE)

Titre : Réseaux multi-octave d'antennes spirales connectées

Mots clés : Antennes, Large Bande, Electromagnétisme, Réseaux d'antennes, Radar

Résumé : Une des problématiques qui est souvent associée aux réseaux large bande est l'apparition des lobes de réseaux, liée à la périodicité de l'espacement entre les éléments du réseau. Un autre problème dans les réseaux large bande est la fréquence de fonctionnement de l'élément du réseau. La plus basse fréquence d'opération est généralement liée à la taille de l'élément.
Dans cette thèse un réseau d'anneaux concentriques a été développé. Les connections entre les spirales de polarisation opposée diminuent le coefficient de réflexion dans les fréquences basses.
La topologie des anneaux concentriques a été optimisée avec des Algorithmes Génétiques pour minimiser le niveau des lobes secondaires relatifs dans les hautes fréquences.
L'addition d'une contrainte de taille dans la procédure d'optimisation a assuré que le réseau soit compact. Le réseau optimisé opère entre 1 et 6.9 GHz. Le design a été d'avantage développé avec la technique WAVES avec l'inclusion d'une copie réduite en son centre, ce qu'a permis l'extension de la bande passante jusque 13 GHz.
De plus, nous avons proposé un nouveau design pour le réseau de spirales connectés qui consiste en des antennes spirales disposées dans un réseau uniforme avec les bras connectés aux bras des antennes voisines. Les simulations indiquent que le réseau peut avoir une bande passante arbitrairement large selon la finitude du réseau. Un prototype a été construit et mesuré pour valider le concept.

Title : Multi-octave Connected Spiral Arrays

Keywords : Antenna, Wideband, Electromagnetism, Antenna Arrays, Radar

Abstract: One of the usual problems associated with wideband arrays is having the highest frequency of operation limited by the appearance of grating lobes, associated with the periodicity in the spacing between elements of the array. Another issue is the working frequency of the element of the array. The lowest frequency of operation is in general related to the size of the element.
In this thesis a Concentric Ring Array of Connecting Spirals has been developed. The connections between spirals of opposite polarizations reduces the reflection coefficient at lower frequencies.
The concentric rings topology had the radius and relative rotations of each ring optimized using Genetic Algorithms to minimize the RSLL at higher frequencies.
The addition of a size constraint in the optimization procedure kept the array compact. The optimized array operates from 1 to 6.9 GHz. The design was then updated using the WAVES technique to include a scaled down copy in its center, extending the bandwidth of the array up to 13 GHz.
Moreover, we proposed a new design for the array of connected spirals which consists of arranging spirals in a uniform array and connecting the arms of the neighboring spirals. Simulations indicate that the design can have an arbitrarily large bandwidth depending on the finiteness of the array. A prototype has been built and measured to validate the concept.

Université Paris-Saclay
Espace Technologique / Immeuble Discovery
Route de l'Orme aux Merisiers RD 128 / 91190 Saint-Aubin, France